

MODELLING CROSS-SHORE TRANSPORT OF GRADED SEDIMENTS UNDER WAVES

W. van de Wardt

2018



MODELLING CROSS-SHORE TRANSPORT OF GRADED SEDIMENTS UNDER WAVES

MASTER THESIS

Varsseveld, October 2018

Author

Willeke van de Wardt

Graduation committee

Dr. ir. J.S. Ribberink (University of Twente)

Dr. ir. J.J. van der Werf (University of Twente, Deltares)

Dr. ir. J. van der Zanden (University of Twente)

Cover photo: NatBG.com - © 2016

ABSTRACT

It is important that the development of the coastline is constantly monitored, and that the effects of interventions, such as nourishments, can be accurately predicted by morphological models. A widely used morphodynamic model by coastal engineers is DELFT3D (Lesser et al., 2004). Both the coastline and these nourishments contain sand with varying grain sizes (mixed sediment). Hence the model of DELFT3D needs to work with these mixed sediments to determine the evolution of the long-term morphodynamics of the beach profile. The objective of this thesis is to investigate the difference between modelled transport rates using a single-fraction approach and multi-fraction approach, and comparing these rates to wave flume data (Van der Zanden et al., 2017). This is done with DELFT3D, using formulations for bed-load transport by Van Rijn (2007c).

First, two stand-alone MATLAB models for bed-load transport were used to compare the results of a single-fraction approach and multi-fraction approach to a database containing data from graded sediment transport experiments in oscillatory flow tunnels (Van der Werf et al., 2009). The bed-load transport models that were used were the bed-load transport formulations by Van Rijn (2007c) and the SANTOSS model (Van der A et al., 2013). The Van Rijn model gave comparable results for both the single-fraction and multi-fraction approach, giving only slightly better results for the multi-fraction approach. For the SANTOSS model, the multi-fraction approach evidently gave a better approximation of the measured bed-load transport rates. Additionally, the SANTOSS model gave the best results when compared to the database

Before any analysis of the transport rates using DELFT3D took place, the hydrodynamics were recalibrated. Previously, Schnitzler (2015) already modified formulations in DELFT3D to obtain better results for regular breaking waves. Since the data were not processed till after these modifications, recalibration was required. Generally, DELFT3D replicated the wave height and undertow velocities accurately, with exception of the undertow velocities at two of the twelve locations. At these two locations the measurements were underestimated.

Subsequently, DELFT3D was used to model both bed-load and suspended-load using a single-fraction and multi-fraction approach. When modelling the current-related suspended sediment transport and bed-load transport, little difference was noticed between the two approaches. The wave-related and total transport rates did show differences between the two approaches, where the single-fraction gave wave-related suspended sediment transport rates 3 times larger than the multi-fraction approach. It has not yet been discovered whether these differences can be attributed to grading effects or an error in DELFT3D.

Based on the results of the bed-load transport rates and current-related suspended sediment transport rates, it does not really seem important whether a single-fraction or multi-fraction approach is used. The logical follow-up step would be to implement the SANTOSS bed-load transport formulations in DELFT3D, as this bed-load transport model showed larger differences between the single-fraction and multi-fraction approach.

PREFACE

This report is the result of my master thesis project which was carried out during a period of eight months at Deltares in Delft. This report is the completion of my master Water Engineering and Management at the University of Twente. The last months have given me more insight about the modelling of cross-shore transport of graded sediments under waves, and the opportunity was given to apply the theoretical knowledge that was obtained during the courses followed during my bachelor and master track.

I would like to thank my graduation committee, starting with Joep van der Zanden. During the preparation process of this thesis project, the path towards his office was regularly walked. Even after he left the university he provided me with many ideas on the subject and was always available for questions, which have helped me to complete this thesis project. When working at Deltares, Jebbe van der Werf was the man to go to when things would not go as planned, or when there were new results to be discussed. These discussions provided new insights and were used as input for this research. Last but not least, I would like to thank Jan Ribberink for his input and broad knowledge on the subject. Due to his many years of experience, he was a very useful source of information.

I have had a splendid time at Deltares, for which I am very grateful. I would like to thank my fellow students at Deltares for showing me around in Delft and their distraction from the work when things got tough. We have had inspirational discussions and much fun over coffee, and struggled with graduation problems together. Finally, I would like to thank my friends, family, and saxophone colleagues from SHOT for their support and very welcome distractions during this graduation process.

I hope you enjoy reading this report as much as I enjoyed working on it.

Willeke van de Wardt

Varsseveld, October 2018

CONTENTS

Abstract	ii
Preface	iii
1 Introduction	1
1.1 Research motivation	1
1.2 Objective and research questions	1
1.3 Methodology	2
1.4 Outline report	3
2 Graded sediment transport processes and modelling	4
2.1 Field study: Sand Motor	4
2.2 General sand transport processes	5
2.2.1 Sheet-flow	5
2.2.2 Bed-load transport	5
2.2.3 Suspended-load transport	5
2.2.4 Sediment transport under waves	6
2.2.5 Sediment transport by currents	6
2.3 Graded sediment effects	6
2.3.1 Sheet-flow layer thickness	7
2.3.2 Hiding and exposure	7
2.3.3 Vertical sorting	8
2.3.4 Cross-shore sorting	8
2.4 Previous graded sediment transport modelling	9
2.4.1 Van Rijn formulations for bed-load transport	9
2.4.2 SANTOSS model	12
2.4.3 DELFT3D	14
2.5 Data and previous experiments	16
2.5.1 The SANTOSS database	16
2.5.2 SINBAD experiments	19
3 Validation of the bed-load transport models	23
3.1 Van Rijn model	23
3.1.1 Graded versus uniform sand approach	24
3.1.2 Graded approach using a representative grain diameter of d_{50} or d_{mean}	25
3.1.3 Effect of roughness settings	27
3.1.4 Effect of selective transport	28
3.1.5 Comparison of the different model settings	33

3.2	SANTOSS model	34
3.2.1	Graded versus uniform sand approach	35
3.2.2	Graded approach using a representative grain diameter of d_{50} or d_{mean}	36
3.2.3	Effect of roughness settings	37
3.2.4	Effect of selective transport	39
3.2.5	Comparison of the different model settings	40
3.3	Comparison Van Rijn and SANTOSS	41
3.3.1	Conclusion	43
4	Set-up and calibration of the hydrodynamics of the DELFT3D model	44
4.1	Model set-up	44
4.1.1	Grid set-up	44
4.1.2	Initial and boundary conditions	45
4.1.3	Roughness settings	45
4.2	Results of the calibration of the hydrodynamics	46
4.2.1	Wave height	47
4.2.2	Undertow	48
4.2.3	Turbulent kinetic energy	51
4.2.4	Conclusion	53
5	Assessment of modelled transport rates in DELFT3D	54
5.1	Fraction configurations	55
5.2	Suspended sediment transport	56
5.2.1	Suspended sediment concentrations	56
5.2.2	Grain size distribution in the water column	60
5.2.3	Cross-shore sediment transport	62
5.3	Bed-load transport	64
5.4	Total net transport rates	65
5.5	Conclusion	66
6	Discussion	68
6.1	Modelling bed-load transport rates	68
6.2	Measuring instruments wave flume experiments	69
6.3	Modelling hydrodynamics wave flume experiments	69
6.4	Modelled suspended sediment transport due to waves	70
7	Conclusions and recommendations	71
7.1	Conclusions	71
7.2	Recommendations	73
	References	75
	References	75
	Appendices	
A	Van Rijn equations	77
A.1	Sediment bed classification	77
A.2	Current related bed roughness	77
A.2.1	Ripples	77

A.2.2	Mega-ripples	77
A.3	Bed-shear stress	78
B	SANTOSS equations	79
B.1	Bed-shear stress	79
C	DELFT3D	80
C.1	Grids	80
C.2	System of equations	81
C.2.1	Hydrostatic pressure assumption	81
C.2.2	Continuity equation	81
C.2.3	Horizontal momentum equation	81
C.2.4	Turbulence closure models	81
C.2.5	Concentration profile (Rouse profile)	82
D	SINBAD experiments	83
E	Performance criteria	84
F	Validation Van Rijn model for bed-load transport	85
F.1	Fortran code	85
F.2	Comparison Fortran and MATLAB	86
F.2.1	Streaming	86
F.2.2	Comparison	86
F.3	MATLAB results	88
F.4	Results fractions	88
F.5	Effect of roughness settings using $d_{rep} = d_{50}$	90
F.6	Selective transport using $d_{rep} = d_{50}$	91
G	Validation SANTOSS model for bed-load transport	95
G.1	Results fractions	95
G.2	Wave-related roughness	97
G.3	Effect of selective transport for $d_{rep} = d_{50}$	99
H	Sensitivity analysis DELFT3D	101

INTRODUCTION

As climate induced effects may result in a sea level rise and more extreme weather events, it is essential that the morphological effects of mitigating measures, for example nourishments, can be predicted accurately to guarantee the safety of the human population living near the coast. Profound understanding of mixed sediment transport behaviour is especially relevant in the view of nourishments, because the coastal regions consists of a vast variety of grain sizes, where the grain size of sand nourishments may also differ from the grain size at the pre-nourished beach (Huisman et al., 2016). Additionally, the differences in bed compositions and the rate at which sediment transport takes place along the coast affect the ecology within that region and the habitat of fish and benthic species (Knaapen et al., 2003).

1.1 RESEARCH MOTIVATION

Up till today, numerical models aiming to determine the morphological evolution of coastlines usually assume that the bed consists of a single grain size. However, this is not true as the coastal region consists of sand with different grain sizes and thus mixed (or graded) sediment is present. As the transport processes for graded sediment differ substantially from uniform sediment, it is of the essence that morphodynamic models are able to predict these transport processes for graded sediment accurately. An example of such a morphodynamic model which can simulate hydrodynamic flows, sediment transport, and morphological changes, is DELFT3D (Lesser et al., 2004). Currently, this model has been parametrised on the basis of experimental data that was primarily obtained under steady flow conditions or in oscillatory flow tunnels. With newly obtained wave flume data, this model can now be validated for graded sediment transport processes by waves, to investigate the effect on the model results when using a graded sediment approach instead of a uniform sediment approach. Chapter 2 further elaborates on graded sediment transport processes, available models and data.

1.2 OBJECTIVE AND RESEARCH QUESTIONS

The objective of this thesis is stated as follows:

Assessment of DELFT3D for cross-shore graded sediment transport under waves.

To achieve the research objective, two research questions are formulated:

1. How well do practical models for bed-load transport predict oscillatory sheet-flow transport of mixed sediments and how can these models be improved?
2. What are the effects of using a graded sediment approach instead of a uniform approach in DELFT3D regarding the (a) suspended sediment concentrations, (b) suspended sediment grain sizes, and (c) cross-shore net total sediment transport?

1.3 METHODOLOGY

In this section, a methodology per research question is provided.

RESEARCH QUESTION 1

How well do practical models for bed-load transport predict oscillatory sheet-flow transport of mixed sediments and how can these models be improved?

Two models were used to model bed-load transport, namely the model by Van Rijn (2007c) and the SANTOSS model by Van der A et al. (2013). Both models have already been used to compute graded sediment transport rates in the past. The SANTOSS database (Van der Werf et al., 2009) was used to validate the practical models. The experiments included in this database were carried out in oscillatory flow tunnels where predominantly bed-load takes place. Both models were validated using the same approach:

1. First, the graded sediment was treated as uniform, which means that no distinction was made between the different grain sizes per fraction, and only one representative grain diameter was used for the entire mixture,
2. Subsequently, the bed-load transport rates were validated with a graded sediment approach, where a distinction was made between the grain size per fraction.
3. Next, different approaches for the grain roughness were used.
4. Finally, the effects of the correction factors for selective transport were investigated.

RESEARCH QUESTION 2

After computing the bed-load transport rates in stand-alone MATLAB models using either SANTOSS or Van Rijn, both the bed-load and suspended sediment transport were computed using DELFT3D. DELFT3D is a suitable model to model the transport rates, as it is able to calculate flows, waves, sediment transport rates and morphological changes (Lesser et al., 2004). During a large scale wave flume experiment, data were obtained regarding the transport rates of graded sediment under waves around a breaker bar. Research question 2 is stated as follows:

What are the effects of using a graded sediment approach instead of a uniform approach in DELFT3D regarding the (a) suspended sediment concentrations, (b) suspended sediment grain sizes, and (c) cross-shore net total sediment transport?

Without allowing any morphological changes in DELFT3D, first the suspended sediment concentrations in the water column were investigated. This was done by comparing the modelled concentrations using a graded approach to the measured concentrations. Additionally, the behaviour and contribution of the different fractions was analysed to obtain a better comprehension of graded sediment transport processes. Next, the modelled d_m in the water column using a graded approach was compared to the data and its behaviour was analysed.

Finally, the cross-shore graded sediment transport was analysed in terms of (1) the suspended sediment transport due to currents, (2) the suspended sediment transport due to waves, (3) the bed-load transport due to currents and waves, and (4) the net total sediment transport. This was done for both the transport per fraction and total transport of all fractions, where the results of the graded approach were compared to those of the uniform approach.

1.4 OUTLINE REPORT

In Chapter 2 a literature review is provided on graded sediment transport processes and graded sediment modelling. In Chapter 3 the bed-load transport models of Van Rijn and SANTOSS are validated using data obtained in oscillatory flow tunnel experiments. In Chapter 4 the hydrodynamics within DELFT3D are calibrated, where after in Chapter 5 the computed sediment transport rates using a graded and uniform sand approach are compared to each other and to the data which were obtained during wave flume experiments. In Chapter 6 the results, performance of the models, and any uncertainties are discussed, followed by the conclusions and recommendations in Chapter 7.

2

GRADED SEDIMENT TRANSPORT PROCESSES AND MODELLING

In this chapter, first an example of a field study is presented where both cross-shore and long-shore sediment sorting has taken place. Hereafter, the processes regarding sediment transport are explained, starting with the general sand transport processes and followed by graded sediment effects. Subsequently, Section 2.4 provides information about previous graded sediment transport modelling and the models used within this thesis project. Finally, the datasets which are used to validate the sediment transport rates are presented.

2.1 FIELD STUDY: SAND MOTOR

An example of a large-scale nourishment is the Sand Motor (The Netherlands), which was applied between April and August 2011. Here the beach and dune region consisted of fine sand ($100\text{-}200\mu\text{m}$), the swash and surf zone of fine to medium sand ($200\text{-}400\mu\text{m}$) and the region offshore till a depth of 10m of finer sand again ($100\text{-}300\mu\text{m}$). The nourishment had an average median grain size d_{50} of about $278\mu\text{m}$. The differences in grain sizes and the development of the nourishment were monitored a while after the intervention to observe the influence of graded sediment effects (Fig. 2.1). It was found that selective transport of the finer sediment and the bed-shear stresses caused by the hydrodynamic forcing were the drivers of spatial heterogeneity regarding grain sizes. Figure 2.1 shows the spatial distribution of the grain sizes at the site of the Sand Motor right before (left) and three years after (right) the application of the nourishment, with the dominant wave direction towards the North-East. Despite the well mixed sediment that was used for the Sand Motor, the longshore profile clearly shows sorting, with coarsening at the bulge and finer sand further North.

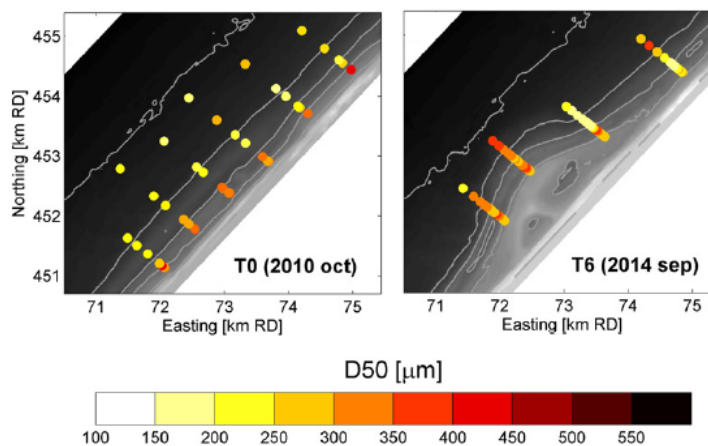


Figure 2.1: D_{50} along the site of the Sand Motor before and after its application (Huisman et al., 2016)

2.2 GENERAL SAND TRANSPORT PROCESSES

Sediment can be transported by currents and waves. For grains to be set into motion, enough force must be exerted on the bed, causing the lift and drag forces on a grain to be larger than the gravitational and frictional forces, causing the moment of incipient motion. When high flow velocities are present, sheet-flow may occur (Section 2.2.1). Sediment can be transported as bed-load or suspended-load, which is shown in Figure 2.2.

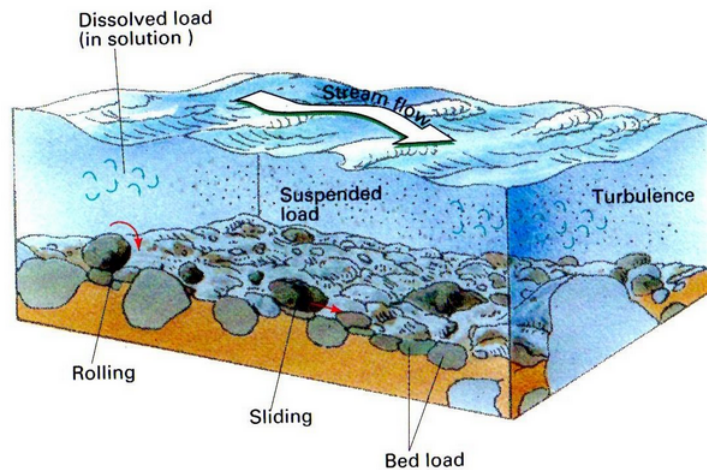


Figure 2.2: Modes of sediment transport (Indiawrm, 2015)

2.2.1 SHEET-FLOW

Sheet-flow occurs when the flow is very strong and bed-forms such as ripples are washed out. When this occurs, a plain bed remains and the sand is transported in a sediment-water mixture, which is up to a few centimetres thick. Sheet-flow transport is characterized by very high sediment transport rates. Hence it is of importance that the sediment transport in these regimes can be predicted and modelled accurately (Wright, 2002). When the flow velocity increases, sediment is entrained and the concentration decreases in the lower part of the sheet flow layer, which is called the pick-up layer. Once the flow velocity decreases again, the sediment settles and the concentration increases once again in this pick-up layer. The concentration in the top layer is in phase with the flow velocity, whereas the concentration in the pick-up layer is in anti-phase.

2.2.2 BED-LOAD TRANSPORT

Bed-load is the fraction of transported grains that are still in contact in the bed and move by rolling, sliding and jumping (saltation) over each other (The Open University, 1999) (Fig. 2.2). Rolling and sliding occurs when there are low flow velocities, whereas saltation takes place with higher flow velocities.

2.2.3 SUSPENDED-LOAD TRANSPORT

A different mode of transport besides bed-load is suspended-load. Large orbital velocities and high levels of turbulence create higher bed-shear stresses, creating the potential for the sediment to be picked up by the flow. After the grain has been picked up, it will be entrained higher into the water column due to turbulent mixing, where the upward force exceeds the gravitational force (Ribberink,

2011). Grains that are in suspension have been separated from the bed and are transported higher up in the water column, and only when the flow slackens, these grains regain contact with the bed (The Open University, 1999).

2.2.4 SEDIMENT TRANSPORT UNDER WAVES

Waves approaching the shoreline increase in height and steepness before they break and their energy is dissipated. Due to the wave skewness which increases with an increasing relative wave height, net onshore transport is caused by the increasing difference in flow velocities under the crest and trough (Hassan, 2003). Besides, due to the non-linear relation between the magnitude of the flow velocity and sediment transport rate, where higher flow velocities transport relatively more sediment, these large onshore velocities carry more sediment than the smaller offshore velocities (Fig.2.3), resulting in an accumulation of sediment towards the shoreline.

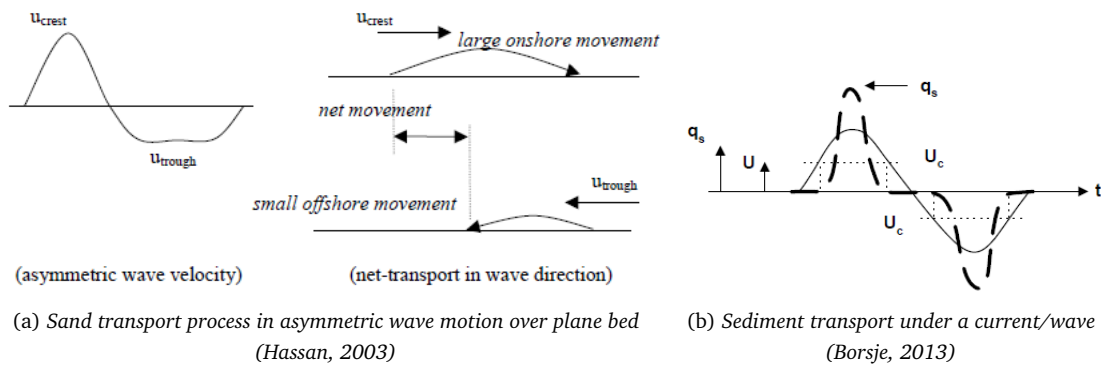


Figure 2.3: Sediment transport under an asymmetric wave

2.2.5 SEDIMENT TRANSPORT BY CURRENTS

As elaborated on earlier, longshore currents also play a role regarding sediment transport, as shown by Figure 2.1. When waves approach the beach at an oblique angle, a longshore current will be created as the waves break and their energy is dissipated. With the presence of (tidal) currents and the stirring up of sediment by waves, an advantageous environment is created for sediment transport.

2.3 GRADED SEDIMENT EFFECTS

The mobility of sediment changes when present in a mixture. The mobility of fine and coarse sediment are respectively lower and higher when present in a mixture instead of a homogeneous environment (Fig. 2.4). Figure 2.4 shows that when fine sand (0.13mm) is present within a mixture, its mobility decreases significantly in comparison with uniform sand. Additionally, the relation between the grain size and suspended sediment transport rate is non-linear, as explained by Van Rijn (2007c) as follows: Using the transport formula $q_s \approx \sum p_i d_i^\alpha u^3$, with p_i and d_i the percentage and diameter of fraction i , and u the velocity. α varies between 2 and -2 , and is now chosen to be -2 , and the symmetric size distribution ($N = 7$) is given by: $p_1 = 0.05$, $p_2 = 0.15$, $p_3 = 0.2$, $p_4 = 0.2$, $p_5 = 0.2$, $p_6 = 0.15$, $p_7 = 0.05$ and $d_1 = 0.5d$, $d_2 = 0.666d$, $d_3 = 0.8d$, $d_4 = 1d$, $d_5 = 1.25d$, $d_6 = 1.5d$, $d_7 = 2d$. The multi-fraction approach can then be expressed in terms of the single-fraction approach by: $q_{s,N=7} = 1.26q_{s,N=1}$ for all current velocities. Choosing either $\alpha = 2$ or -2 , both show higher transport rates using a multi-fraction

approach, where the transport of coarser sediment is dominant when α is positive, and transport of fine sediment is dominant when α is negative.

The processes for graded sediment transport are elaborated on in this section. These processes regard the thickness of the sheet flow layer, hiding and exposure, vertical sorting and cross-shore sorting.

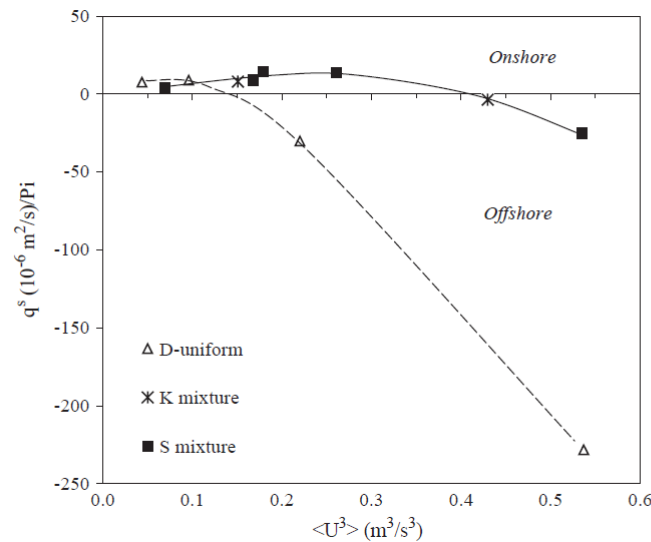


Figure 2.4: Comparison of the transport rates of fine sand (0.13mm) when being present in uniform sand (triangles), and a mixture with coarser grains (stars and solid squares) (Hassan & Ribberink, 2005).

2.3.1 SHEET-FLOW LAYER THICKNESS

The thickness of the sheet flow layer is larger for fine sediment due to unsteady effects (O'Donoghue & Wright, 2004). Furthermore, grading has a significant effect on the sheet flow layer thickness. For experiments with uniform and graded sediment with both a d_{50} of 0.28mm, the sheet flow layer thickness of the mixture was much greater, as both coarse and fine sediment are present.

2.3.2 HIDING AND EXPOSURE

In environments with graded sediment, smaller grains tend to hide behind and between the coarser grains, where consequently the coarser grains are exposed to the flow. The degree of exposure is defined by the degree that a certain particle is exposed to the flow when regarding unequal grain sizes. Smaller particles hide behind the larger particles, which have a relatively larger exposure to the flow, such that the larger grain sizes are picked up more easily. This phenomenon is called "hiding and exposure" and is demonstrated in Figure 2.5. The degree of exposure determines the critical bed-shear stress required for initiation of motion, which again influences the transport rates of the different grain sizes. Due to these hiding and exposure processes, the mobility of sediment is different for a graded bed than for a uniform bed (Fig. 2.4). Additionally, the variety of grain sizes in the bed has a negative effect on the smoothness of the bed, as there are more protrusions. These irregularities result in a thicker sheet-flow layer.

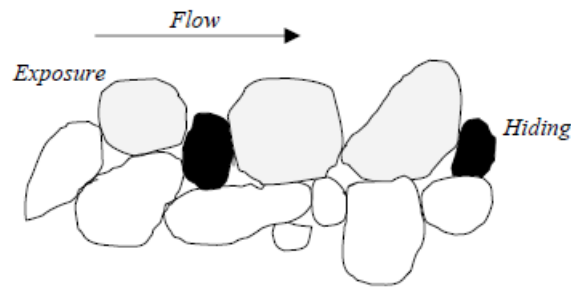


Figure 2.5: Hiding and exposure of sediment particles in a mixture (Hassan, 2003).

2.3.3 VERTICAL SORTING

Vertical sorting may take place in environments where different grain sizes are present, and bed forms (ripples) may be formed. An armouring layer of immobile large grains can be formed on top of the smaller grains, preventing them from being transported by the flow, even though their threshold for initiation of motion has been exceeded. Furthermore, sorting processes take place around ripples, where for river dunes coarsening takes place at the bottom. However, lab experiments have provided results where coarsening actually takes place on top of ripples (Cáceres et al., 2018). It is still unclear how such processes affect the net transport rates of graded sand in a sand ripple regime and how these sorting processes take place in coastal environments.

2.3.4 CROSS-SHORE SORTING

Besides vertical sorting, also cross-shore sorting takes place as an effect of graded sand transport. This is illustrated by Figure 2.6, with larger grain sizes landwards and finer sand further seawards. This is caused by the currents approaching the shoreline, which have the capacity to transport coarse sand. The offshore directed bottom current however, is weaker and only able to transport the finer grains. Fine grains are more easily eroded, resulting in coarsening of the shoreline (Hassan, 2003).

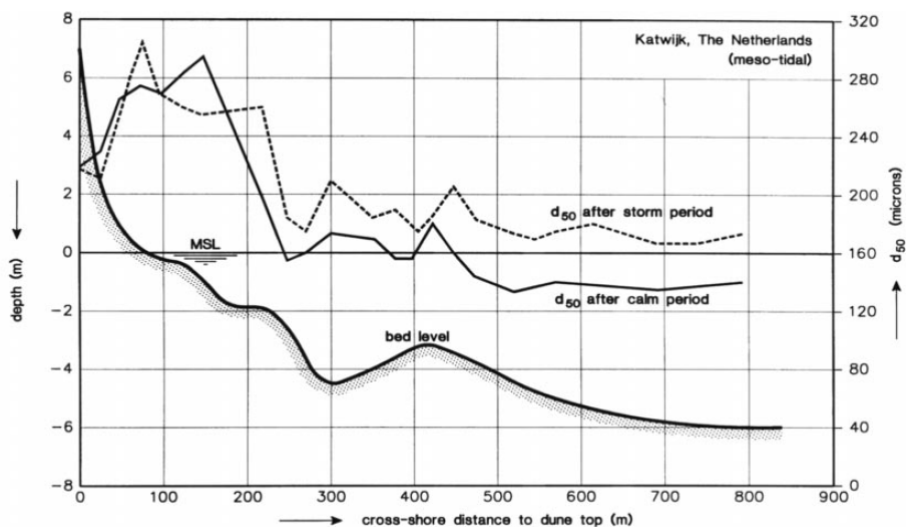


Figure 2.6: Cross-shore sorting as an effect of graded sand transport (Hassan, 2003).

2.4 PREVIOUS GRADED SEDIMENT TRANSPORT MODELLING

Two models that can be used to model bed-load transport for graded sediment are the formulations by Van Rijn (2007c) and the SANTOSS model by Van der A et al. (2013). The main difference between these two bed-load transport models, is the incorporation of formulations for phase lag effects in the SANTOSS model, which are not included in the bed-load transport formulations by (Van Rijn, 2007c). These phase lag effects are covered in Section 2.4.2. Furthermore, DELFT3D is an often used model when modelling both the bed-load and suspended transport. In this section information is provided about these three different models.

2.4.1 VAN RIJN FORMULATIONS FOR BED-LOAD TRANSPORT

Van Rijn (2007c) has incorporated graded sediment effects within his formulations for bed-load transport. This model originates from experiments carried out in a flume and existing transport formulae for rivers in particular. However, in his paper (2007c) he validates the model with data retrieved from experiments carried out in a wave tunnel under sheet-flow conditions. In the bed-load formula by Van Rijn (2007a) the transport rate is assumed to scale quasi-instantaneously to the velocity forcing. The multifraction approach of Van Rijn divides the bed into different fractions and computes the sand transport rate of each size fraction. The net bedload transport is determined by the summation of the transport rates per size fraction times the probability of occurrence of each size fraction. The formulae for sand transport and especially bed-load transport as defined by Van Rijn (2007c) originates from experiments carried out in flumes and existing transport formulae for particularly rivers. However, this formulation has been validated with oscillatory flow in a wave tunnel using the dataset of (Hassan, 2003) (Table 2.1, Code P9F). Validation then showed that the modelled total transport rates were overestimated, where the transport of the fine fraction was systematically overestimated by the model, and the transport of the coarse fraction was most of the time underestimated.

NET BED-LOAD TRANSPORT

The formula for the total sand transport rate is given by:

$$q_{b,tot} = \sum p_j q_{b,j} \quad (2.1)$$

where p_j is the percentage of a certain fraction in a mixture, where subscript j denotes the fraction, and $q_{b,j}$ the transport rate of this fraction. The transport rate per fraction in $m^2 s^{-1}$ is calculated by:

$$q_{b,j} = 0.5 f_{silt,j} d_j [D_{*,j}]^{-0.3} \left[\frac{\tau'_{b,cw}}{\rho_w} \right]^{0.5} [T_j], \quad (2.2)$$

where $f_{silt,j}$ ($= \frac{d_{sand}}{d_j}$) is the silt factor, d_j the grain size of the fraction, $D_{*,j}$ the dimensionless particle size of fraction j , $\tau'_{b,cw}$ the instantaneous grain-related bed-shear stress due to both currents and waves, ρ_w the density of water, and T_j the dimensionless bed-shear stress parameter.

BED-SHEAR STRESS

The dimensionless particle size $D_{*,j/rep}$ per fraction or for the entire mixture is given by:

$$D_{*,j} = d_j [(s-1)g/v^2]^{1/3} \quad (2.3)$$

$$D_{*,rep} = d_{rep} [(s-1)g/v^2]^{1/3}, \quad (2.4)$$

with d_j the grain size of fraction j and d_{rep} the representative diameter of the entire mixture, which is either d_{50} or d_m (section 2.5), where Van Rijn (2007c) assumes that $d_{rep} = d_{50}$. g is the gravitational acceleration, ν the kinematic viscosity and $s = \frac{\rho_s - \rho_w}{\rho_w}$ with ρ_w the density of water and ρ_s the density of sediment. The dimensionless critical Shields parameter ($\theta_{cr,j}$) is calculated using the formulae of Miller et al. (1977):

$$\begin{aligned}\theta_{cr,j/rep} &= 0.115D_{*,j/rep}^{-0.5} & 1 < D_{*,j} \leq 4 \\ \theta_{cr,j/rep} &= 0.14D_{*,j/rep}^{-0.64} & 4 < D_{*,j} \leq 10 \\ \theta_{cr,j/rep} &= 0.04D_{*,j/rep}^{-0.1} & 10 < D_{*,j} \leq 20 \\ \theta_{cr,j/rep} &= 0.013D_{*,j/rep}^{0.29} & 20 < D_{*,j} \leq 150 \\ \theta_{cr,j/rep} &= 0.055 & 150 < D_{*,j/rep}\end{aligned}\quad (2.5)$$

where subscript j and rep either denote the fraction or the representative diameter of the entire mixture. The critical bed-shear stress is then determined by:

$$\tau_{b,cr,d_j} = \theta_{cr,d_j} [(\rho_s - \rho_w)gd_j] \quad (2.6)$$

$$\tau_{b,cr,d_{rep}} = \theta_{cr,d_{rep}} [(\rho_s - \rho_w)gd_{rep}]. \quad (2.7)$$

The instantaneous bed-shear stress for currents and waves is finally given by:

$$\tau'_{b,cw} = 0.5\rho_w f'_{cw} (U_{\delta,cw})^2, \quad (2.8)$$

with f'_{cw} and $U_{\delta,cw}$ respectively being the friction coefficient and instantaneous velocity due to currents and waves at the edge of the wave boundary layer.

BED ROUGHNESS DUE TO BEDFORMS

The dimensions of the bedforms are calculated using the representative grain size of the entire mixture. The formulae to calculate the current related roughness due to the dimensions of ripples and mega-ripples are found in Appendix A.2. The total physical current related roughness $k_{s,c}$ is then calculated by:

$$k_{s,c} = [k_{s,c,r}^2 + k_{s,c,mr}^2]^{0.5}. \quad (2.9)$$

Van Rijn (2007c) assumes that dunes are not present. Additionally, the current-related roughness only depends on the representative grain diameter of the entire mixture and not the grain size per fraction. The current-related friction factor and current-related grain friction coefficient are then given by:

$$f_{c,j} = 0.24[\log(12h/k_{s,c})]^{-2} \quad (2.10)$$

$$f'_{c,j} = 0.24[\log(12h/k_{s,grain})]^{-2}, \quad (2.11)$$

with $k_{s,grain}$ the grain roughness, either based on d_{g0} or d_j . Additionally, the wave-related roughness due to ripples is equal to the current related roughness due to ripples: $k_{s,w,r} = k_{s,c,r}$. The wave-related friction factor and wave-related grain friction coefficient are then given by:

$$f_{w,j} = \exp \left[-6 + 5.2 \left(\frac{A_w}{k_{s,w,r}} \right)^{-0.19} \right] \quad \text{with } f_{w,j,max} = 0.3 \quad (2.12)$$

$$f'_{w,j} = \exp \left[-6 + 5.2 \left(\frac{A_w}{k_{s,grain}} \right)^{-0.19} \right] \quad \text{with } f'_{w,j,max} = 0.05 \quad (2.13)$$

with A_w the representative orbital excursion amplitude. Finally the friction coefficient due to currents and waves is given by:

$$f'_{c,w,j} = \alpha\beta f'_c + (1 - \alpha)f'_w, \quad (2.14)$$

with β a coefficient related to the vertical structure of the velocity profile (Appendix A.2), and α :

$$\alpha = \frac{|U_{net}|}{|U_{net}| + U_w}, \quad (2.15)$$

with U_w is the representative orbital velocity amplitude and $|U_{net}|$ the net current velocity.

SELECTIVE TRANSPORT

In sediment mixtures, selective transport takes place due to grading effects. This involves hiding and exposure, where smaller grains are hidden behind coarser grains and are thus less exposed to the flow. Additionally, coarser grains endure a larger amount of fluid drag. Van Rijn (2007c) corrects for these two effect of selective transport due to grading effects using two correction factors:

1. The hiding and exposure factor by Egiazaroff (1965):

$$\xi_j = \left[\frac{\log(19)}{\log(19d_j/d_{rep})} \right]^2, \quad (2.16)$$

which expresses to what extent the particles are exposed to the flow, as the smaller grains may be hidden behind the larger grains.

2. The correction factor for the effective grain-shear stress by Day (1980):

$$\lambda_j = \left(\frac{d_j}{d_{rep}} \right)^{0.25}, \quad (2.17)$$

which represents the amount of fluid drag to which a particle is exposed.

DIMENSIONLESS BED-SHEAR STRESS PARAMETER

Van Rijn introduces four methods to determine the dimensionless bed-shear stress parameter T_j . Methods A and B both use the d_{rep} approach for the critical bed-shear stress, whereas methods C and D use the d_j approach. The difference between method A and B lies within the correction factor for the effective grain-shear stress which is present in the former and absent in the latter. Method A and B are respectively given by the following formulae:

$$\text{Method A: } T_j = \lambda_j \left[\frac{\tau'_{b,cw} - \xi_j \left(\frac{d_j}{d_{rep}} \right) \tau_{b,cr,d_{rep}}}{\left(\frac{d_j}{d_{rep}} \right) \tau_{b,cr,d_{rep}}} \right] \quad (2.18)$$

$$\text{Method B: } T_j = \left[\frac{\tau'_{b,cw} - \xi_j \left(\frac{d_j}{d_{rep}} \right) \tau_{b,cr,d_{rep}}}{\left(\frac{d_j}{d_{rep}} \right) \tau_{b,cr,d_{rep}}} \right]. \quad (2.19)$$

Methods C and D differ as method C uses the correction factor for hiding and exposure by (Egiazaroff, 1965) which is absent in method D. Method C and D are respectively given by the following formulae:

$$\text{Method C: } T_j = \left[\frac{\tau'_{b,cw} - \xi_j \tau_{b,cr,d_j}}{\tau_{b,cr,d_j}} \right] \quad (2.20)$$

$$\text{Method D: } T_j = \left[\frac{\tau'_{b,cw} - \tau_{b,cr,d_j}}{\tau_{b,cr,d_j}} \right] \quad (2.21)$$

In his paper, Van Rijn (2007c) recommends to use method A.

2.4.2 SANTOSS MODEL

The SANTOSS model incorporates graded sediment effects by first calculating the net transport rates per fraction, and then determining the total net transport rate by summing these rates per fraction (Van der A et al., 2013). Additionally graded sediment effects are incorporated, such as a correction factor for hiding and exposure. The model calculates the near-bed transport under waves and currents and determines the total net sand transport rate by calculating the difference between the sand transport during the positive crest half-cycle and negative trough half-cycle. The formula takes hiding and exposure, and phase lag effects into account, as the sand transport during each half-cycle consists of sediment which is transported during the present cycle and sand that has not yet settled down in the previous half-cycle. Previously this model was already used for graded sediment conditions by Van der A et al. (2013) and gave fairly good results for the net total transport (89% in a factor 2 interval from the data). However, the transport rates per fraction are still unknown and graded sediment effects need to be examined more thoroughly.

NET BED-LOAD TRANSPORT

The formula for the net transport rate as used in the SANTOSS model is given by:

$$\vec{\Phi} = \sum_{j=1}^M p_j \frac{\vec{q}_{s,j}}{\sqrt{(s-1)gd_j^3}} \quad (2.22)$$

where p_j is the percentage of a fraction in the mixture, $\vec{q}_{s,j}$ the transport of this fraction, d_j the grain size of the fraction, s the ratio between the densities of water and sediment, and M the total number of fractions. This equation is then rewritten for the non-dimensional net transport rates, such that:

$$\vec{\Phi} = \sum_{j=1}^M p_j \frac{\sqrt{|\theta_{c,j}|} T_c (\Omega_{cc,j} + \frac{T_c}{2T_{cu}} \Omega_{tc,j}) \frac{\vec{\theta}_{c,j}}{|\theta_{c,j}|} + \sqrt{|\theta_{t,j}|} T_t (\Omega_{tt,j} + \frac{T_t}{2T_{tu}} \Omega_{ct,j}) \frac{\vec{\theta}_{t,j}}{|\theta_{t,j}|}}{T} \quad (2.23)$$

where T denotes the total wave period and T_j a part of this total wave period as explained in Figure 2.7. $\Omega_{12,j}$ denotes during which period the sediment is (1) entrained and (2) transported, which is respectively c for crest and t for trough.

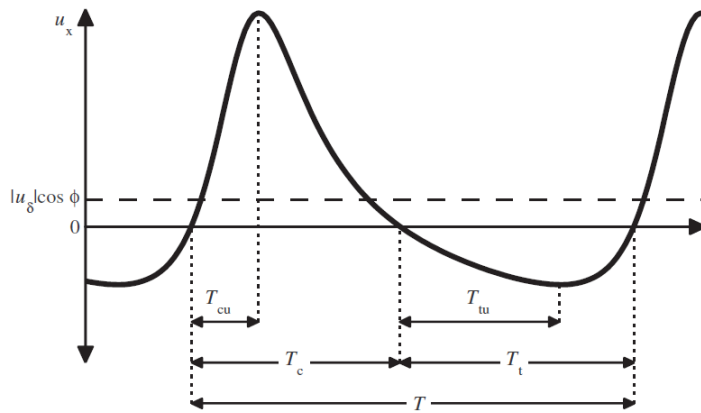


Figure 2.7: Sketch of the different wave periods with their corresponding near-bed velocities. T_c and T_{cu} are the positive (crest) flow duration and flow acceleration. T_t and T_{tu} are the negative (trough) flow duration and flow acceleration (Van der A et al., 2013)

BED-SHEAR STRESS

The vector for the dimensionless bed-shear stress is given by:

$$\vec{\theta}_{i,j} = \left\{ \frac{\frac{1}{2}f_w\delta_{i,j}|u_{i,r}|u_{i,rx} + \tau_w Re}{(s-1)gd_j}, \frac{\frac{1}{2}f_w\delta_{i,j}|u_{i,r}|u_{i,ry}}{(s-1)gd_j} \right\}, \quad (2.24)$$

where i denotes the wave crest or trough, $|u_{i,r}|$ is the representative half-cycle orbital velocity, and $u_{i,rx}$ and $u_{i,ry}$ the representative combined wave-current velocity in the x and y direction. $\tau_w Re$ is a contribution related to progressive surface waves and is absent in the case of oscillatory flow tunnel experiments and f_{cwi} is the friction factor due to currents and waves.

BED ROUGHNESS

The bed roughness consists of the current-related roughness and the wave-related roughness. The friction factor due to currents and waves $f_{\delta wi}$ is given by:

$$f_{cwi} = \alpha f_{ci} + (1 - \alpha)f_{wi} \quad (2.25)$$

where subscript i denotes the crest (c) or trough (t) period, and α is given by Equation 2.15. Furthermore the current-related friction factor is calculated assuming a logarithmic profile:

$$f_{ci} = 2 \left[\frac{0.4}{\ln(30\delta/k_{s,\delta})} \right]^2 \quad (2.26)$$

where δ is the distance between the bed and the top of the wave boundary layer, and $k_{s,\delta}$ is the current related roughness (Appendix B.1). Finally the wave friction factor is given by:

$$\begin{cases} f_{wi} = \exp \left[-6 + 5.2 \left(\frac{A_w}{k_{s,w}} \right)^{-0.19} \right] \\ f_{wi,max} = 0.3 \end{cases}$$

where A_w is the peak orbital diameter, and $k_{s,w}$ the wave related roughness (Appendix B.1).

HIDING AND EXPOSURE

Hiding and exposure is incorporated in the SANTOSS model by correction factor λ for the effective Shields parameter by Day (1980) (Eq. 2.17), where Van der A et al. (2013) suggests that $d_{rep} = d_{mean}$. The effective Shields parameter is then determined by:

$$|\theta_{i,j,eff}| = \lambda_j |\theta_{i,j}| \quad (2.27)$$

The effective Shields parameter is embedded in the formula determining the sand load entrained in a flow during each half-cycle:

$$\Omega_{i,j} = \begin{cases} 0 & \text{if } |\theta_{i,j,eff}| \leq \theta_{cr,j} \\ m(|\theta_{i,j,eff}| - \theta_{cr,j})^n & \text{if } |\theta_{i,j,eff}| > \theta_{cr,j} \end{cases} \quad (2.28)$$

PHASE LAG

Whether sediment is transported during the current or successive crest or trough cycle depends on the phase lag parameter. This parameter is calculated per sediment fraction and are given by the following formulae:

$$P_{c,j} = \begin{cases} \alpha \left(\frac{1-\xi\hat{u}_c}{c_w} \right) \left(\frac{\eta}{2(T_c - T_{cu})w_{sc,j}} \right) & \text{if } \eta > 0 \text{ (ripple regime)} \\ \alpha \left(\frac{1-\xi\hat{u}_c}{c_w} \right) \left(\frac{\delta_s c}{2(T_c - T_{cu})w_{sc,j}} \right) & \text{if } \eta = 0 \text{ (sheet flow regime)} \end{cases} \quad (2.29)$$

$$P_{t,j} = \begin{cases} \alpha \left(\frac{1+\xi \hat{u}_c}{c_w} \right) \left(\frac{\eta}{2(T_t - T_{tu})} w_{st,j} \right) & \text{if } \eta > 0 \text{ (ripple regime)} \\ \alpha \left(\frac{1+\xi \hat{u}_c}{c_w} \right) \left(\frac{\delta_{si} t}{2(T_t - T_{tu})} w_{st,j} \right) & \text{if } \eta = 0 \text{ (sheet flow regime)} \end{cases} \quad (2.30)$$

where α is the calibration coefficient, η the ripple height, ξ accounts for the shape of the velocity and the concentration profile, δ_{si} the sheet flow layer thickness for the half cycle, and w_{si} the sediment settling velocity within the half cycle. When $P_i > 1$ there is an exchange of sand between cycles. How much sand is transported within a cycle is determined by $\frac{1}{P_i}$. The amount of sand that stays in suspension until the next cycle is given by $1 - \frac{1}{P_i}$. The different wave periods with their corresponding near-bed velocities are schematised in Figure 2.7.

2.4.3 DELFT3D

In this section general information about equations solved by the model are explained, followed by specific formulae used for modelling of the hydrodynamics, and finally concluding with equations for the suspended sediment transport. DELFT3D uses the formulations by Van Rijn (1993) to compute the bed-load transport.

COORDINATE SYSTEM

DELFT3D uses a grid to solve the equations per grid cell (Fig. C.1). The equations can be solved on a number of grids, namely Cartesian rectangular, orthogonal curvilinear (boundary fitted), or spherical grid (Lesser et al., 2004). The hereafter stated equations are applicable for a Cartesian rectangular grid. For the vertical grid direction a boundary fitted (σ -coordinate) approach is used (Fig. C.2).

2.4.3.1 HYDRODYNAMICS

The DELFT3D-FLOW module is used to solve the unsteady shallow-water equations and compute the sediment transport rates. The set of equations used to solve the shallow-water equations are found in section C.2 and comprises the hydrostatic pressure assumption, continuity and horizontal momentum equations, and turbulence closure model.

WAVES

DELFT3D models the forcing caused by short waves instead of modelling individual waves. The energy of these short waves travels with the group velocity. The short wave energy balance is given by (Deltares, 2018):

$$\frac{\partial E}{\partial t} + \frac{\partial}{\partial x} (EC_g \cos(\alpha)) + \frac{\partial}{\partial y} (EC_g \sin(\alpha)) = -D_w, \quad (2.31)$$

with E the short-wave energy, C_g the group celerity, α the wave direction, and D_w the dissipation of wave energy. Originally, DELFT3D is designed for irregular waves, as is the formulation for the energy dissipation. In contradiction with irregular waves, regular waves all break at the same location. Therefore, Schnitzler (2015) proposed an adaption of the current formulations for the energy dissipation based on the formulations by Van Rijn and Wijnberg (1996):

$$D_w = \frac{1}{4} \alpha_{rol} \rho_w g \frac{1}{T} H_{max}^2 Q_b, \quad (2.32)$$

with α_{rol} the roller dissipation coefficient, T the wave period, H_{max} the maximum wave height, and $Q_b = 1$ when waves break and $Q_b = 0$ when waves are not breaking. Q_b was adapted such that waves

break until the wave height has reached a relative depth:

$$\begin{cases} Q_b = 1 & \text{if } \frac{H_{rms}}{h} > \gamma \\ Q_b = 1 & \text{if } Q_{bx-1} = 1 \text{ and } H_{rms_{x+1}} > reldep \\ Q_b = 0 & \text{otherwise,} \end{cases} \quad (2.33)$$

with $\left(\frac{H_{rms}}{h}\right)$ the relative wave height, γ the wave breaking index. The maximum wave height H_{max} is given by:

$$H_{max} = \frac{0.88}{k} \tanh\left(\frac{\gamma}{0.88} kh_{ref}\right), \quad (2.34)$$

with k the wave number, γ the wave breaking index, and h_{ref} the water depth.

ROLLER ENERGY

When a wave breaks, its energy is transformed into roller energy. In shallow water regions this energy is quickly dissipated. Recent studies have shown that these effects can not be ignored, and even though the effect is not yet well understood, this conversion from wave motion to roller energy is given by the roller energy balance (Deltares, 2018):

$$\frac{\partial E_r}{\partial t} + \frac{\partial}{\partial x} (2E_r C \cos(\alpha)) + \frac{\partial}{\partial y} (2E_r C \sin(\alpha)) = D_w - D_r, \quad (2.35)$$

with E_r the roller energy and D_r the roller energy dissipation as function of the roller energy:

$$D_r = 2\beta_{rol} g \frac{E_r}{C}, \quad (2.36)$$

with β_{rol} a user-defined coefficient which is used to calibrate the undertow.

2.4.3.2 SUSPENDED SEDIMENT TRANSPORT

The suspended sediment transport rates are computed in DELFT3D by solving the three-dimensional advection-diffusion (mass-balance) equation (Deltares, 2018):

$$\frac{\partial c^{(l)}}{\partial t} + \frac{\partial uc^{(l)}}{\partial x} + \frac{\partial vc^{(l)}}{\partial y} + \frac{\partial (\omega - \omega_s^{(l)}) c^{(l)}}{\partial \sigma} = \frac{\partial}{\partial x} \left(\varepsilon_{s,x}^{(l)} \frac{\partial c^{(l)}}{\partial x} \right) + \frac{\partial}{\partial y} \left(\varepsilon_{s,y}^{(l)} \frac{\partial c^{(l)}}{\partial y} \right) + \frac{\partial}{\partial \sigma} \left(\varepsilon_{s,\sigma}^{(l)} \frac{\partial c^{(l)}}{\partial \sigma} \right) \quad (2.37)$$

with c the mass concentration of sediment fraction (l), u , v and ω velocity components, $\varepsilon_{s,x}^{(l)}$, $\varepsilon_{s,y}^{(l)}$ and $\varepsilon_{s,\sigma}^{(l)}$ the eddy diffusivities of sediment fraction (l), and $\omega_s^{(l)}$ the sediment settling velocity of sediment fraction (l). The velocities and horizontal and vertical diffusivity follow from the hydrodynamic computations and turbulence model.

REFERENCE CONCENTRATION

To compute the sediment concentration of a given fraction assuming a Rouse profile (Section C.2.5, Eq. C.2.5 and C.2.5) (Van Rijn, 2007c), first the reference concentration is calculated. For sediment fractions the approach by Van Rijn (2007c) is used, using a reference concentration given by:

$$c_a = 0.015 f_{silt,j} \frac{d_j T_j^{1.5}}{a D_{*,j}^{0.3}}, \quad (2.38)$$

with $f_{silt} = d_{sand}/d_j$ the silt factor ($f_{silt} = 1$ for $d_j > d_{sand} = 62\mu m$) and T_j the dimensionless bed-shear stress parameter. In DELFT3D this parameter is given by method D (eq. 2.21), where no correction factor for selective transport is incorporated. Finally, a is the reference level given by:

$$a = \max(0.5k_{s,c,r}, 0.5k_{s,w,r}), \quad (2.39)$$

with a minimum value of 0.01 m, and $k_{s,c,r}$ and $k_{s,w,r}$ given by equation A.2, assuming $k_{s,c,r} = k_{s,w,r}$ (section 2.4.1). A schematisation of the reference profile is provided in Figure 2.8.

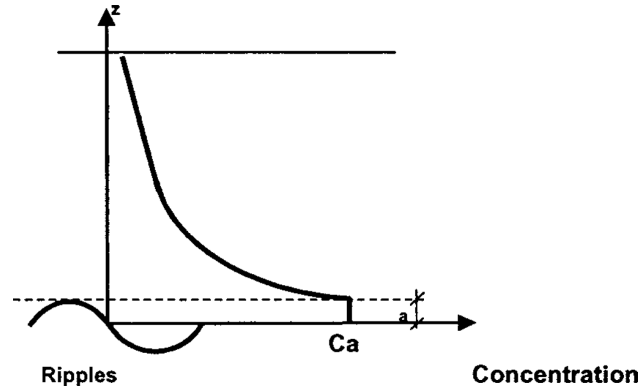


Figure 2.8: Schematisation of the reference concentration profile (Van Rijn, 2007c)

Finally, the current and wave-related suspended sediment transport are computed with:

$$q_{s,c} = \int_a^z u(z)c(z)dz, \quad (2.40)$$

$$q_{s,w} = \gamma V_{asym} \int_a^\delta c(z)dz, \quad (2.41)$$

where u is the velocity profile, c the concentration profile, $\gamma = 0.1$ the phase factor, δ the thickness of the suspension layer near the bed ($3\delta_s$) and V_{asym} the velocity asymmetry factor given by:

$$V_{asym} = \frac{[(U_{on}^4) - (U_{off}^4)]}{[(U_{on}^3) + (U_{off}^3)]}, \quad (2.42)$$

where U_{on} and U_{off} respectively are the onshore and offshore-directed peak orbital velocities.

2.5 DATA AND PREVIOUS EXPERIMENTS

A number of experiments have been carried out using graded sediment. These experiments were carried out in oscillatory flow tunnels where predominantly bed-load takes place, and in a wave flume where both bed-load and suspended-load is present. The facilities will be further explained together with the datasets in the following sections. The two datasets are:

1. The SANTOSS database (bed-load transport)
2. SINBAD experiments (bed-load and suspended transport)

2.5.1 THE SANTOSS DATABASE

Experiments for graded sediment have been carried out in oscillatory flow tunnels and the results have been included in the SANTOSS database (Van der Werf et al., 2009). The experiments by Hamm et al. (1998) and Hassan (2003) have been carried out in the Large Oscillating Water Tunnel (WL|Delft Hydraulics, The Netherlands) (LOWT) (Fig. 2.9), and the experiments by O'Donoghue and Wright (2004) were carried out in the Aberdeen Oscillatory Flow Tunnel (Aberdeen University, United Kingdom) (AOFT). Both facilities consist of a rectangular horizontal test section where the LOWT has a

height of 1.1m and the AOFT 0.75m. A piston generates oscillatory flows, creating a various number of flow conditions, with varying grain sizes and bed compositions. All experiments were carried out under sheet flow conditions without bed forms (ripples) where bed-load was predominating. The experiments were carried out with either two or three fractions. The results of the experiments with graded sediment as carried out by Hamm et al. (1998), Hassan (2003) and O'Donoghue and Wright (2004) are presented in Table 2.1. In this table, the first two columns specify the name of the experiments. Columns three till eight then specify the d_{50} and d_{mean} of the mixture (which is further elaborated on later in this chapter), which grain sizes are present within the mixture according to the classification presented in Table 2.2, and the distribution of the grain sizes. Columns nine till thirteen contain information about the wave characteristics, and the last four columns provide the measured transport rates per fraction and in total.

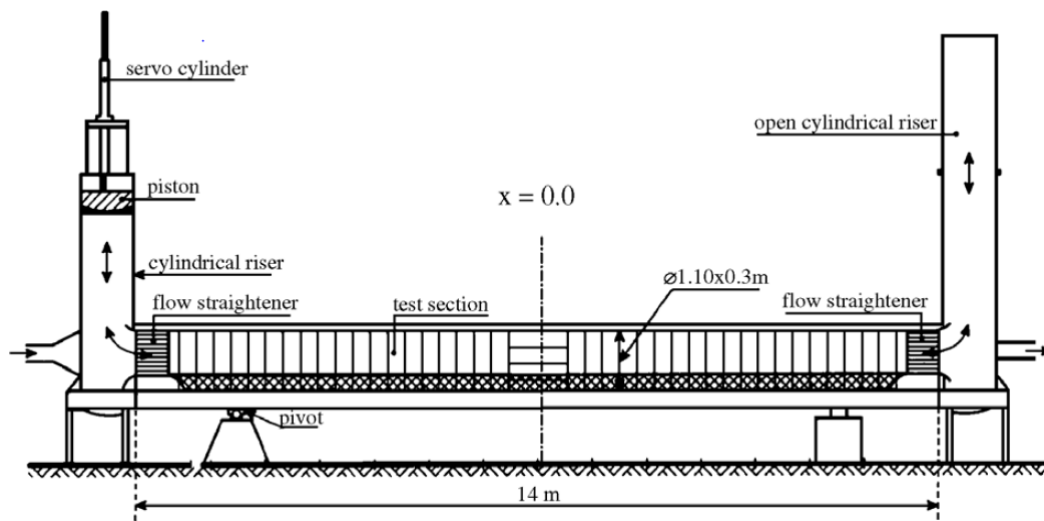


Figure 2.9: Schematisation of the Large Oscillating Wave Tunnel (WL|Delft Hydraulics, The Netherlands) (Hassan & Ribberink, 2005)

CLASSIFICATION OF GRAIN SIZES

Within the database three categories of grain sizes are distinguished, namely coarse, medium and fine. Table 2.1 displays the composition of the mixtures and what percentage of each grain size is present within the mixture. The fractions in these datasets have been classified according to the the classifications of Wentworth (1922) (Table 2.2).

Table 2.2: Classification of grain sizes based on findings by Wentworth (1922).

Subclass	mm	μm
Fine	0.0625 - 0.250	62.5 - 250
Medium	0.250 - 0.500	250 - 500
Coarse	0.500 - 2	500 - 2000

Table 2.1: Overview of the graded sediment cases within the SANTOSS database of Van der Werf et al. (2009). The bed form regime for all the data is sheet flow, with \hat{u} the maximum oscillatory flow velocity and $\langle u \rangle$ the steady current velocity. F, M and C denote respectively the Fine, Medium and Coarse grain size

Reference	Code	d_{50}	d_{mean}	F	M	C	Grain size distribution F - M - C	Type of wave	T	U_{rms}	\hat{u}	$\langle u \rangle$	q_f	q_m	q_c	q_s	
		[mm]															[-]
Hamm et al. (1998)	K1	0.19	0.22	0.13	0.32	-	50 - 50 - 0	2nd-order stokes	6.50	0.90	-	-	-1.7	36.5	-	34.8	
	K2							2nd-order stokes	6.50	0.60	-	-	3.9	13.1	-	17.0	
	K3							sawtooth	6.40	0.70	-	-	6.5	11.5	-	18.0	
	K5							sinusoidal	7.20	1.06	1.50	0.25	26.5	52.1	-	78.6	
	K6							sinusoidal	7.20	0.67	0.95	0.45	25.8	48.9	-	74.7	
	P6F							6.50	0.60				11.2	-	8.4	19.6	
Hassan (2003)	P7F	0.24	0.44	0.21	-	0.97	70 - 0 - 30		6.50	0.70			16.5	-	14.0	30.5	
	P9F								6.50	0.90			29.9	-	34.4	64.3	
	S45F								6.50	0.45	= 1.80	= 0.55	2.3	2.9	5.9	11.2	
	S6F								6.50	0.60			5.3	4.1	7.9	17.4	
	S7F	0.15	0.34	0.13	0.34	0.97	60 - 20 - 20		6.50	0.70			8.3	4.4	10.3	22.9	
	S9F								6.50	0.90			-9.8	6.8	18.4	15.4	
O'Donoghue and Wright (2004a,b)	S12F								12.00	0.70			8.5	4.2	8.0	20.8	
	X1A5010								5.00				-10.4	17.2	8.1	14.9	
	X1A7515	0.15	0.23				60 - 30 - 10		7.50				-5.0	16.1	9.7	20.8	
	X2A5010								5.00				-1.2	29.5	18.0	46.3	
	X2A7515	0.27	0.30	0.15	0.28	0.51	20 - 60 - 20	Asymmetric	7.50	0.90	= 1.50	-	-1.5	16.7	17.1	32.3	
	X4A5010								5.00				1.1	-	37.5	38.6	
X4A7515	0.26	0.33				50 - 0 - 50		7.50				-2.0	-	24.4	22.4		

d_{50} AND d_{mean}

The values of d_{50} as used in the experiments are presented with the other oscillatory flow tunnel data in Table 2.1. These values are based on the sieve curves where 50% of the mixture is finer than d_{50} . Additionally a weighted mean grain diameter is calculated ($d_{mean} = \sum p_j * d_j$) for every dataset. The dataset of Hassan (2003) yields a significant difference between d_{50} and d_{mean} . The grain size distributions for these experiments are given in Figure 2.10.

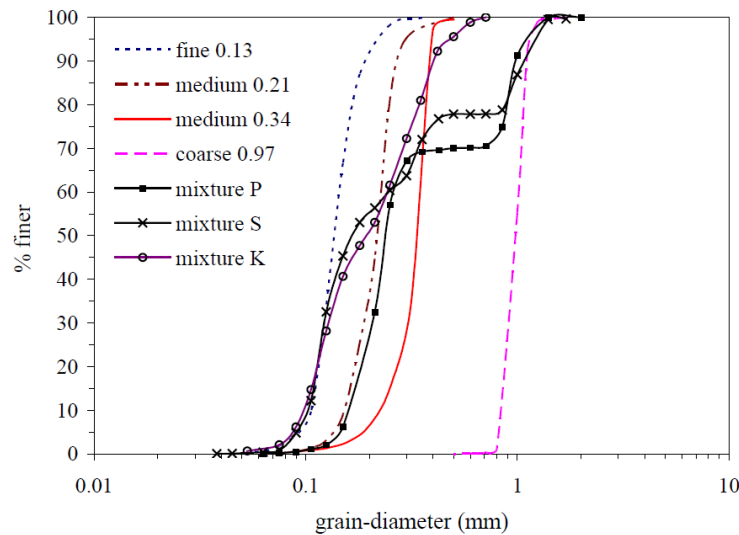


Figure 2.10: Grain size distributions of the sediment mixes used by Hassan (2003)

The first three experiments by Hassan (2003) consist of mixture P and the other five consist of mixture S. Mixture P contains medium sand (0.21 mm, brown dashed line) and coarse sand (0.97 mm, pink dashed line). Due to the large difference in grain size between these two fractions the distribution of this mixture has a flat zone, giving a d_{50} which is roughly halve the size of the mean diameter (d_{mean}). Mixture S contains fine sand (0.13 mm, blue dashed line), medium sand (0.34 mm, red solid line) and coarse sand (0.97 mm, pink dashed line). Due to the presence of three fractions the line of mixture S increases more gradually towards the coarse grain-diameter, reducing the flat zones between the different grain sizes.

2.5.2 SINBAD EXPERIMENTS

For the validation of the transport rates regarding both bed-load and suspended sediment transport the data from the SINBAD experiments is used. These experiments have been carried out in the CIEM wave flume in Barcelona and include graded sediment transport under breaking waves as carried out by Van der Zanden et al. (2017).

EXPERIMENTAL SET-UP

The testing area is 100m long and 3m wide and is presented in Figure 2.11. A wave paddle is located on the left ($x=0$ m) and the bed profile on its right consists of medium sized sediment, of which the sieve curve is given in Figure 2.13. Between $x=50$ and 60m a breaker bar is located, with a sloping bed on its left (1:10), and a fixed slope on its right ($x>68$ m). The experiments were carried out with monochromatic waves over a timespan of 90 minutes (6 runs of 15 minutes), where the evolution of the bed profile was measured every 30 minutes.

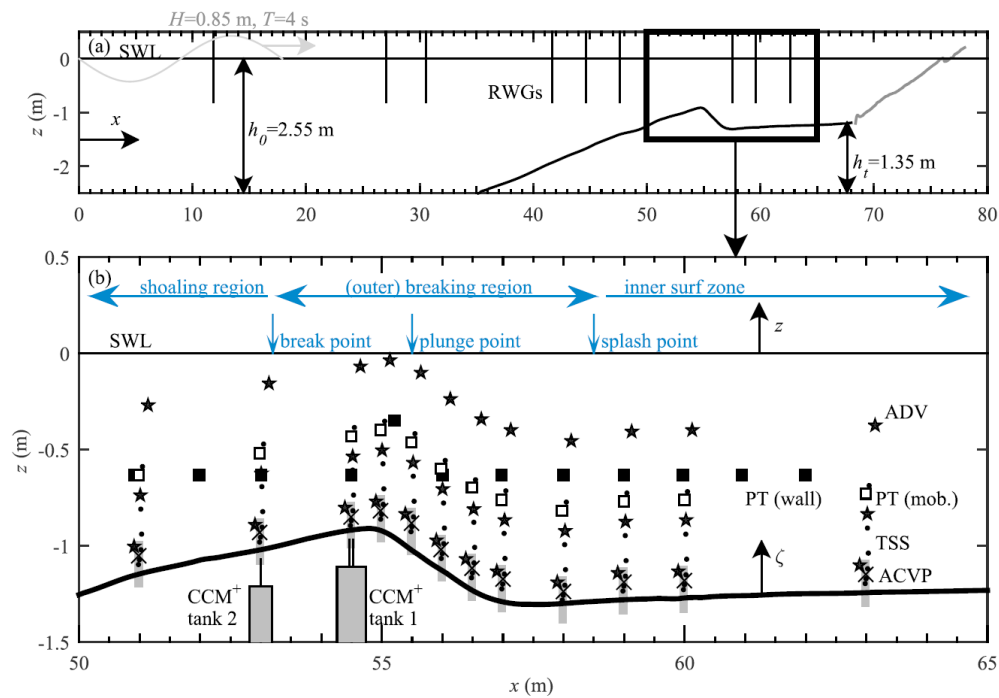


Figure 2.11: Set-up of the SINBAD experiment (Van der Zanden et al., 2017). With in the top figure the bed profile (black) and fixed slope (grey). The lower figure zooms in on the breaker bar and shows the measurement locations (squares, stars, crosses and dots) and defines the different regions.

INSTRUMENTATION

The hydrodynamics are calibrated for the wave height, undertow and kinetic energy. The sediment transport is then validated in terms of the suspended sediment concentrations and grain sizes in the water column, followed by the validation of the cross-shore net total sediment transport. The data required for these steps are obtained by the measuring equipment shown in Table 2.3. For each instrument the name is given, the measuring locations above the bed, and where the data is used for.

Table 2.3: Measuring equipment as used during the SINBAD experiments Van der Zanden (2016).

Instrument	Elevation ζ [m]	Used for the validation of:
Acoustic Doppler Velocimeters (ADVs)	0.11, 0.38, 0.85	Undertow, Turbulent Kinetic Energy
High-Resolution Acoustic Concentration and Velocity Profiler (ACVP)	0.12	Undertow, Turbulent Kinetic Energy, Concentrations
Pressure Transducer (PT)	0.48	Wave height
Resistive Wave Gauges (RWGs)	Water surface level	Wave height
Transverse Suction System (TSS) nozzles	0.02, 0.04, 0.10, 0.18, 0.31, 0.53	Concentrations, Grain sizes
Echo Sounders	-	Bed profile
Manually taken bed samples after $t = 90$ min at 12 locations, by collecting 1 to 2cm of top layer	-	Bed composition

REGULAR BREAKING WAVES

During the experiments regular waves were imposed on the left boundary, which break on the breaker bar. As implied in Figure 2.11, the water depth $h_0 = 2.55m$, the wave height $H_0 = 0.85m$ and the wave period $T = 4s$, where in the lower sub-figure the different regions of the wave breaking process are indicated. In Figure 2.12 a schematisation of the development of a breaking wave is presented. Please note that the wave propagation is represented in the opposite direction (from right to left) from Figure 2.11 where the waves approaches from the left.

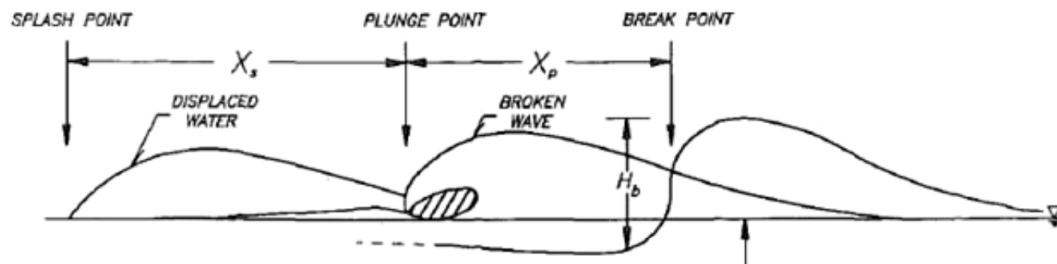


Figure 2.12: The development of a breaking wave after its break point (Smith & Kraus, 1991)

SIEVE CURVE

The sediment used in the experiments has been sieved in the CIEM lab, where the cumulative distribution of 11 grain sizes was obtained (Table D.1). As linear interpolation does not seem fit in this case, a Piecewise Cubic Hermite Interpolating Polynomial (pchip) is fitted through the data points, obtaining the sieve curve as shown in Figure 2.13. Even though the sieve data is now considered to be reliable, it should be taken into account that it is still possible that there are errors in the measurements.

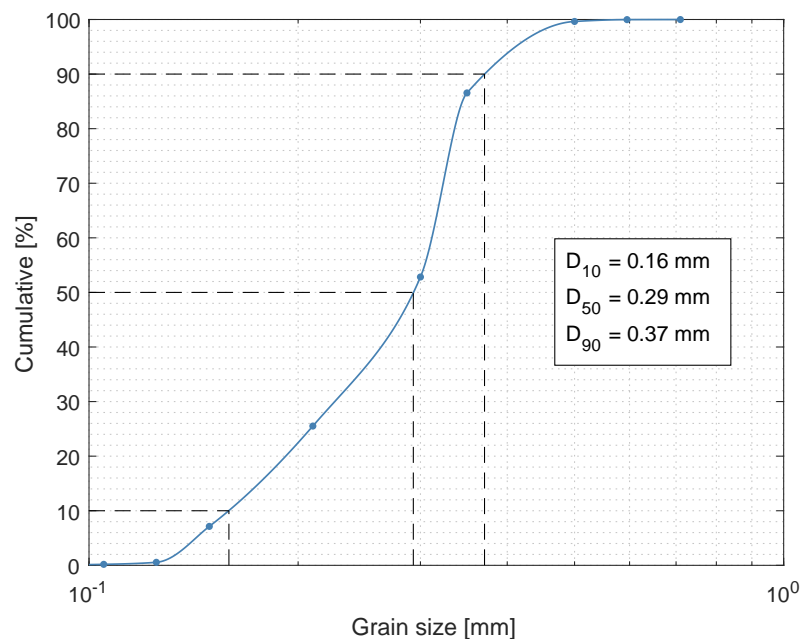


Figure 2.13: Cumulative grain size distribution as used in the SINBAD experiments obtained by sieving tests.

NET SEDIMENT TRANSPORT

The volumetric total sediment transport rates $q_{tot}(x)$ were determined by measuring the changes in the bed-profile and solving the Exner equation:

$$q_{tot}(x) = q_{tot}(x - \Delta x) + \Delta x(1 - \varepsilon_0) \frac{\Delta z_{bed}(x)}{\Delta t} \quad (2.43)$$

Where Δx is the horizontal resolution of z_{bed} measurements (=0.02 m), ε_0 the porosity (=0.4), $\Delta z_{bed}(x)$ the change in bed level and Δt the time interval between two measurements (=30 min.). The bed-load transport rates are then determined by subtracting the suspended sediment transport rates from the total net transport rates.

BED-LEVEL EVOLUTION AND CROSS-SHORE SORTING

Before any measurement were done regarding transport rates, waves were generated for 105 minutes to create a reference profile (Van der Zanden et al., 2017). At the start (t=0 min.) and end (t=90 min.) the bed profile was measured, showing accretion on the breaker-bar and erosion behind this bar. Additionally, fining has taken place on top of the breaker-bar (x=55.5 m), with coarsening right before the top of the bar (x=54.5 m).

VALIDATION OF THE BED-LOAD TRANSPORT MODELS

The results of the validation of both the SANTOSS and Van Rijn model are presented in this chapter in order to answer **research question 1**. First, the results of the Van Rijn model are shown for different settings. Next, the same is done for the SANTOSS model. For both models the best setting is chosen, where after in the last paragraph the best setting of both models are compared and discussed.

3.1 VAN RIJN MODEL

For this thesis project the Van Rijn formulations for graded sediment transport as already incorporated in Fortran (TR2004 (Van Rijn et al., 2004), with the formulae as described in Van Rijn (2007a, 2007b, 2007c)) are converted to MATLAB. In the Fortran code wave-induced near-bed streaming has been embedded (Van Rijn et al., 2003), which is considered to be absent in oscillatory flow tunnels as there are no progressive waves. Incorporating streaming effects in both the Fortran and MATLAB model, gives comparable results for both models with slightly higher transport rates for the MATLAB model (Fig. F.2). These small differences are due to tweaking parameters used in the Fortran code, which are now excluded in MATLAB, following the formulations used by (Van Rijn, 2007a, 2007b, 2007c). For the default case used by Van Rijn (2007c), using method A for the dimensionless bed-shear stress, a grain roughness of $k_s = d_j$ and a representative grain diameter of $d_{rep} = d_{50}$ the MATLAB model gives net transport rates half the magnitude of those computed by Fortran due to the exclusion of streaming effects. The transition from Fortran to MATLAB is further elaborated on in Appendix F. In the current section the modelled results are validated with measured transport rates as included in the SANTOSS database (Table 2.1). This is done for the following model settings:

1. Model setting 1: Graded approach

The representative grain diameter of the entire mixture can either be based on d_{50} or d_{mean} (Section 2.5.1). Using a graded approach (Section 3.1.2), a distinction is been made between the grain sizes of the different fractions. The representative grain diameter which gives the best results is chosen, and used for setting 3 and 4.

2. Model setting 2: Uniform approach

The model does not recognise the different grain sizes of the fractions and treats the mixture as if it is uniform, such that only one d_{50} is used for the mixture (Section 3.1.1).

3. Model setting 3: Roughness approach

The approach for the grain-related roughness is modified (Section 3.1.3), using the best setting of model setting 1.

4. Model setting 4: Selective transport

The correction factor for the effective grain-shear stress by Day (1980) and hiding and exposure factor of Egiazaroff are switched off (Section 3.1.4), using the best setting of model setting 1.

An overview of these four main settings with their sub settings is provided in Table 3.1. The performance of the model regarding the net transport rates per model setting is presented in Table 3.2 at the end of this chapter, with the results per fraction in Table F.3 in appendix F.

Table 3.1: Different model settings to compute the net transport rates with the Van Rijn model. d_{rep} denotes the representative grain diameter of the entire mixture, d_j the grain size used per fraction, T_j the method for the dimensionless bed-shear stress parameter (Section 2.4.1), k_s the approach used for the grain roughness, $\tau_{b,cr}$ the critical bed-shear stress (section 2.4.1), and *Section* in which section the results are presented and discussed. The best setting is denoted in grey.

Name	Setting No. #	d_{rep}	d_j	T_j	k_s	$\tau_{b,cr}$	Section
Graded approach	1.1	d_{50}	d_j	A	d_j	$\left(\frac{d_j}{d_{rep}}\right) \tau_{b,cr,d_{rep}}$	3.1.2
	1.2	d_{mean}	d_j				
Uniform approach	2.1	d_{50}	-	-	d_j	$\left(\frac{d_j}{d_{rep}}\right) \tau_{b,cr,d_{rep}}$	3.1.1
	2.2	d_{mean}					
Grain roughness	3.1	d_{50}	d_j	A	d_{90}	$\left(\frac{d_j}{d_{rep}}\right) \tau_{b,cr,d_{rep}}$	3.1.3
	3.2	d_{mean}	d_j				
Selective transport	4.1	d_{50}	d_j	B	d_j	$\left(\frac{d_j}{d_{rep}}\right) \tau_{b,cr,d_{rep}}$	3.1.4
	4.2	d_{50}	d_j	C	d_j	τ_{b,cr,d_j}	
	4.3	d_{50}	d_j	D	d_j	τ_{b,cr,d_j}	
	4.4	d_{mean}	d_j	B	d_j	$\left(\frac{d_j}{d_{rep}}\right) \tau_{b,cr,d_{rep}}$	
	4.5	d_{mean}	d_j	C	d_j	τ_{b,cr,d_j}	
	4.6	d_{mean}	d_j	D	d_j	τ_{b,cr,d_j}	

DEFAULT SETTING VAN RIJN

Regarding method A for the dimensionless bed-shear stress parameter which incorporates the correction factor by Egiazaroff and a correction factor for the effective grain-shear stress, the model seems to give accurate results for steady flow with the presence and absence of waves (Van Rijn, 2007c). Additionally, using a grain roughness of d_j yields better results for very graded beds, hence A_j (method A, where the subscript denotes the roughness approach d_j) is the standard setting used by Van Rijn (2007c). Furthermore $d_{rep} = d_{50}$, which makes A_j using d_{50} the initial setting used within this section.

3.1.1 GRADED VERSUS UNIFORM SAND APPROACH

Distinguishing between different fractions instead of using one grain size for the entire mixture, will show to what extend graded effects do play a role within the Van Rijn model using the SANTOSS database. When assuming only one fraction, the formula for the dimensionless bed-shear stress parameter for all four methods simply transforms into:

$$T_j = \frac{[\tau'_{b,cw} - \tau_{b,cr}]}{\tau_{b,cr}} \quad (3.1)$$

The initial setting, using method A with grain roughness d_j and a representative grain diameter of d_{50} , is compared to the setting where the mixture is treated as uniform sediment. This uniform sediment also uses a representative grain diameter of d_{50} and a grain roughness of d_{50} as no distinction is made between the roughness per fraction.

MODELLED TRANSPORT RATES

In Figure 3.1 the calculated transport rates are plotted as function of the measured transport rates, where the black solid line denotes the line of perfect fit and the black dashed line the Factor 2 interval.

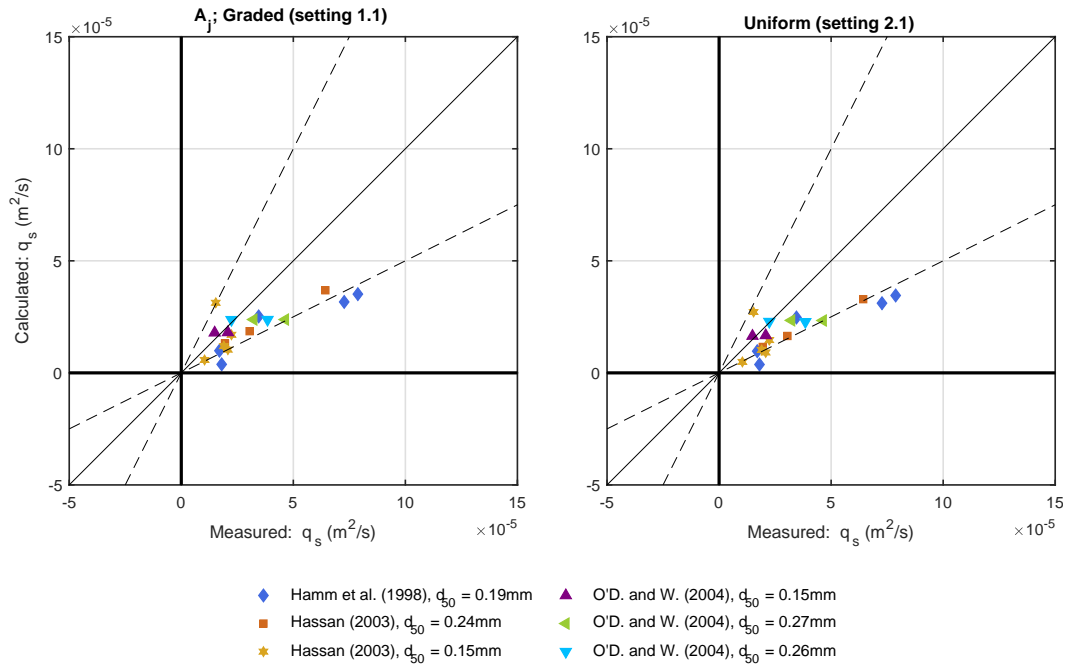


Figure 3.1: Net total transport rates for the graded (setting 1.1) and uniform (setting 2.1) approach using a representative grain diameter of d_{50} . Setting 1.1 uses method A for the dimensionless bed-shear stress parameter and d_j for the grain related roughness, hence A_j .

Comparison of the net total transport rates of both the graded and uniform sand approach shows that the differences in transport rates between these two settings are limited. This might be due to a number of factors, namely how the transport rates are affected by the choice of formula for the dimensionless bed-shear stress parameter, how the critical and effective bed-shear stress are determined, how the grain-related roughness affects the sediment transport rates, or how hiding and exposure is incorporated in the model. The performance of the different settings is presented in Table 3.2.

3.1.2 GRADED APPROACH USING A REPRESENTATIVE GRAIN DIAMETER OF d_{50} OR d_{mean}

When using a graded approach, a representative grain diameter of either d_{50} or d_{mean} can be used (section 2.5.1). The computed net transport rates using different representative grain diameters are presented in Figure 3.2 and the transport rates per fraction in 3.3. In the figures presenting the transport rates per fraction, a total of 47 data points are presented.

Figure 3.2 shows that the transport rates modelled for the datasets by Hassan (2003) give the largest differences between the two approaches, which can be attributed to the difference between d_{50} and d_{mean} . Higher values for the representative grain size yield higher transport rates, mainly due to higher transport rates of the fine fraction, as shown in Figure 3.3. Overall, using d_{mean} gives better results as presented in Table 3.2 with exception of r^2 . Hence the graded approach using $d_{rep} = d_{mean}$ is set as the default setting to which the other settings are compared in the following sections.

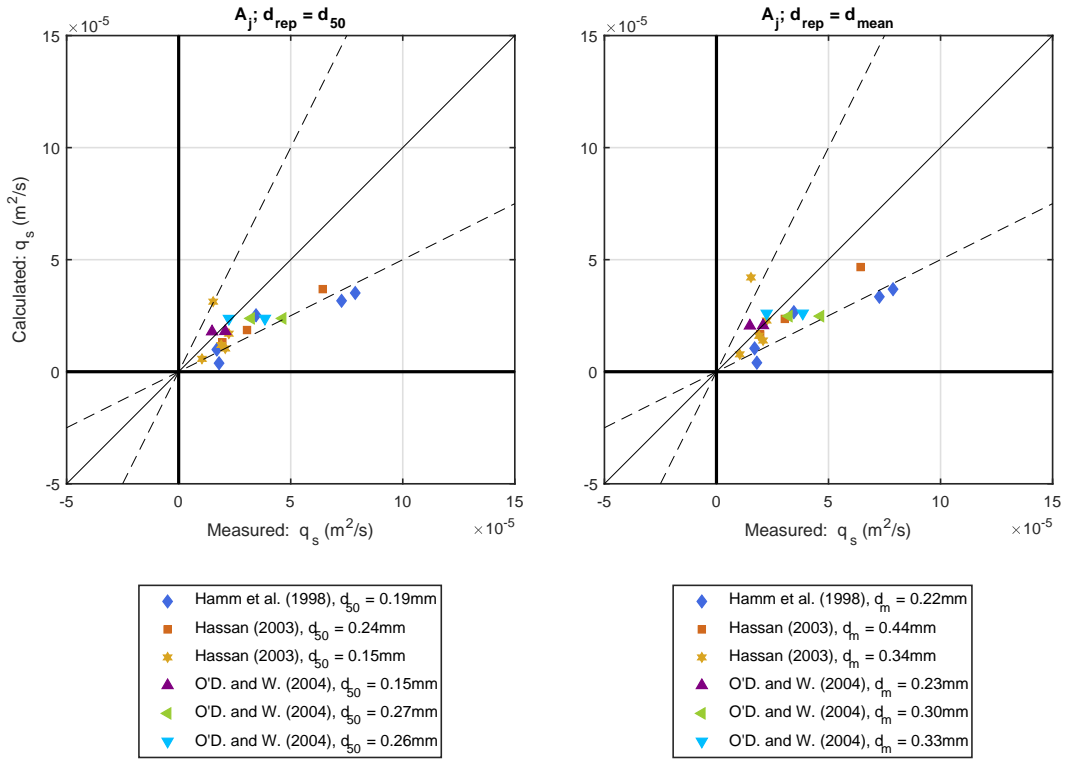


Figure 3.2: Net total transport rates for representative grain diameters of respectively d_{50} (setting 1.1) and d_{mean} (setting 1.2). The settings use method A for the dimensionless bed-shear stress parameter and d_j for the grain related roughness, hence A_j .

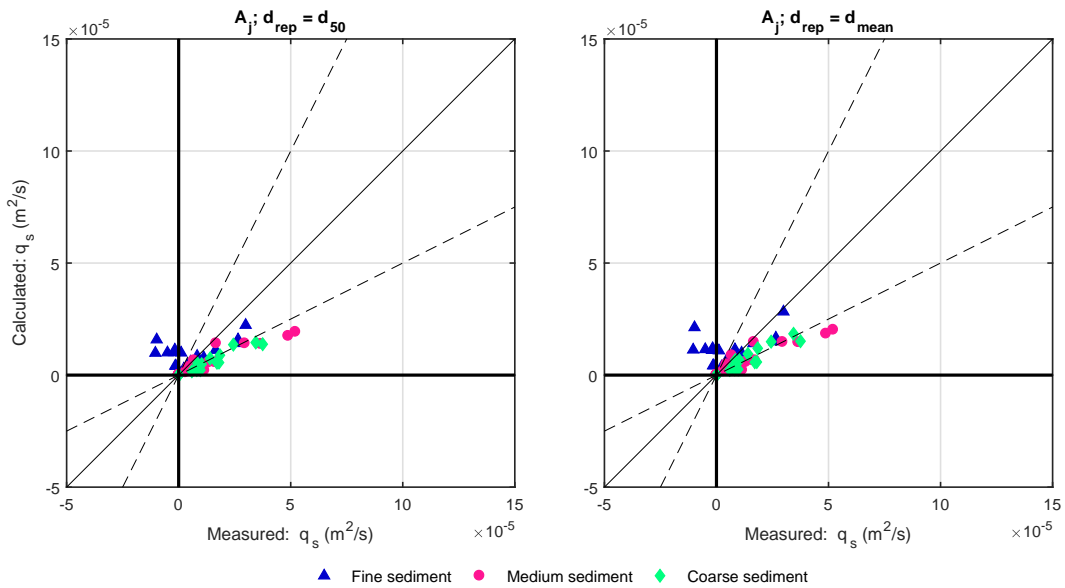


Figure 3.3: Net transport rates per fraction for the d_{50} and d_{mean} approach. The settings use method A for the dimensionless bed-shear stress parameter and d_j for the grain related roughness, hence A_j .

3.1.3 EFFECT OF ROUGHNESS SETTINGS

The grain roughness (k_s) used to determine the current-related friction factor and the wave-related friction factor can either be based on d_{90} or d_j according to Van Rijn (2007c). To investigate the effect of the roughness, the transport rates of method A using a grain roughness of either d_{90} or d_j are compared.

MODELLED TRANSPORT RATES

The transport rates for a representative grain diameter of d_{mean} using different grain roughness approaches as presented in Figure 3.4 and 3.5, show that the transport rates have increased for $k_s = d_{90}$. This is due to an increased current-related and wave-related roughness ($f'_{c,j}$ Eq. 2.11 and $f'_{w,j}$ Eq. 2.13), resulting in higher values for T_j and $\tau'_{b,cw}$, which positively feed into the equation for bed-load transport (Eq. 2.2).

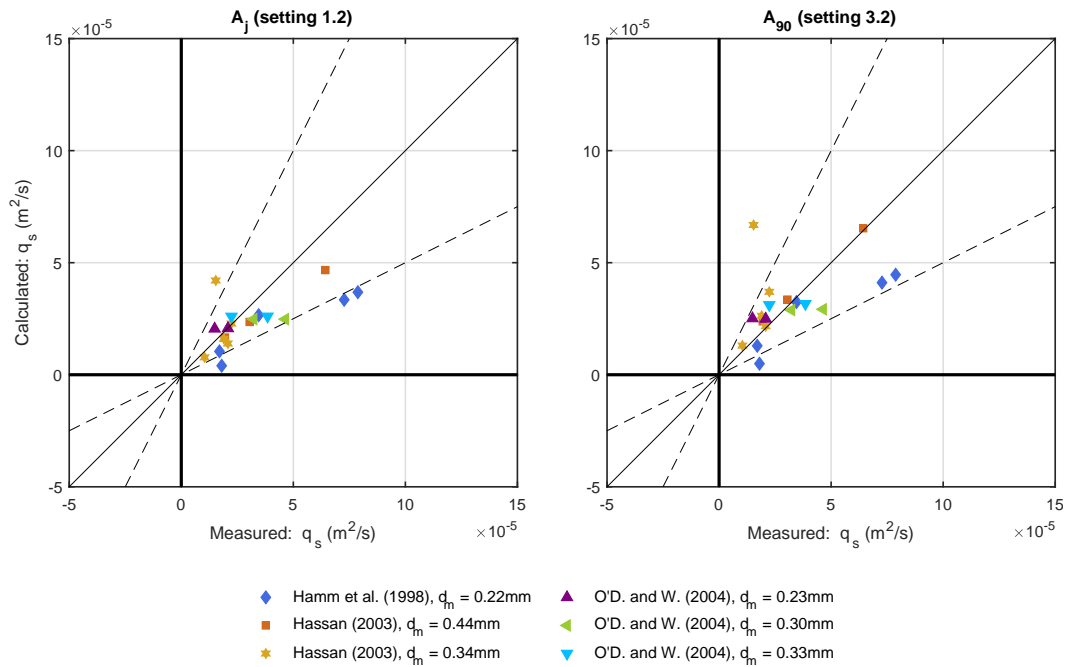


Figure 3.4: Net total transport rates for different settings for the grain roughness, using $d_{rep} = d_m$. Setting 1.2 and 3.2 use method A for the dimensionless bed-shear stress parameter and d_j or d_{90} for the grain related roughness, hence A_j and A_{90} .

For the net total transport rates, the r^2 and RMSE are better when $k_s = d_j$, though the Factor 2 criterion gives a better score when $k_s = d_{90}$, which is due to the calculated transport rates for the experiments by Hassan (2003) which are now computed within the Factor 2 interval.

The transport rates per fraction (Fig. 3.5) show that the fine fraction is affected the most by the different roughness approaches. For this fraction the difference between d_j and d_{90} is larger, with $k_s = d_{90}$ yielding higher transport rates. Analysis of the performance per fraction (Table F.3) shows that for the Bias and r^2 the worst results are given for the fine fraction, mainly due to the large scatter and the high magnitude of the transport rates modelled in the erroneous direction. The RMSE values for the fine fraction are affected the most by the different approaches, giving better results for a grain roughness of d_j . The Factor 2 criterion gives varying results for the different fractions, where better values are obtained for the medium and coarse fraction using a grain roughness of d_{90} . This may be

attributed to the fact that the difference between d_{90} and d_j is smaller for the medium and coarse fraction, which has now resulted in favourable results for d_{90} , mainly when the transport rates are low. According to (Van Rijn, 2007c), in case of well-mixed bed material the grain roughness is the best approached by a constant value of $k_s = d_{90}$. Whenever the bed consists of segregated fractions, this roughness is better approached by $k_s = d_j$. Since both the RMSE and Factor 2 criteria give significantly better values for the fine fraction using $k_s = d_j$ (difference of $0.06 * 10^{-4} m^2/s$ and 16%), and for the net total transport there is only a difference of 10% for the Factor 2 criterion in favour of $k_s = d_{90}$, $k_s = d_j$ is assumed to be the best approach. Therefore, the bed is not considered to be well-mixed.

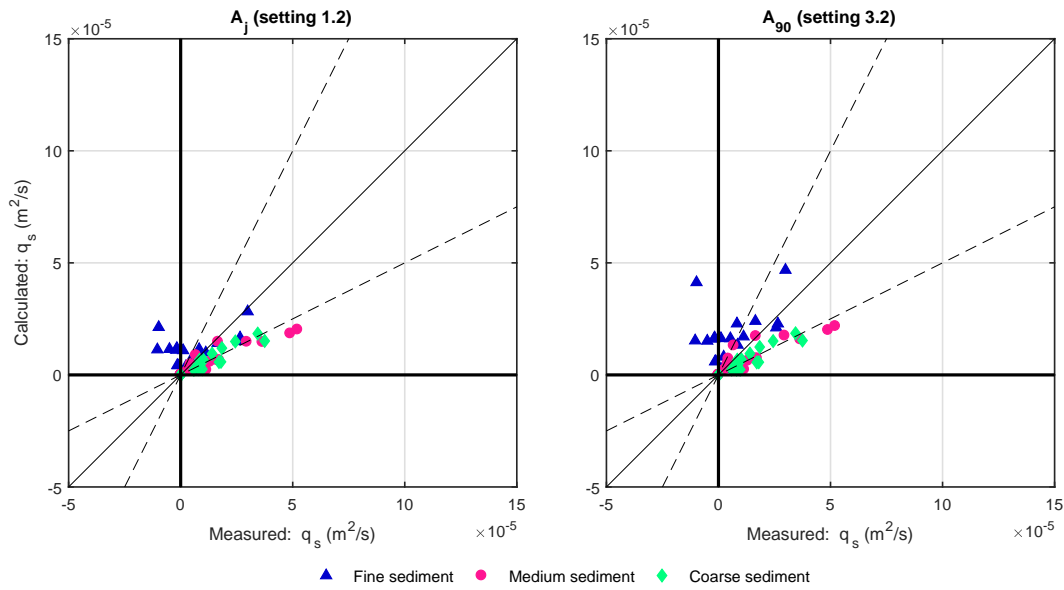


Figure 3.5: Net transport rates per fraction for different settings for the grain roughness, using $d_{rep} = d_{mean}$. Setting 1.2 and 3.2 use method A for the dimensionless bed-shear stress parameter and d_j or d_{90} for the grain related roughness, hence A_j and A_{90} .

3.1.4 EFFECT OF SELECTIVE TRANSPORT

Selective transport is incorporated in the model through two factors:

1. A correction factor for the effective grain-shear stress (λ_j , Eq. 2.17) by Day (1980).
2. A hiding and exposure factor (ξ_j , Eq. 2.16) by Egiazaroff (1965).

Whereas λ_j increases with an increasing relative grain size and is a multiplication factor for the dimensionless bed-shear stress parameter T_j in method A (Eq. 2.18), ξ_j decreases with an increasing relative grain size. ξ_j is a multiplication factor for the critical bed-shear stress, and thus increases the critical bed-shear stress for fine particles as they may be hidden behind larger particles and decreases the critical bed-shear stress for the coarse particles as they are more exposed to the flow. Both factors as function of the relative grain size using $d_{rep} = d_{mean}$ are given in Figure 3.6.

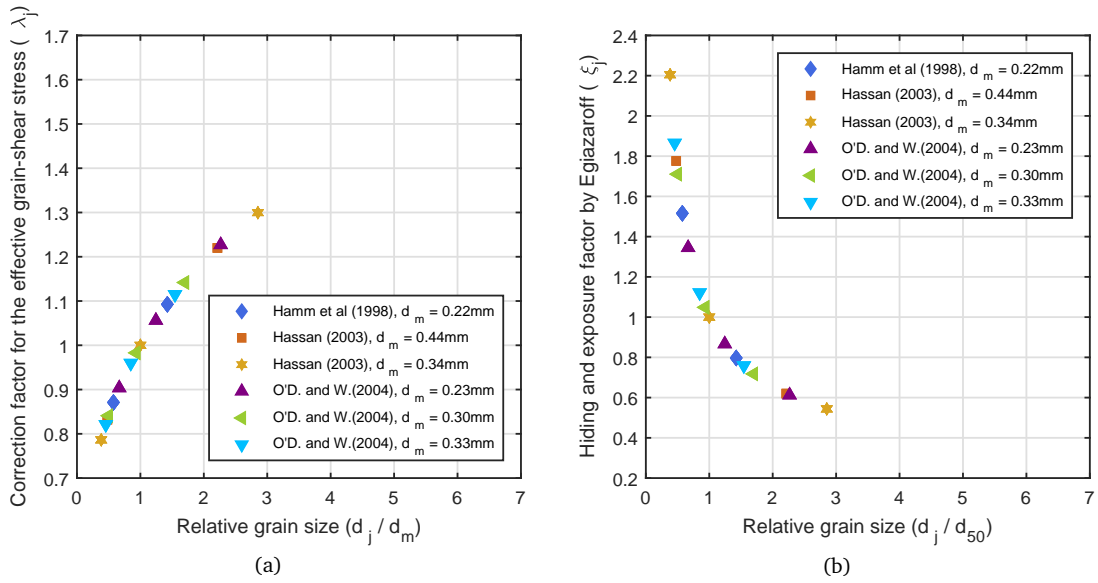


Figure 3.6: (a) The correction factor for the effective grain-shear stress and (b) the hiding and exposure factor by Egiazaroff as function of the relative grain size. Please note that both y-axes use different limits.

In this section first the effect on the critical bed-shear stress by the hiding and exposure factor of Egiazaroff (ξ_j) is investigated. This is done for both approaches for the critical bed-shear stress, using either $\xi_j \left(\frac{d_j}{d_{rep}} \right) \tau_{b,cr,d_{rep}}$ or $\xi_j \tau_{b,cr,d_j}$. Hereafter the computed transport rates using different methods for the dimensionless bed-shear stress parameter are presented.

CRITICAL BED-SHEAR STRESS $\tau_{b,cr}$

The critical bed-shear stress is either be based on the d_{rep} approach $\left(\left(\frac{d_j}{d_{rep}} \right) \tau_{b,cr,d_{rep}} \right)$ or the d_j approach (τ_{b,cr,d_j}) . Methods A and B make use of a multiplication factor for the critical bed-shear stress $\left(\frac{d_j}{d_{rep}} \right)$ to account for grading. Methods C and D use a critical bed-shear stress determined per fraction. The critical bed-shear stress times the hiding and exposure factor of Egiazaroff as used in methods A, B and C is plotted in Figure 3.7a. The blue and green dots depict the d_{rep} approach $\left(\xi_j \left(\frac{d_j}{d_{rep}} \right) \tau_{b,cr,d_{rep}} \right)$ and the yellow and red triangles the d_j approach $(\xi_j \tau_{b,cr,d_j})$, using a representative grain diameter of d_{mean} . The solid black line defines the critical bed-shear stress for uniform sediment. In Figure 3.7b the ratio of between the instantaneous bed-shear stress and critical bed-shear stress is plotted as function on the grain size.

Figure 3.7a shows that the critical bed-shear stress is higher for fine sand and is lower for coarse sand when compared to uniform sand. Due to the correction factor of Egiazaroff, the mobility is decreased for fine sand and increased for coarse sand, accounting for grading effects. Furthermore, the d_{rep} approach shows results closer to the uniform sand approach, whereas the d_j approach shows a larger deviation from this line as the critical bed-shear stress is determined for each grain size specifically. Figure 3.7b shows that the instantaneous bed-shear stress can become relatively high compared to the critical bed-shear stress. The range varies between a ratio of approximately 2 and 27. In Appendix F the correction factors for $d_{rep} = d_{50}$ and the critical bed-shear stress per dataset for the different approaches using either $d_{rep} = d_{mean}$ or d_{50} are presented.

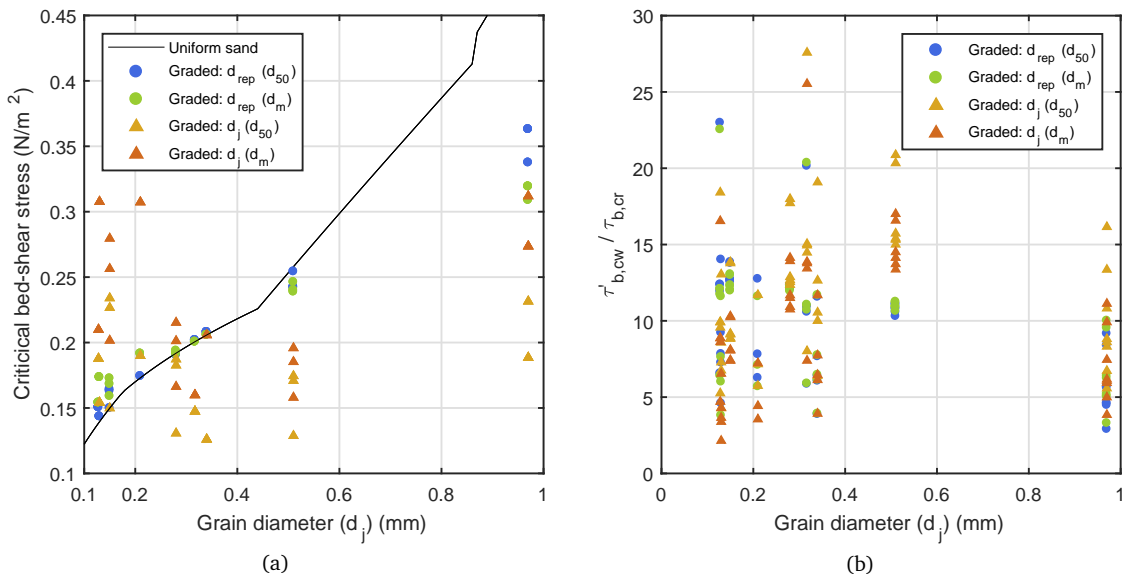


Figure 3.7: Analysis of the critical bed-shear stress using the experiments from the SANTOSS database, with (a) the critical bed-shear stress times the hiding and exposure factor of Egiazaroff (Eq. 2.16), $\tau_{b,cr} * \xi_j$, as function of the grain diameter d_j . With in blue and green the d_{rep} approach respectively using $d_{rep} = d_{50}$ and d_{mean} as used in Method A and B (Eq. 2.18 and 2.19). Yellow and red depict the d_j approach respectively using $d_{rep} = d_{50}$ and d_{mean} as used in Method C (Eq. 2.20). The black line denotes the critical bed-shear stress for uniform sand. (b) shows the ratio between the instantaneous and critical bed-shear stress, by dividing the former by the latter, as function of the grain size.

MODELLED TRANSPORT RATES

Figure 3.8 and 3.9 (on page 31 and 32) show the transport rates for methods A, B, C and D using a grain roughness of d_j and $d_{rep} = d_{mean}$. To examine the effect of (1) the correction factor for the effective grain-shear stress by Day (1980), (2) the hiding and exposure factor by Egiazaroff (1965) and (3) the different approaches for the critical bed shear stress, the methods are compared below.

1. Correction factor for the effective grain-shear stress λ_j : Method A and B

The only difference between method A and B is the correction factor for the effective grain-shear stress, which is included in method A and excluded from method B. The total net transport rates (Fig. 3.8) hardly shows any differences between the two methods, with limited reduction of the transport rates when the correction factor is excluded. The transport rates per fraction (Fig. 3.9) are also hardly affected by the different methods, with a small decrease in transport rates for the medium and coarse fraction when the correction factor is incorporated.

2. Hiding and exposure factor by Egiazaroff ξ_j : Method C and D

The hiding and exposure factor by Egiazaroff is included in method C and excluded from method D. The total net transport rates and transport rates per fraction (Fig. 3.8 and 3.9) show no large differences between the methods. Figure 3.7 shows that the ratio between the critical bed-shear stress and the actual bed-shear stress can become very large. This means that a small change of the critical bed-shear stress due to the correction factor of Egiazaroff is almost negligible compared to the actual bed-shear stress. Therefore this correction factor hardly affects the transport rates.

3. Critical bed-shear stress: Method B and C

Method B and C use different approaches for the critical bed-shear stress. Method B uses $\left(\frac{d_j}{d_{rep}}\right) \tau_{b,cr,d_{rep}}$ whereas method C uses τ_{b,cr,d_j} . Regarding the net total transport rates method C yields slightly higher values. In Figure 3.9 these differences are more evident, as for method C the rates have increased for the coarse and medium fraction and decreased for the fine fraction. The calculated net total transport rates for the datasets of Hassan (2003) show the largest decrease when method C (τ_{b,cr,d_j}) is applied. Especially the transport rates of the fine fraction decrease when method C is applied, with a small increase for the other fractions.

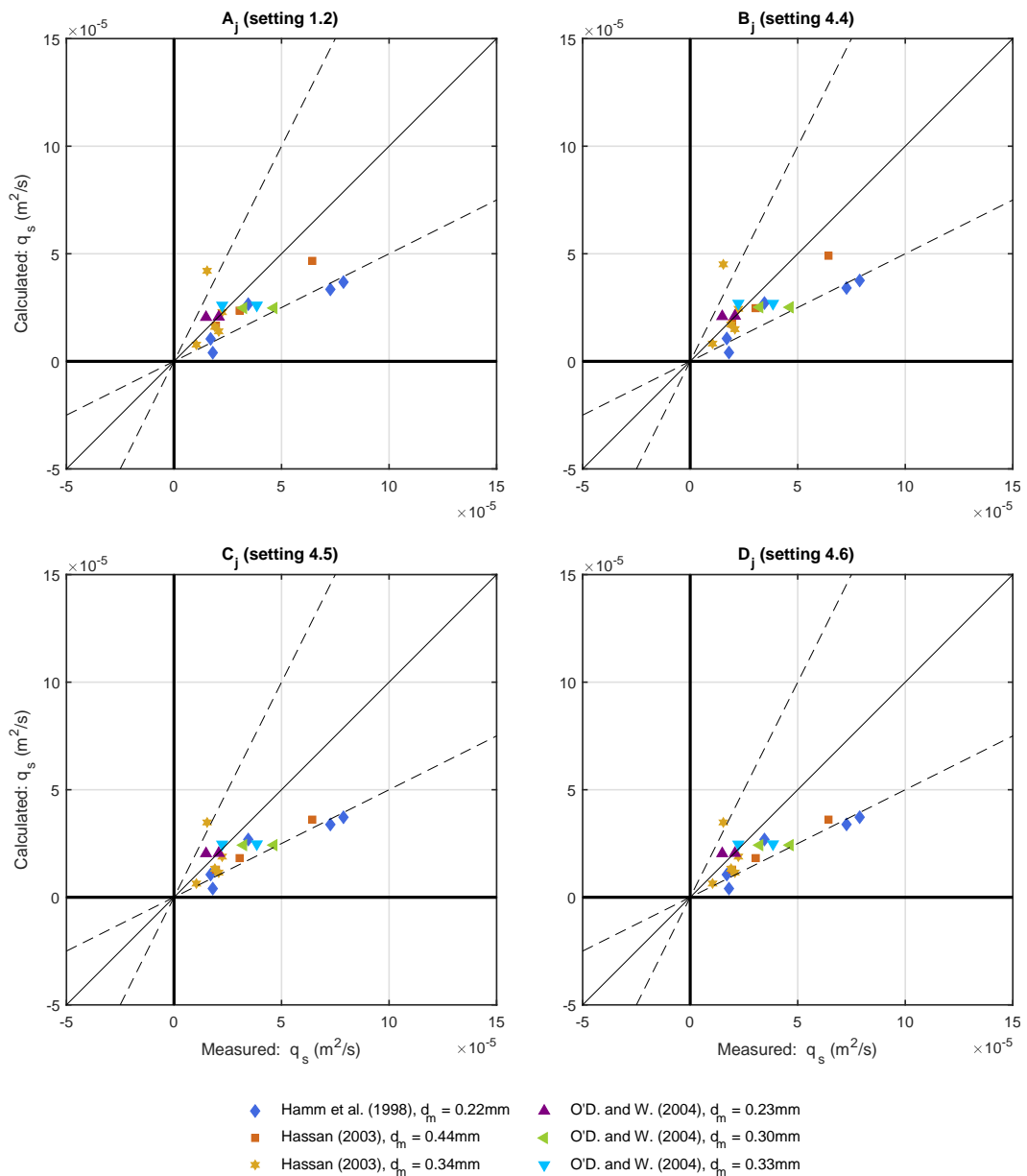


Figure 3.8: Net total transport rates for different settings for grain roughness and critical bed-shear stress, using $d_{rep} = d_{mean}$. Setting 1.2, 4.4, 4.5 and 4.6 respectively use method A, B, C or D for the dimensionless bed-shear stress parameter and d_j for the grain related roughness, hence A_j , B_j , C_j and D_j .

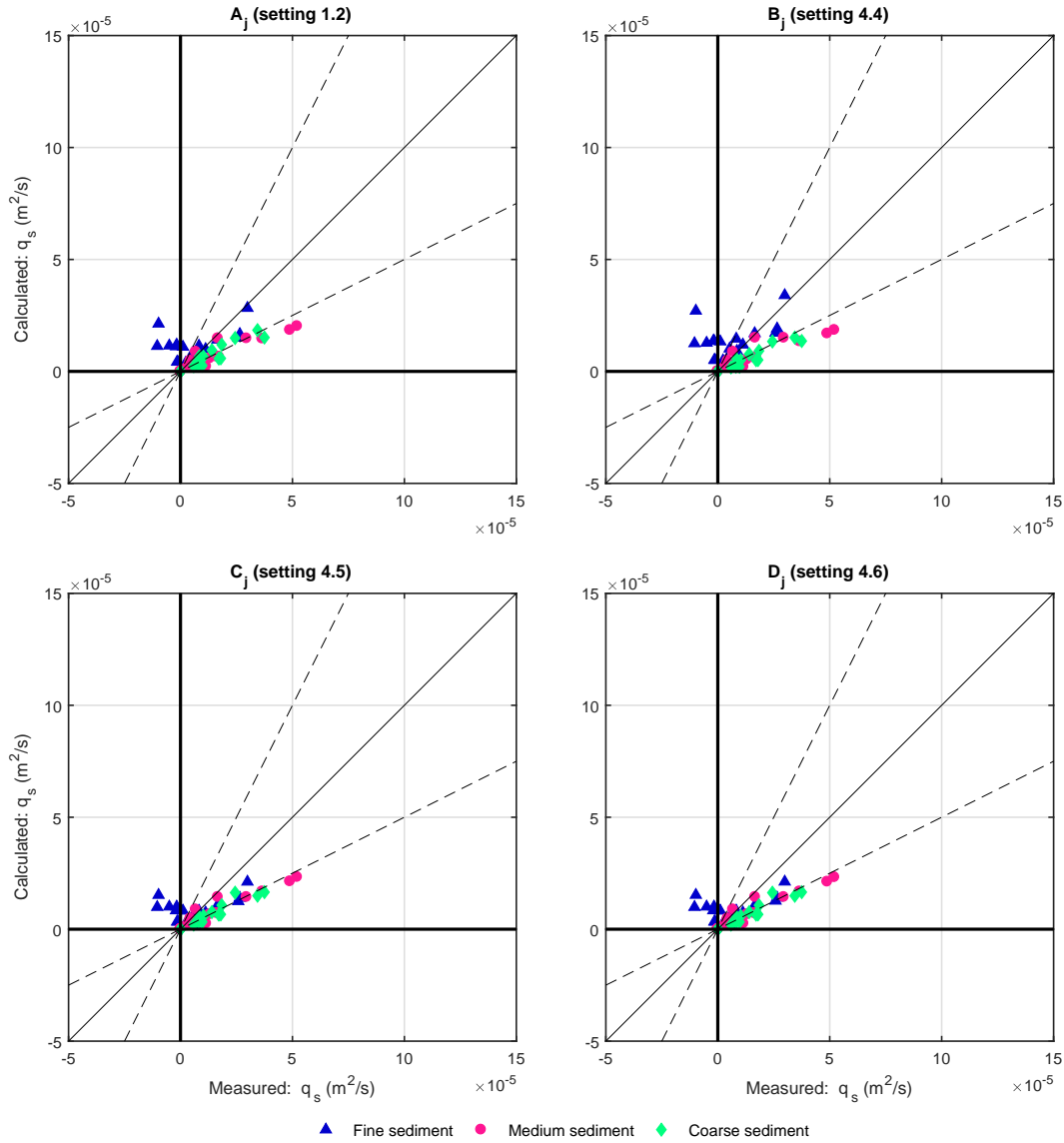


Figure 3.9: Net transport rates per fraction for different settings for grain roughness and critical bed-shear stress, using $d_{rep} = d_{mean}$. Setting 1.2, 4.4, 4.5 and 4.6 respectively use method A, B, C or D for the dimensionless bed-shear stress parameter and d_j for the grain related roughness, hence A_j , B_j , C_j and D_j .

COMPARISON OF ALL DIFFERENT METHODS

Table 3.2 shows the performance of the different model settings based on the net total transport rates, giving comparable results for all four methods, with better results for the RMSE and Factor 2 using method A and B with $d_{rep} = d_{mean}$, and method C and D with $d_{rep} = d_{50}$. The transport rates per fraction also give comparable results for all four methods (Table F.3). The most evident differences are given for the Factor 2 criterion, where method A using $k_s = d_j$ and $d_{rep} = d_{mean}$ gives the best results.

3.1.5 COMPARISON OF THE DIFFERENT MODEL SETTINGS

In this section the performances of all the different model settings are compared and the best model setting is determined. As the RMSE expresses the accuracy of the model as the error between the modelled and measured values, this criterion is chosen to be the most important when determining the best model setting. This is followed by the Factor 2 criterion.

Table 3.2 shows the performance of the calculated net total transport rates in comparison with the measured transport rates. Judging the model by its performance for the net total transport rates alone does not lead to a clear conclusion, as the settings have comparable values for both the RMSE and Factor 2, with slightly better values for the grain roughness setting. These small differences in performance may be due to the overall low transport rates computed by the Van Rijn model, where there are no large differences between the model settings. Furthermore, it is more valuable to judge the model on its performance per fraction, as the Van Rijn bed-load model is incapable of calculating transport in the negative direction, which might give misleading results for the performance of the net total transport rates.

Table 3.2: Performance of the Van Rijn model when modelling the net transport rates using different settings.

The average value of the observed transport is $0.32 * 10^{-4} \text{ m}^2/\text{s}$ and $N = 19$. The best setting is denoted in grey.

Name	Setting No. #	Bias [%]	r^2 [-]	RMSE [$*10^{-4} \text{ m}^2/\text{s}$]	Factor 2 [%]	Section
Graded approach	1.1	-28	0.59	0.18	74	3.1.2
	1.2	-14	0.44	0.17	79	
Uniform approach	2.1	-34	0.64	0.19	74	3.1.1
	2.2	-11	0.42	0.17	79	
Grain roughness	3.1	-1	0.44	0.16	89	3.1.3
	3.2	20	0.27	0.18	89	
Selective transport	4.1	-33	0.64	0.19	74	3.1.4
	4.2	-22	0.54	0.17	79	
	4.3	-23	0.54	0.17	79	
	4.4	-10	0.41	0.17	79	
	4.5	-23	0.54	0.18	79	
	4.6	-23	0.54	0.18	79	

According to table F.3, the Factor 2 criterion gives the best result for the graded approach using $d_{rep} = d_{mean}$ (setting 1.2). Regarding the RMSE for the fine fraction, the grain roughness approach (setting 2) gives the worst results. For the medium and coarse fraction the values of the RMSE are comparable for all settings, where setting 4.1 and 4.4 (method B) give higher RMSE values. Therefore, the graded approach using $d_{rep} = d_{mean}$ (setting 1.2) is selected as the best model setting.

3.2 SANTOSS MODEL

Within the SANTOSS model four main model settings can be distinguished, namely:

1. Model setting 1: Graded approach

The representative grain diameter of the entire mixture can either be based on d_{50} or d_{mean} (Section 2.5.1). Using a graded approach (Section 3.2.2), a distinction is been made between the grain sizes of the different fractions. The representative grain diameter which gives the best results is chosen, and used for setting 3 and 4.

2. Model setting 2: Uniform approach

The model does not recognise the different grain sizes in the different fractions and treats the mixture as if it is uniform, such that only one d_{50} or d_{mean} is used for the mixture (Section 3.2.1).

3. Model setting 3: Roughness approach

The approach for the wave-related roughness is modified (Section 3.2.3), using the best setting of model setting 1.

4. Model setting 4: Hiding and exposure

The correction factor for the effective grain-shear stress by Day (1980) is switched off (Section 3.2.4), using the best setting of model setting 1.

An overview of these four main settings is provided in Table 3.3, which clarifies which representative grain diameter (d_{rep}), diameter per fraction (d_j), and roughness approach for the wave-related roughness are used per model setting. Additionally, it shows whether the correction factor for the effective grain-shear stress λ_j is included and in which section the results of the setting are presented. Per main model setting different parameters are modified, leading to a total of ten different model settings. The performance of the model regarding the net transport rates per model setting is presented in Table 3.4, with the results per fraction in Table G.1.

Table 3.3: Different model settings to compute the net transport rates with the SANTOSS model. d_{rep} denotes the representative grain diameter of the entire mixture, d_j the grain size used per fraction, $k_{s,w}$ the approach used for the wave-related roughness (where only the part of the formula that is changed is given in this table, with the complete formula in Appendix B.1), λ_j the correction factor for the effective grain-shear stress, and *Section* in which section the results are presented and discussed. The best setting is denoted in grey.

Name	Setting No. #	d_{rep}	d_j	$k_{s,w}$	λ_j	Section																																			
Graded approach	1.1	d_{50}	d_j	$k_{s,w} = \max\{d_{rep}, \dots\}$	Included	3.2.2																																			
	1.2	d_{mean}	d_j				Uniform approach	2.1	d_{50}	-	$k_{s,w} = \max\{d_{rep}, \dots\}$	-	3.2.1	2.2	d_{mean}	-	Roughness approach	3.1	d_{50}	d_j	$k_{s,w} = \max\{d_j, \dots\}$	Included	3.2.3	3.2	d_{50}	d_j	$k_{s,w} = \max\{3d_{90}, \dots\}$	3.3	d_{mean}	d_j	$k_{s,w} = \max\{d_j, \dots\}$	3.4	d_{mean}	d_j	$k_{s,w} = \max\{3d_{90}, \dots\}$	Selective transport	4.1	d_{50}	d_j	$k_{s,w} = \max\{d_{rep}, \dots\}$	Excluded
Uniform approach	2.1	d_{50}	-	$k_{s,w} = \max\{d_{rep}, \dots\}$	-	3.2.1																																			
	2.2	d_{mean}	-				Roughness approach	3.1	d_{50}	d_j	$k_{s,w} = \max\{d_j, \dots\}$	Included	3.2.3	3.2	d_{50}	d_j		$k_{s,w} = \max\{3d_{90}, \dots\}$	3.3	d_{mean}	d_j			$k_{s,w} = \max\{d_j, \dots\}$	3.4	d_{mean}	d_j	$k_{s,w} = \max\{3d_{90}, \dots\}$	Selective transport	4.1	d_{50}	d_j	$k_{s,w} = \max\{d_{rep}, \dots\}$	Excluded	3.2.4	4.2	d_{mean}	d_j			
Roughness approach	3.1	d_{50}	d_j	$k_{s,w} = \max\{d_j, \dots\}$	Included	3.2.3																																			
	3.2	d_{50}	d_j	$k_{s,w} = \max\{3d_{90}, \dots\}$																																					
	3.3	d_{mean}	d_j	$k_{s,w} = \max\{d_j, \dots\}$																																					
	3.4	d_{mean}	d_j	$k_{s,w} = \max\{3d_{90}, \dots\}$																																					
Selective transport	4.1	d_{50}	d_j	$k_{s,w} = \max\{d_{rep}, \dots\}$	Excluded	3.2.4																																			
	4.2	d_{mean}	d_j																																						

3.2.1 GRADED VERSUS UNIFORM SAND APPROACH

To investigate to what extent graded effects play a role within the SANTOSS model in comparison with a uniform sand approach, the results of both these model settings are compared. For the uniform approach no distinction is made between the grain sizes of the fractions. An overall representative grain diameter of d_{50} is used, as was done by Van der A et al. (2013).

MODELLED TRANSPORT RATES

Comparison of the two sub-figures in Figure 3.10 shows that the graded sand approach gives better results than the uniform sand approach. Especially for the dataset by Hassan (2003) $d_{50} = 0.15mm$ and O'Donoghue and Wright (2004) $d_{50} = 0.15mm$ the model shows improvement. The main effect of the uniform approach is an overall increase of the calculated transport rates. Please note that the left sub-figure should show the same calculated transport rates as presented by Van der A et al. (2013) (Fig. 9), though this is not the case. No explanation has been found yet why these modelled transport rates show any differences, as it has been ought to use the same settings in this thesis project as were used by Van der A et al. (2013). The graded approach using $d_{rep} = d_{50}$ gives better results for the Bias, r^2 and RMSE (Table 3.4), where the Factor 2 criterion gives the same results for both approaches. Nevertheless, the computed transport rates obtained by the uniform sand approach (Fig. 3.10) still show acceptable results when compared to the data, where the majority of the calculated transport rates are within a Factor 2 interval.

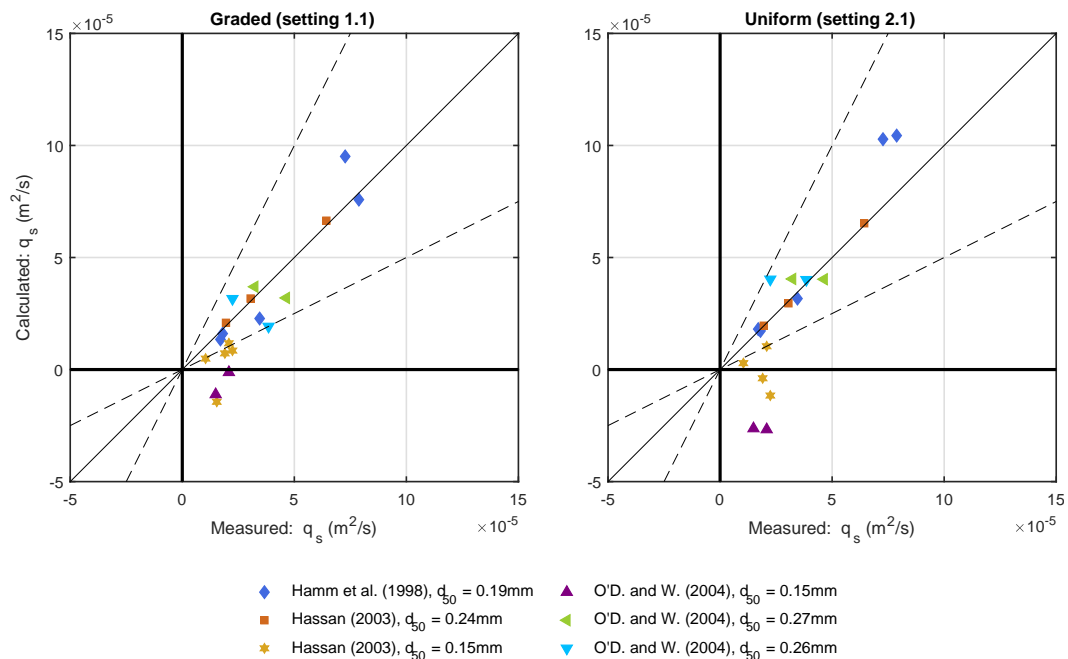


Figure 3.10: Net total transport rates for the graded (setting 1.1) and uniform (setting 2.1) approach using a representative grain diameter of d_{50} .

3.2.2 GRADED APPROACH USING A REPRESENTATIVE GRAIN DIAMETER OF d_{50} OR d_{mean}

In Section 2.5.1 a distinction has been made between d_{50} and d_{mean} . Where the SANTOSS model as reviewed by Van der A et al. (2013) only uses d_{50} as the representative grain diameter, now the results using both d_{50} and d_{mean} are compared, giving net total transport as presented in Figure 3.11.

When looking at the net total transport rates, the d_{mean} approach gives better results as the model computes all the total net transport rates in the correct direction and in 18 of the 19 cases the computed transport rates are in the Factor 2 interval (95%). Table 3.4 shows that the d_{mean} (d_m) approach gives better results for all criteria with exception of r^2 , which is slightly worse for $d_{rep} = d_{mean}$.

Figure 3.12 and Table G.1 show that the fine fraction gives better results regarding the Factor 2 interval using the d_{mean} approach as the scatter of this fraction has been reduced and 58% is located within this Factor 2 interval. Additionally, the RMSE and r^2 give better values for all fractions using the d_{mean} approach. Investigation of the transport per fraction per dataset shows that the calculated transport rates for Hassan (2003) $d_{mean} = 0.34mm$ and O'Donoghue and Wright (2004) $d_{mean} = 0.23mm$ are affected the most by the two approaches. Comparing the calculated sheet flow layer thickness for these datasets shows that the thickness for the d_{mean} approach is smaller than half the thickness of the d_{50} approach. Due to the reduced thickness for the d_{mean} approach, the phase lag parameter reduces as well, causing less fine sediment to stay in the water column until the subsequent crest or trough period. Figure 3.12 shows that this reduces the transport rates of the fine fraction into the negative direction. Concluding, the d_{mean} approach is a better representation of the representative grain diameter of the mixture, and will be used for further analysis in the next sections.

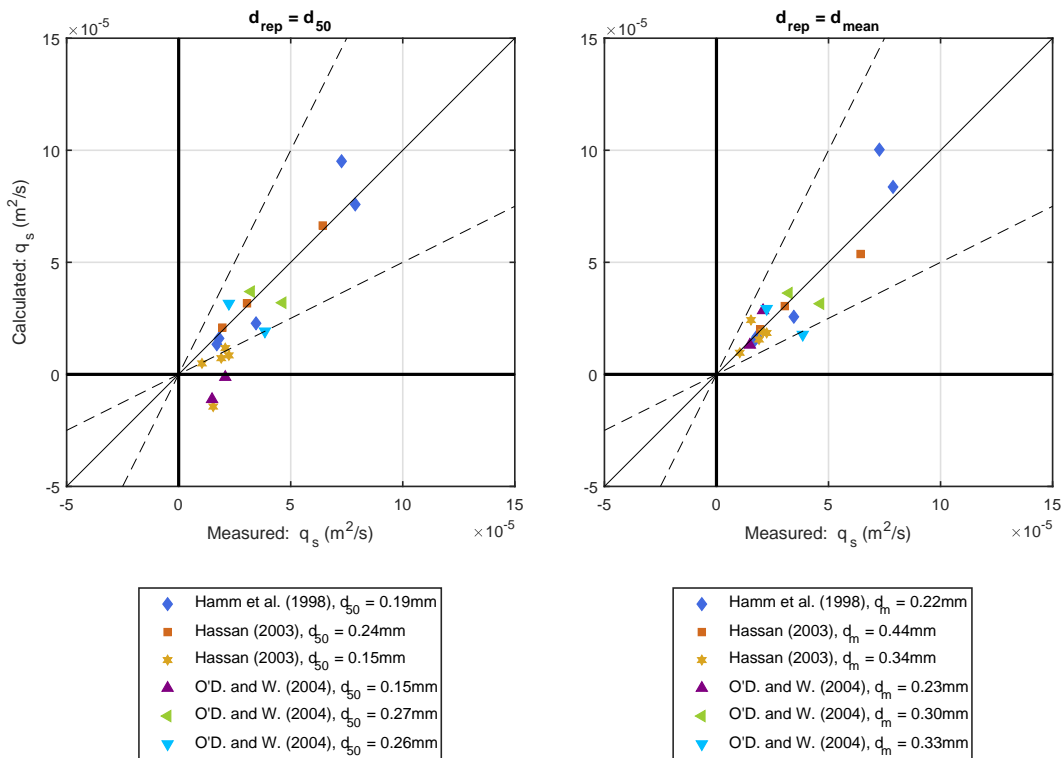


Figure 3.11: Net total transport rates for representative grain diameters of respectively d_{50} (setting 1.1) and d_{mean} (setting 1.2).

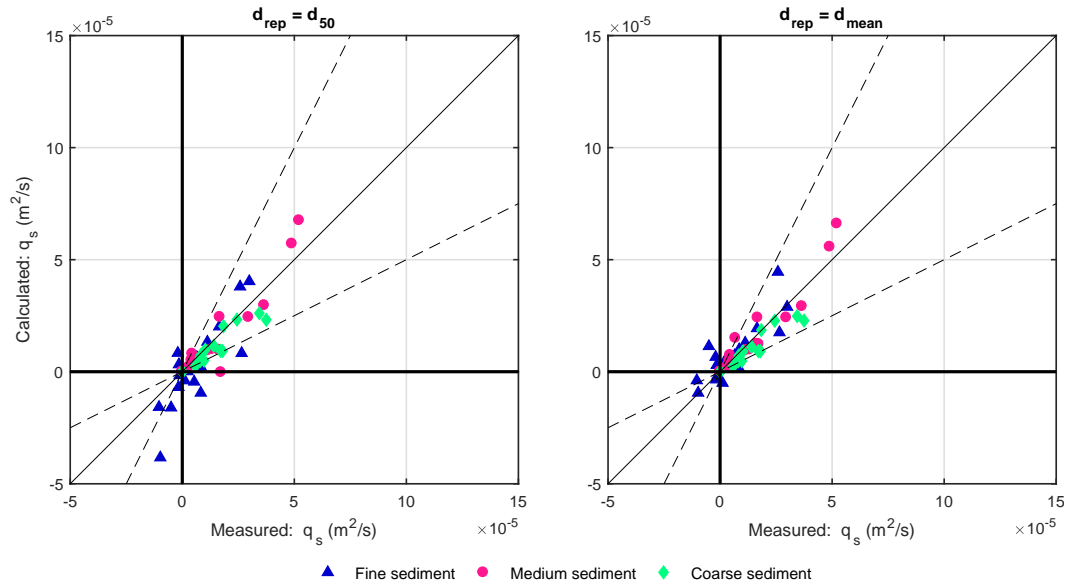


Figure 3.12: Net transport rates per fraction for different representative grain diameters of respectively d_{50} (setting 1.1) and d_{mean} (setting 1.2).

3.2.3 EFFECT OF ROUGHNESS SETTINGS

Due to the absence of a current, the current-related friction factor has a limited effect on the transport rates and the wave-related friction factor is the driving friction factor. To investigate the effects of the roughness approach on the transport rates, four additional settings are introduced besides the two default settings, in which the first term of Equation B.2, d_{50} , is varied as shown in Table 3.3. In Figure 3.13 the wave-related roughness as function of the grain size d_j is presented for all fractions of the 19 datasets. As shown, d_{50} , d_m and d_j give results in the same order of magnitude, reaching maximum values of around 1 mm, whereas $3d_{90}$ shows significantly higher values.

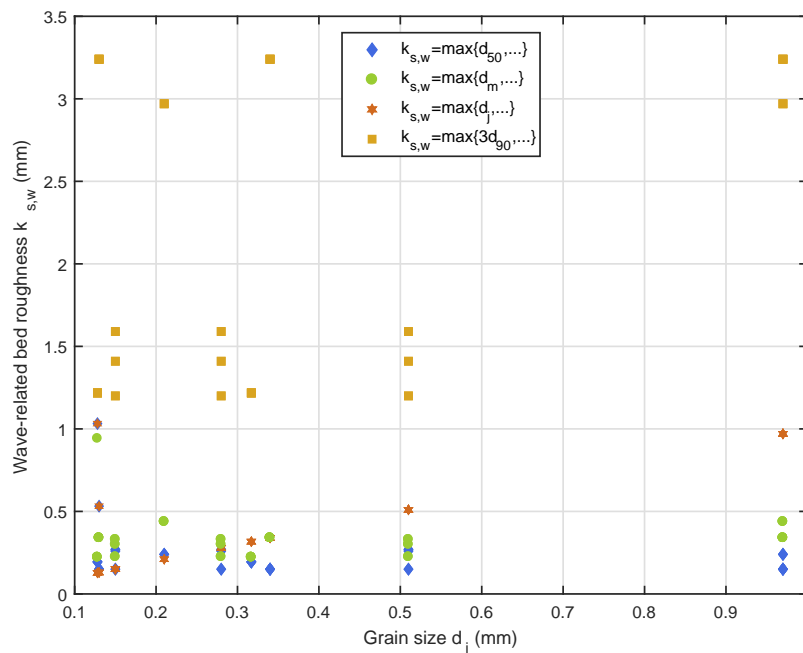


Figure 3.13: The wave-related roughness for four different settings as function of the grain size d_j

MODELLED TRANSPORT RATES

The total net transport rates and the transport rates per fraction for $d_{rep} = d_{mean}$ are presented in Figure 3.14 and 3.15. The total net transport rates and the transport rates per fraction using $d_{rep} = d_{mean}$ are presented in Figure 3.14 and 3.15. As the transport rates using the same formula for the current and wave-related friction factor ($k_{s,w} = 3d_{90}$, setting 3.2), became very high, this setting is not considered to be representative as a realistic model setting and the results are thus moved to Appendix F.

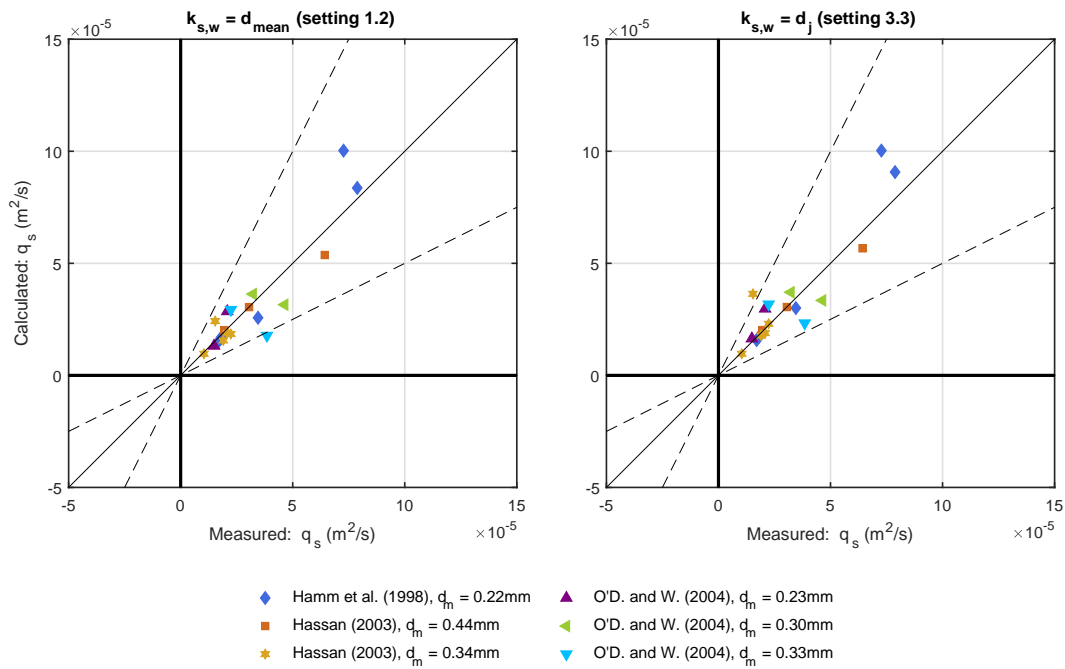


Figure 3.14: Net total transport rates for different settings for the wave-related roughness, using $d_{rep} = d_{mean}$

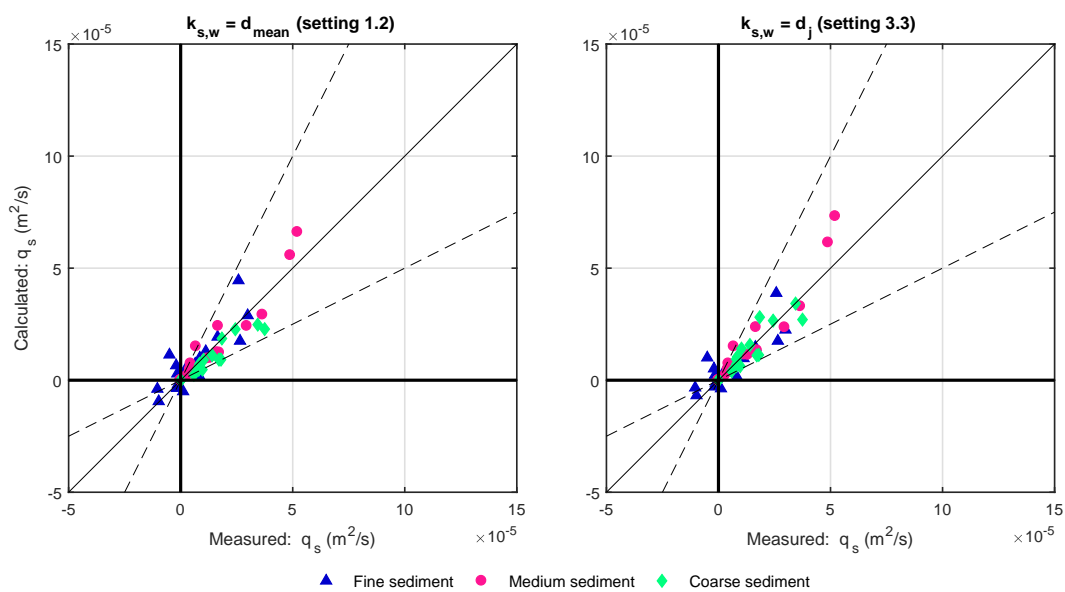


Figure 3.15: Net transport rates per fraction for different settings for the wave-related roughness, using $d_{rep} = d_{mean}$

The graded approach using $k_{s,w} = \max\{d_{mean}, \dots\}$ and $k_{s,w} = \max\{d_j, \dots\}$ give comparable results for the net total transport rates (Table 3.4) with almost the same accuracy, showing slightly higher transport rates for $k_{s,w} = d_j$ (Fig. 3.14). Figure 3.15 shows small differences between setting 1.2 and 3.3, where the transport rates of the medium and coarse sediment have increased, comparable to those in Figure G.2, and the transport rates of the fine sediment have decreased for a number of experiments. Analysis of the performance of the different fractions per setting (Table G.1) shows that $d_{rep} = d_{mean}$ with $k_{s,w} = d_j$ (setting 3.3) gives the best results regarding the RMSE, except for the medium fraction, and the Factor 2 criteria.

3.2.4 EFFECT OF SELECTIVE TRANSPORT

Selective transport has been embedded in the model as a correction factor (λ_j) for the effective grain-shear stress due to grading. This correction factor is multiplied with the Shields parameter to obtain the effective Shields parameter (Eq. 2.27). λ_j increases with an increasing relative grain size (Fig. 3.6a), and thus increases the effective Shields parameter for the coarser grains and decreases this parameter for the finer grains.

MODELLED TRANSPORT RATES

In Figure 3.16 and 3.17 the effect of λ_j on the transport rates is presented for a representative grain diameter of d_{mean} . The effects on the net total transport rates are minor, showing a small increase for the calculated net transport rates for the dataset by Hamm et al. (1998) ($d_m = 0.22mm$, experiment K1 and K6), Hassan (2003) ($d_m = 0.34mm$, experiment S9F) and O'Donoghue and Wright (2004) ($d_m = 0.33mm$, experiment X4A5010). Table 3.4 shows that including λ_j and using $d_{rep} = d_{mean}$ gives the best overall results. The percentage of the total net transport rates calculated within the Factor 2 interval is the same for both inclusion and exclusion of λ_j .

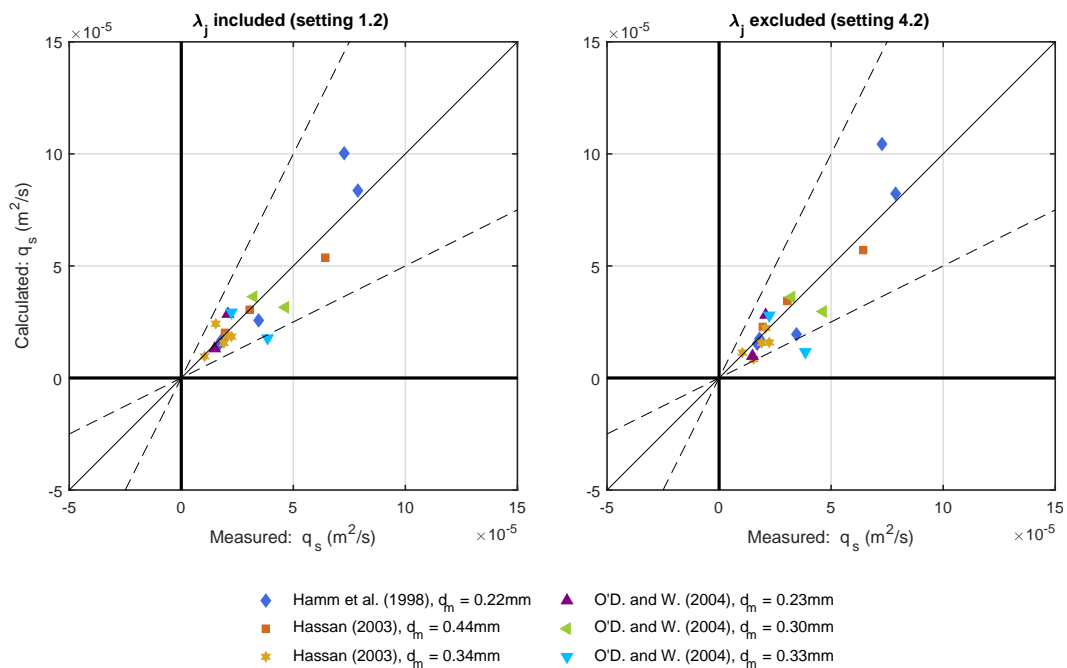


Figure 3.16: Net total transport rates for both exclusion and inclusion of the correction factor for the effective grain-shear stress using $d_{rel} = d_{mean}$.

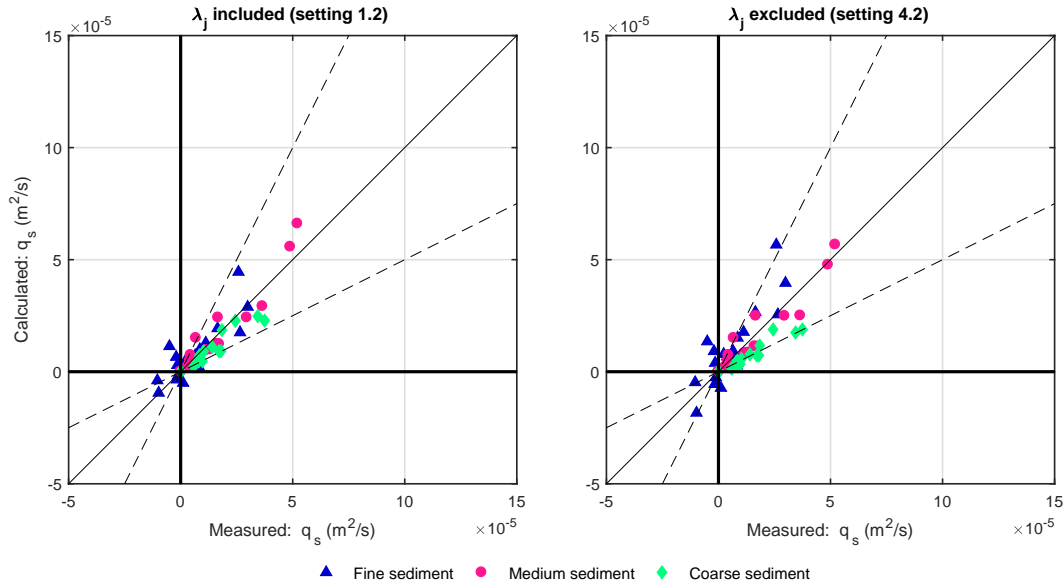


Figure 3.17: Net total transport rates for both exclusion and inclusion of the correction factor for the effective grain-shear stress using $d_{rel} = d_{mean}$.

Comparison of the transport rates per fraction in Figure 3.17 shows that the transport rates of the coarse and medium fractions are slightly higher when λ_j is included. The scatter in the computed transport rates of the fine fraction has been reduced, since $\lambda_j < 1$ when $d_j < d_{mean}$, which reduces the computed transport rates. Table G.1 shows that r^2 gives slightly worse values for the fine and coarse fraction when λ_j is included. The RMSE values however, are better for the fine and coarse fractions when incorporating λ_j , indicating that hiding and exposure processes take place within the flow tunnel experiments. Nevertheless, the RMSE gives better results for medium size grains when no hiding and exposure is incorporated in the model. This is due to two experiments by Hamm et al. (1998) (K5 and K6, Table 2.1), where the calculated transport rates already overestimate the measured transport rates when there is no hiding and exposure included in the model. Since $\lambda > 1$ for the medium fraction for both these experiments when hiding and exposure is incorporated, the calculated transport rates give an even larger overestimation of the measured transport rates for the graded approach (setting 1.2). In the entire database only these two experiments have both waves and currents, where the waves are of the sinusoidal type. The percentage of calculated transport rates per fraction within a Factor 2 interval is higher when hiding and exposure is included, mainly as an effect of the reduced scatter of the fine fraction (Fig. 3.16).

3.2.5 COMPARISON OF THE DIFFERENT MODEL SETTINGS

The results of the different model settings are evaluated for the net total transport rates and for the transport rates per fraction, where the RMSE and Factor 2 criteria are decisive when choosing the best model setting. Regarding the net total transport rates (Table 3.4), the uniform approach (setting 2) shows the least desirable results, followed by setting 4 where λ_j is excluded. The graded approach (setting 1) and the roughness approach with $k_{s,w} = d_j$ (setting 3.1 and 3.3) give the most favourable results, with the best results for $d_{rep} = d_{mean}$. Finally, assessment of the transport rates per fraction using $d_{rep} = d_{mean}$ gives the most favourable results for $k_{s,w} = d_j$ (setting 3.3). Yet, all the different settings with their corresponding tables and figures imply that the fine fraction is the hardest to model accurately and thus provides the model with the highest uncertainty regarding the accurate modelling of the net total transport rates.

Table 3.4: Performance of the SANTOSS model when modelling the net transport rates using different settings. The average value of the observed transport is $0.32 * 10^{-4} m^2/s$ and $N = 19$. The best setting is denoted in grey.

Name	Setting No. #	Bias [%]	r^2 [-]	RMSE [$*10^{-4} m^2/s$]	Factor 2 [%]	Section
Graded approach	1.1	-39	0.84	0.14	63	3.2.2
	1.2	-1	0.82	0.10	95	
Uniform approach	2.1	-64	0.74	0.27	63	3.2.1
	2.2	56	0.69	0.24	89	
Wave-related roughness	3.1	-11	0.87	0.12	84	3.2.3
	3.2	-29	0.66	0.37	58	
	3.3	9	0.82	0.10	95	
	3.4	47	0.73	0.25	84	
Selective transport	4.1	-60	0.76	0.19	53	3.2.4
	4.2	-7	0.79	0.12	95	

3.3 COMPARISON VAN RIJN AND SANTOSS

For the Van Rijn model, model setting 1.2 was selected as the best model setting, using method A, a grain roughness based on d_j and a representative grain diameter of d_{mean} . This is largely in accordance with the approach by Van Rijn (2007c), though he used a representative grain diameter of d_{50} . For the SANTOSS model, model setting 3.3 was selected as the best model setting. This setting used a wave-related roughness based on d_j and a representative grain diameter of d_{mean} . This is different than the approach by Van der A et al. (2013), where a wave-related roughness based on d_{rep} was used and a representative grain diameter of d_{50} . It is not known why Van der A et al. (2013) used a representative grain diameter of d_{50} instead of d_{mean} and a grain roughness of d_{rep} . As the best setting of both models uses a roughness approach based on d_j and a representative grain diameter of d_{mean} , these approaches seem to be crucial to model graded bed-load transport the most accurately. In Figure 3.18 and 3.19 the total net transport rates and the transport rates per fraction for the best model settings for both bed-load transport models are shown.

Overall, the calculated net transport rates are lower for the Van Rijn model than for the SANTOSS model. For the dataset by Hamm et al. (1998), with measured rates of 7.8 and $7.3 * 10^{-5} m^2/s$, the calculated transport rates by Van Rijn are less than half the magnitude of those computed by SANTOSS. This is partly due to the difference between the current and wave-related friction factor, which gives higher values for the SANTOSS model and results in higher transport rates. The current and wave-related friction factors used in the SANTOSS and Van Rijn model are calculated respectively by Equation 2.25 and 2.14. However, the equation used in the Van Rijn model has an additional β incorporated, which has a value smaller than 1, reducing the effect of the current-friction factor. Only the transport rates computed for the experiment by Hamm et al. (1998) are affected by this factor, as this is the only dataset with a current. According to Table 2.1 the type of wave used for these two specific experiments was sinusoidal, which probably causes the significant difference between these two models, as no other differences between this dataset and other datasets were found. According to Table 3.2 and 3.4 the SANTOSS model is a better fit to the given dataset as it scores better on all the assessment criteria. In Figure 3.19 the transport per fraction is shown.

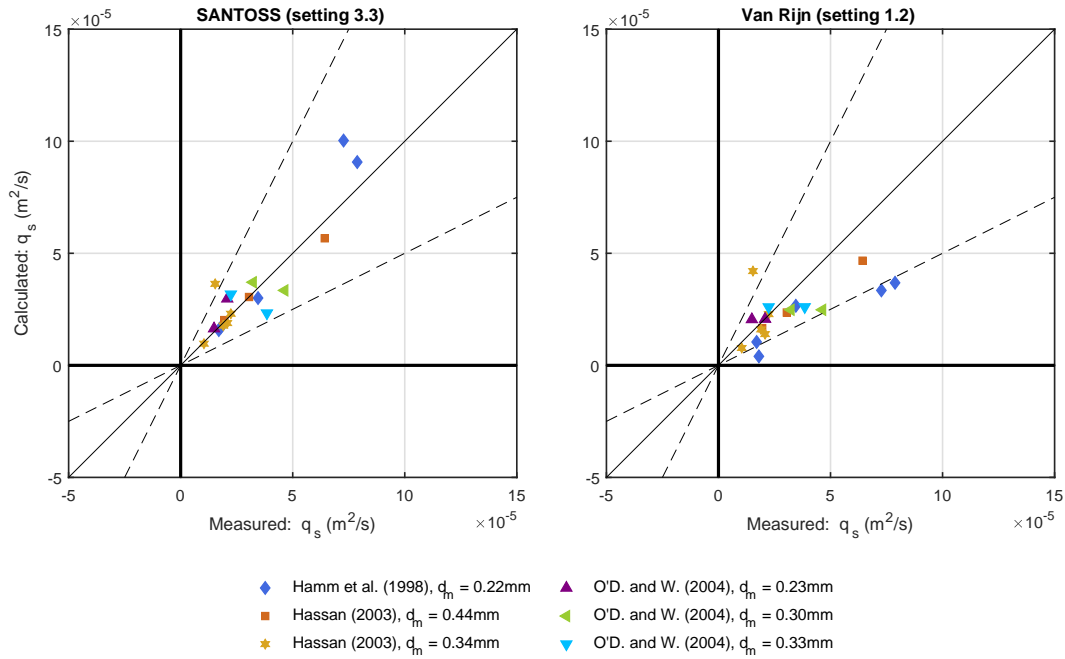


Figure 3.18: Net total transport rates for different settings for the grain roughness, using $d_{rep} = d_m$.

Regarding the transport per fraction, the Van Rijn model computes lower values for the coarse and medium fraction due to lower bed shear stresses, which are incapable of mobilising the sediment. The model is incapable of modelling transport of fine sediment in the negative direction. Whereas the SANTOSS model accounts for phase lag effects, this processes has not yet been incorporated in the Van Rijn bed-load transport formulations. In DELFT3D these phase lag effects have been accounted for with the formulation by Van Rijn for the wave-related suspended sediment transport.

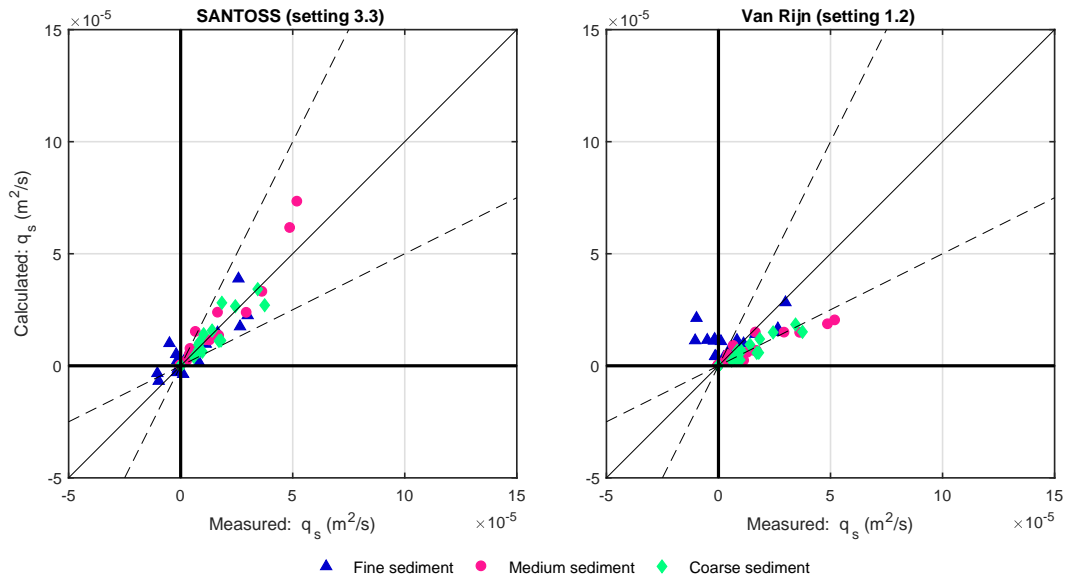


Figure 3.19: Net total transport rates for different settings for the grain roughness, using $d_{rep} = d_m$.

Table 3.2 and 3.4 generally show better results for the SANTOSS model. r^2 gives a significantly worse result for the fine fraction computed by Van Rijn as all transport has been modelled in the positive direction. Better results for the RMSE and Factor 2 interval are obtained by the SANTOSS model, whereas for the Factor 2 interval this is due to the overall lower transport rates for the medium and coarse fractions.

3.3.1 CONCLUSION

This chapter gives answer to research question 1: *How well do models for practical bed-load transport perform for sand mixtures compared to flow tunnel data and how can these models be improved?*

The best setting of the Van Rijn model computes transport rates with an RMSE of $0.17 * 10^{-4} m^2/s$ and 79% within a factor 2 of the data. The graded approach however, does not show large differences with the uniform approach, implicating that within the bed-load formulations the graded effects do not have a large influence on the transport rates. This model has been improved by using a weighted d_{mean} instead of a d_{50} derived from a sieve curve. Additionally, this model could be improved by investigating the effects of including streaming effects in the formulation.

The best results obtained by the SANTOSS model gives an RMSE of $0.10 * 10^{-4} m^2/s$ with 95% within a factor 2 of the data. This is clearly better than the Van Rijn model and larger differences are shown between the graded and uniform approach. This model has also been improved by using d_{mean} instead of d_{50} .

4

SET-UP AND CALIBRATION OF THE HYDRODYNAMICS OF THE DELFT3D MODEL

Before modelling the sediment transport, the hydrodynamics need to be calibrated. Previously, this was already done by Schnitzler (2015) and He (2017). Schnitzler (2015) added formulations to DELFT3D, which account for accurately modelling energy dissipation due to breaking of regular waves. However, after this modification some post processing of the data has taken place. In 2017, He (2017) applied modifications to the formulations which determine the turbulent kinetic energy and validated different formulations for the reference concentration. The work of Schnitzler (2015) was found to be more reliable due to the accurate description of all the modifications which were carried out during the calibration procedure, in contrast with He (2017). Therefore, this model is the starting point of the calibration which is to be carried out for this thesis project. This chapter will start with a description of the model set-up, followed by the calibration process. In the calibration process, first the wave height is calibrated as it is important to accurately model the breaking point. Hereafter, the undertow and turbulent kinetic energy are calibration, without changing the height.

4.1 MODEL SET-UP

In this section the model set-up as calibrated by Schnitzler (2015) is described, starting with a description of the grid, followed by the initial and boundary conditions and concluded with the roughness settings.

4.1.1 GRID SET-UP

The model has one grid cell in the alongshore direction, 263 cross-shore grid cells and 24 vertical layers. Due to the complexity of the physical processes and the measurements, the grid has a high resolution, with grid cells of 0.2m near the breaker-bar and 0.9m near the boundaries. The water depth on the left boundary is 2.55m and $\Delta t = 0.06s$. The resolution of the latter is needed due to drying and flooding conditions and corresponding Courant numbers near the shore (right boundary) (Schnitzler, 2015). The thickness of the layers is given as percentage of the water depth and is as follows: 1%, 1.3%, 1.6%, 2%, 2.4%, 3.1%, 3.8%, 4.8%, 5.8%, 7%, 8.2%, 9%, 9%, 8.2%, 7%, 5.8%, 4.8%, 3.8%, 3.1%, 2.4%, 2%, 1.6%, 1.3% and 1%. The grid is presented in Figure 4.1.

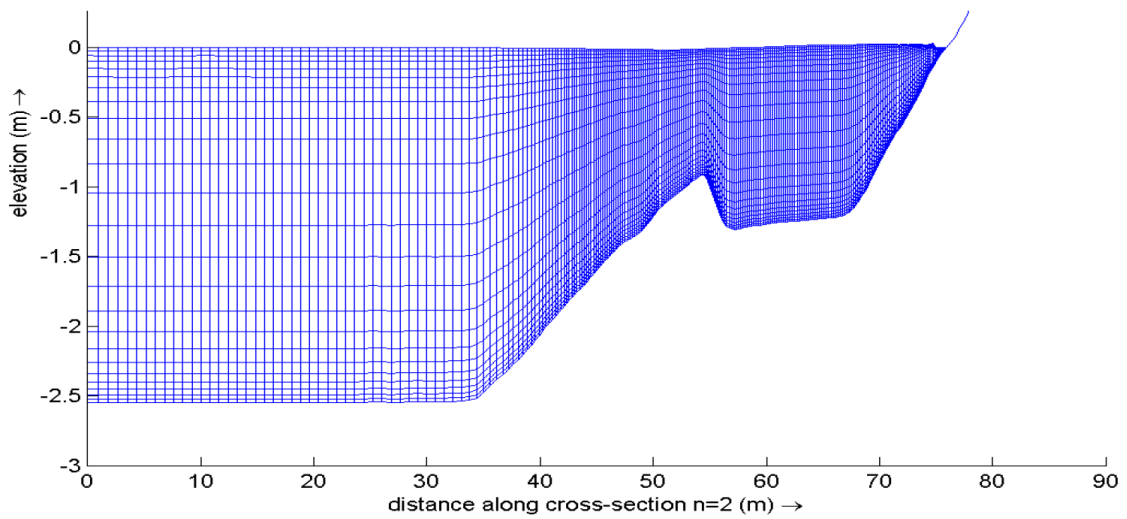


Figure 4.1: Grid dimensions as used for the SINBAD experiments (Schnitzler, 2015).

4.1.2 INITIAL AND BOUNDARY CONDITIONS

At the start of the model computations initial conditions are imposed on the model. The initial water level is set to 0m and as the water was at rest when the measurements were taken and sediment had time to settle, the sediment concentration in the water column is set to 0 kg/m^3 . On the left side of the model ($x=0\text{m}$) an open boundary is located where the waves are generated ($H = 0.80\text{m}$ and $T = 4\text{s}$). As the waves measured in the wave flume are not exactly equal to 0.85m, this value is set to 0.80m in the model.

4.1.3 ROUGHNESS SETTINGS

Before any computations can be carried out, the bed roughness needs to be established. The roughness regions along the bed profile together with the type of roughness and its value are displayed in Table 4.1.

Table 4.1: Different roughness regions along the bed profile.

	$x < 8\text{m}$	$x = 38 - 68\text{m}$	$x > 68\text{m}$
Type of bottom	Smooth concrete	Sand	Sand covered with plastic, iron and concrete tiles
Type of roughness	Chezy	Bed-forms	Chezy
Value	$85\text{m}^{1/2}/\text{s}$	Roughness approach by (Van Rijn, 2007a) for bed-forms (Appendix A.2)	$45\text{m}^{1/2}/\text{s}$

4.2 RESULTS OF THE CALIBRATION OF THE HYDRODYNAMICS

The hydrodynamics are calibrated by comparing the modelled wave height and undertow to the measurements. The parameters which are used for calibration are the same parameters which were used by Schnitzler (2015) and He (2017). The optimal parameter settings found by Schnitzler (2015), He (2017) and after the calibration described in this chapter are presented in Table 4.2. For this thesis project, first the wave height is calibrated because it is important that the breaking point is modelled accurately, as energy dissipation occurs when the waves break, causing driving forces for sediment transport. Calibration of the wave height has taken place by varying the values for α_{rol} , F_lam, Gamdis and Reldep. By varying α_{rol} , the slope of the breaking wave is steepened or flattened. F_lam and Gamdis mainly determine the location where the wave breaks, and by varying Reldep the water depth after wave breaking is determined. After calibration of the wave height the undertow is calibrated by varying the value for Betaro. In the following paragraphs the wave height and undertow are presented for the parameter settings shown in Table 4.2.

Table 4.2: Optimal parameter settings after calibration of the hydrodynamics in DELFT3D.

Parameter	Symbol	Value	Value Schnitzler (2015)	Value He (2017)	Description
Alfaro	α_{rol}	10	6	6	Roller dissipation coefficient. Used in the formula for energy dissipation due to breaking waves (Eq. 2.32)
Betaro	β_{rol}	0.25	0.25	0.20	Roller slope parameter which is used in the formula for the roller energy dissipation (Eq. 2.36) and determines the wave energy transferred from the roller model to the underlying water. Especially useful when calibrating the undertow.
F_lam		2	2	0	Breaker delay parameter. Spatial lag between break point and actual breaking.
Fwee	f_w	0	0	0	Bottom friction factor. This parameter is excluded from the model, as it reduces the peak wave height.
Gamdis	γ	0.8	0.62	0.58	Wave breaking index. Determines when a wave breaks, where a higher value allows the waves to get higher and break later (Eq. 2.33).
Reldep		0.35	0.35	0.35	Value to which waves keep breaking. This parameter accounts for regular waves in DELFT3D which break at the same location in contradiction with irregular waves (Eq. 2.33).

4.2.1 WAVE HEIGHT

During the experiments wave height data was obtained using Resistive Wave Gauges (RWGs), Pressure Transducers (PTs) fixed to the wall, and PTs on a mobile frame. The RWGs measured the actual wave height, whereas the PTs used a pressure signal and a correction based on the linear wave theory to derive the wave height (Van der Zanden, 2016). As shown in Table 4.2, only the PTs provide information about the wave height in the shoaling and breaking region ($x=50$ till 85.5m). Within this region the undertow is the largest compared to other locations along the wave flume (Section 4.2.2). Additionally, the wave height is used in formulae which model the energy dissipation. As this drives the sediment transport, particularly the shoaling and breaking region are of interest and it is important that the wave height can therefore be modelled accordingly. Due to the absence of measurements taken by the RWGs within this region, the model is calibrated for the data obtained by the PTs, even though the latter is considered to be less reliable since the wave heights are derived using the linear wave theory, instead of retrieving the wave heights directly. The calibrated wave height and measured wave height per instrument are shown in Figure 4.2.

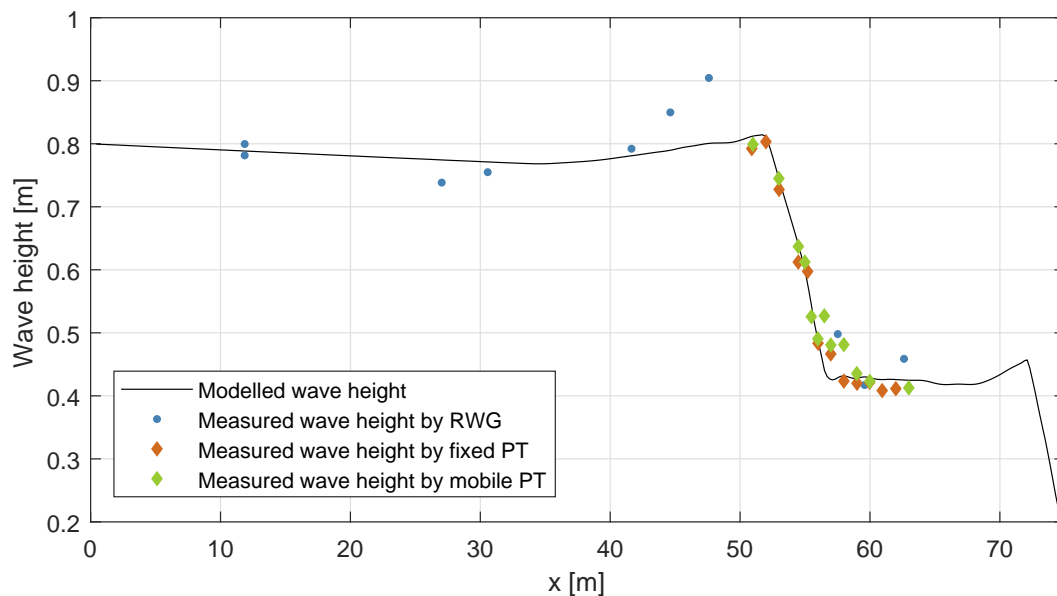


Figure 4.2: Calibrated wave height (black solid line) using measured wave heights by Resistive Wave Gauges (blue dots), fixed Pressure Transducers at the wall (red diamonds) and mobile Pressure Transducers (green diamonds).

As shown in Figure 4.2, the waves break between $x \approx 50$ and 60m. By deriving dH/dx for this region, the change in wave height of the model and measurements can be compared. This is only done with the PT data and the results are shown in Figure 4.3. As the data were obtained at different x locations along the wave flume than the x locations at which model output was given, the values for the data were interpolated to match the x locations of the model. Figure 4.3 shows that between $x=55$ and 56m the modelled wave height does not decrease as much as observed during the experiments. However, before $x=55$ m and after $x=56$ m the modelled decrease in wave height is larger than observed. Due to the scatter of the data, it is difficult to model the decrease in wave height accurately.

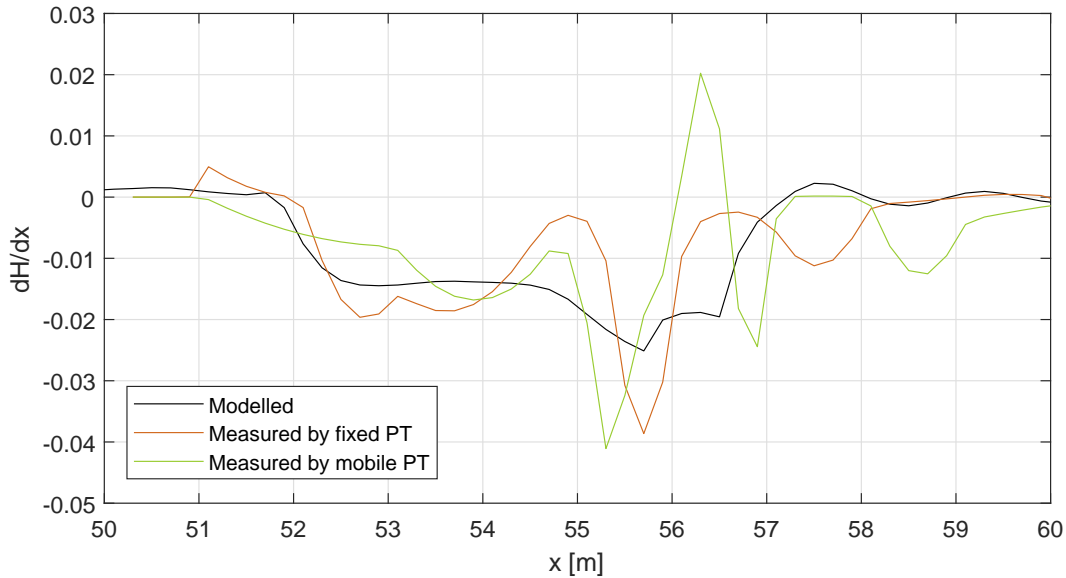


Figure 4.3: Gradient of the modelled (black line) and measured (red and green line) wave height along the wave flume.

The accuracy of the model between $x=50$ and 60m for the modelled wave height in comparison with the observed wave height using Pressure Transducers is given in Table 4.3. Comparison with the data obtained by the mobile Pressure Transducer gives a higher value for the RMSE than for the fixed PT. The mobile PT gives higher values for the wave height around $x\approx 57\text{m}$, where the wave height even slightly increased (Fig: 4.3), than the fixed PT and the model (Fig. 4.2), resulting in a larger RMSE.

Table 4.3: Performance of DELFT3D for the measured wave height.

	RMSE [m]	Bias [%]
Wave height (fixed PT)	0.018	1
Wave height (mobile PT)	0.027	-1

4.2.2 UNDERTOW

The undertow is equal to the average velocity and is calibrated using measured flow velocities obtained by Acoustic Doppler Velocimeters (ADV). Near the water surface the undertow is positive, but in order to account for this onshore flux, the flow direction closer to the bed is offshore. In Figure 4.4 the vertical undertow profile is presented for 12 locations along the wave flume. It is shown that after the waves break ($x>53\text{m}$) the undertow becomes stronger and the model is unable to replicate the data (between $x=55$ and 57m).

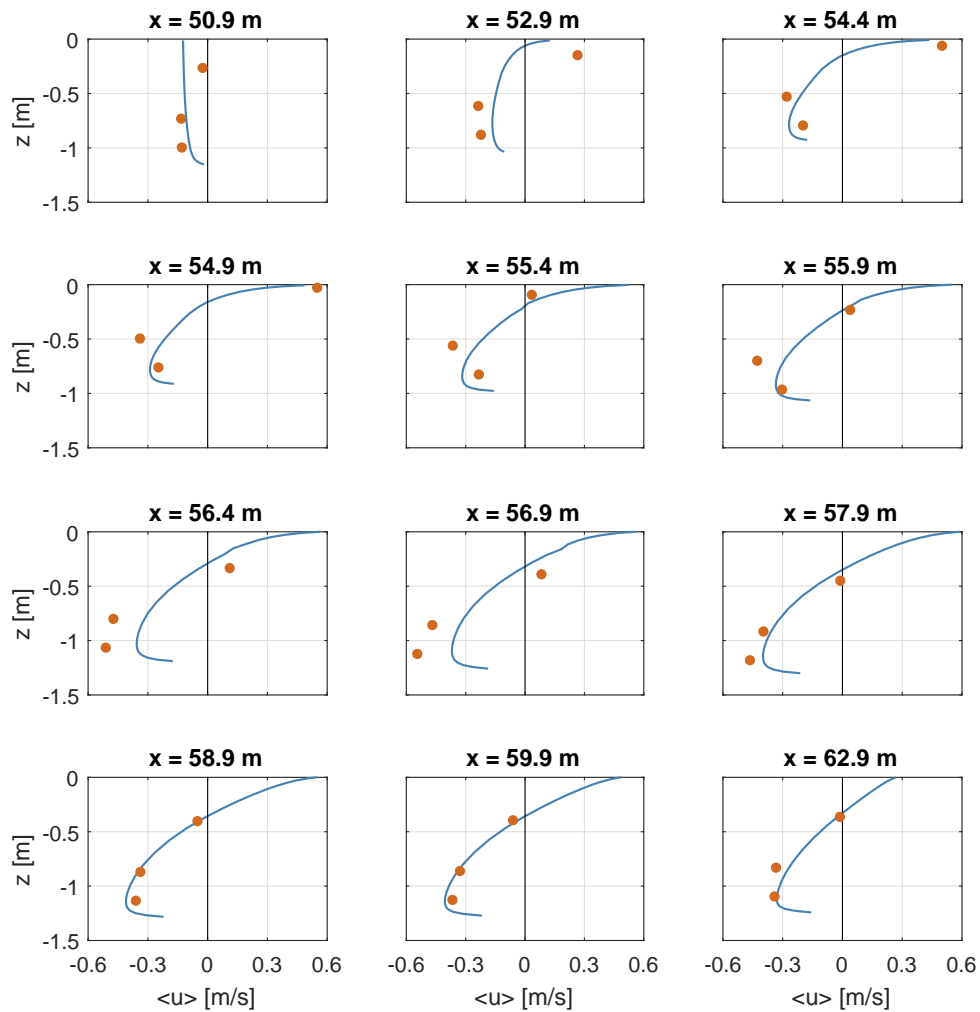


Figure 4.4: Calibrated undertow (blue line) using measured time-averaged velocities by Acoustic Doppler Velocimeters (red dots).

The undertow near the bottom along the wave flume is shown in Figure 4.5. The modelled undertow has been interpolated to match the water depth at which the measurements were taken. This depth (z) is denoted by the black line. Whereas the undertow is overestimated on top of the breaker bar ($x \approx 55\text{m}$), it is underestimated right behind the bar after the plunge point ($x \approx 56\text{m}$, Fig. 2.11). The gradient of the modelled and measured undertow is presented in Figure 4.6. Between $x \approx 56$ and 57m the gradient of the undertow is significantly underestimated by the model, where the modelled undertow underestimates the measured undertow (Fig. 4.5). Before $x \approx 56$ and 57m the model overestimates the measured undertow, where for $x < 56\text{m}$ the gradient is too strong and predicts a stronger undertow. When $x > 57\text{m}$ the magnitude of the modelled undertow still increases, though the measurements show that the undertow is actually decreasing. According to Equation 2.37, a lower gradient of the undertow results in lower suspended sediment transport rates, and lower suspended sediment concentrations higher in the water column. Especially behind the breaker bar this difference in gradient between the modelled and measured undertow may affect the accuracy of the modelled suspended sediment transport rates. The performance of DELFT3D regarding the measured undertow near the bottom is shown in Table 4.4.

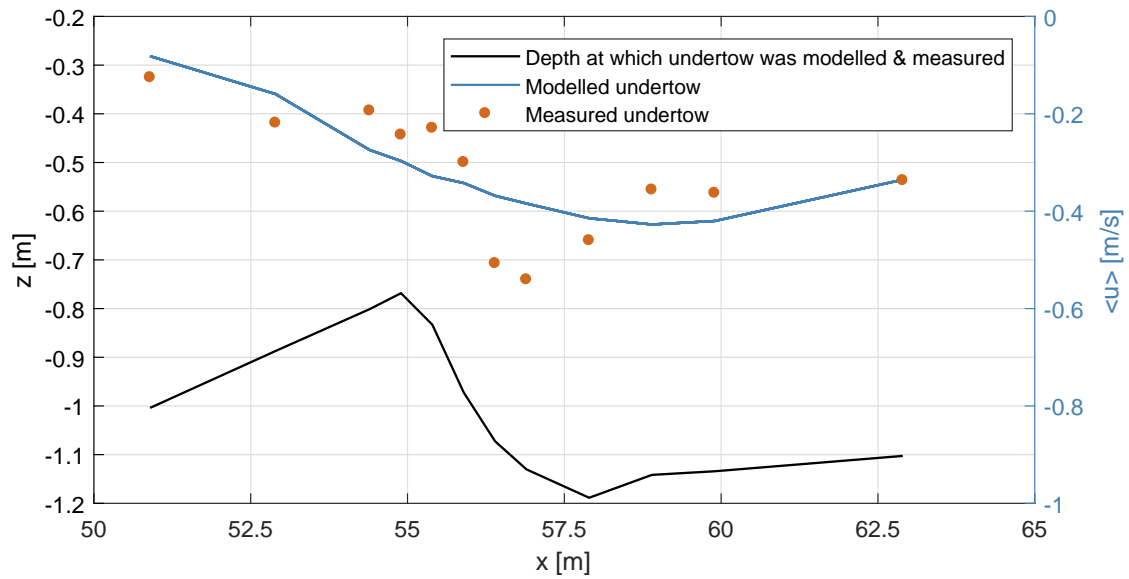


Figure 4.5: Calibrated undertow near the bottom (blue line) using measured time-averaged velocities obtained by Acoustic Doppler Velocimeters (red dots). The black line denotes at which depth the undertow was modelled and measured.

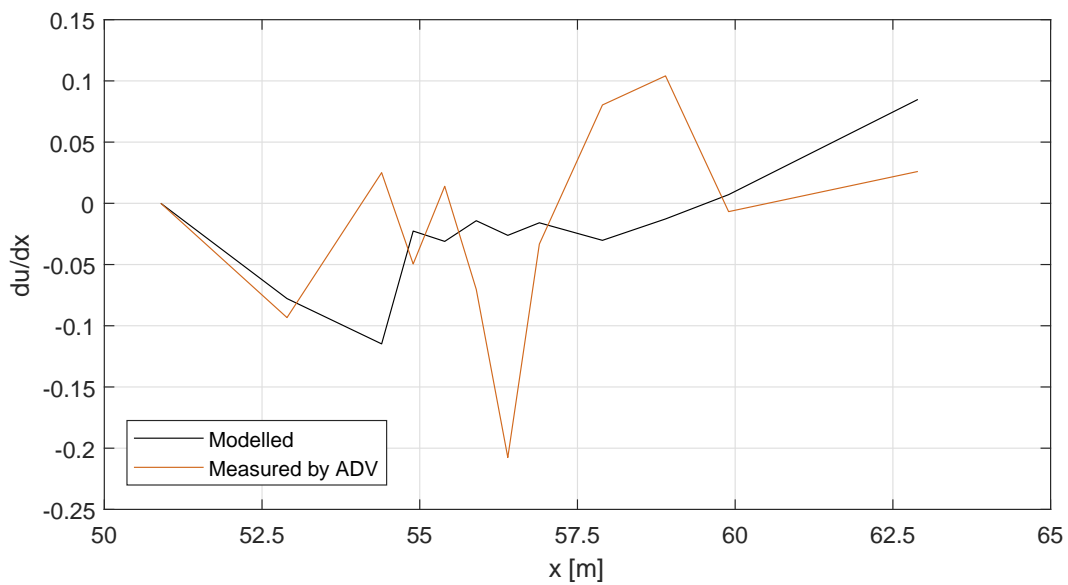


Figure 4.6: Gradient of the modelled (black line) and measured (red line) undertow along the wave flume.

Table 4.4: Performance of DELFT3D for the measured undertow near the bed.

	RMSE [m/s]	Bias [%]
Undertow (ADV)	0.08	2

ORBITAL VELOCITIES

The peak orbital velocities are shown in Figure 4.7, and represent the maximum onshore and offshore velocities (maximum and minimum orbital velocity). Before $x=55\text{m}$, the maximum orbital velocity is underestimated, but after $x=55.5\text{m}$ (plunge point) the measured velocities are overestimated. This is the location where the waves are breaking and where the largest decrease in maximum orbital velocity is shown. The modelled minimum orbital velocity is always underestimated. Overestimation of the onshore velocities and underestimation of the offshore velocities, may result in sediment transport that is overestimated in the onshore direction and underestimated in the offshore direction.

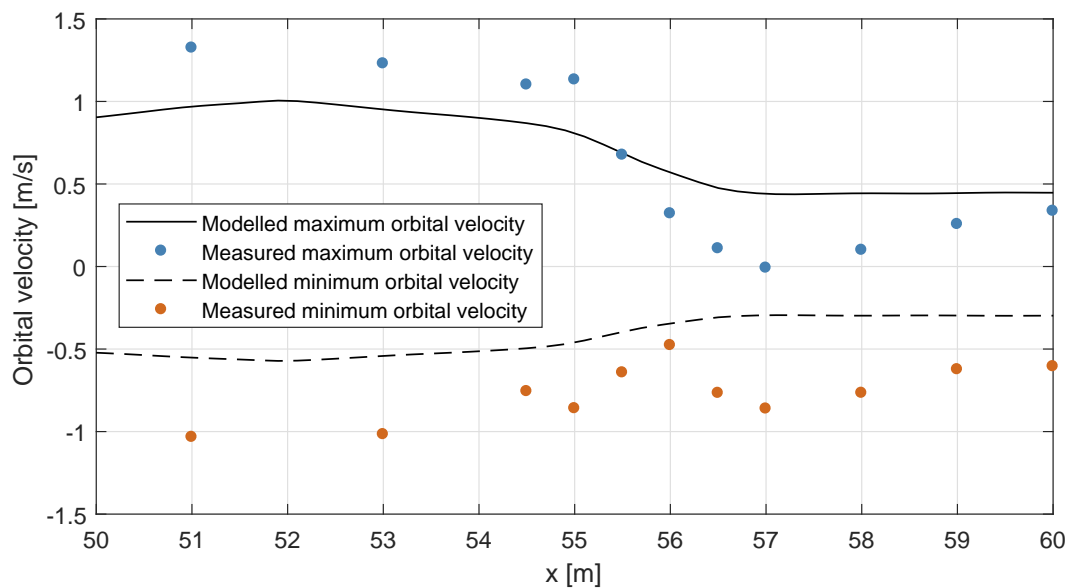


Figure 4.7: Measured and modelled maximum and minimum orbital velocities near the bottom ($\zeta \approx 0.02\text{m}$).

4.2.3 TURBULENT KINETIC ENERGY

The Turbulent Kinetic Energy (TKE) along the wave flume near the bed is presented in Figure 4.8. The data (red dots) were obtained by ADVs. The figure shows that the modelled TKE reaches its maximum before the top of the breaker bank is reached, whereas for the measurements this occurs right behind the breaker bank. Even though the orbital velocities decrease behind the breaker bar, the largest value for the TKE are measured within this region. This is due to the turbulence which is caused by breaking waves (Van der Zanden et al., 2017). Additionally, the peak is lower than the measurements. Table 4.5 shows that the model has the tendency to overestimate that data. Figure 4.9 shows the vertical TKE profile at 12 locations. In front of the plunge point ($x \approx 55.5\text{m}$), the TKE is substantially overestimated by the model. After this point the model approaches the measurements better.

Table 4.5: Performance of DELFT3D for the measured turbulent kinetic energy (TKE) near the bed.

	RMSE [m^2/s^2]	Bias [%]
Turbulent Kinetic Energy (ADV)	0.0086	31

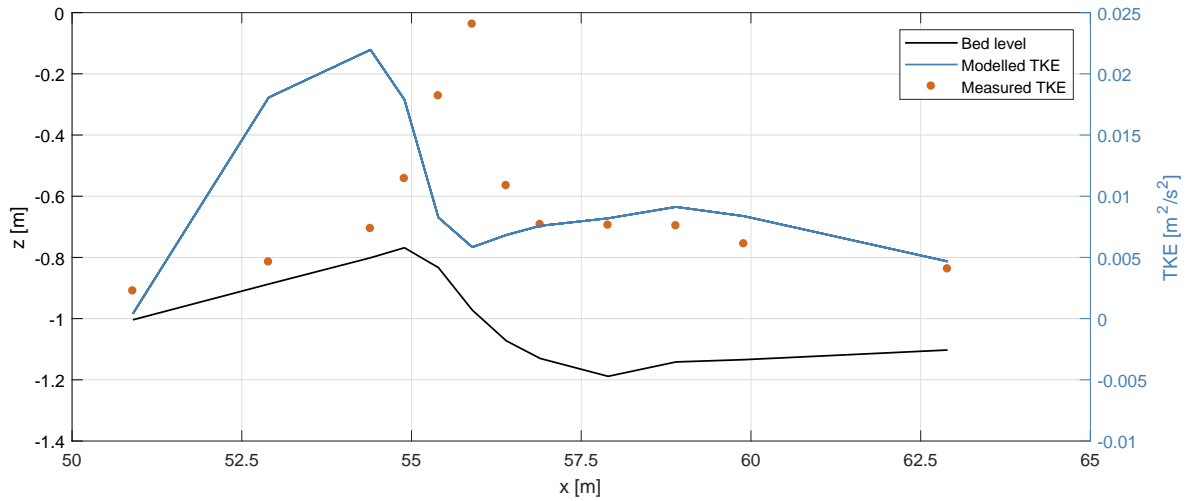


Figure 4.8: Calibrated Turbulent Kinetic Energy near the bottom (blue line) using measured time-averaged turbulence data obtained by Acoustic Doppler Velocimeters (red dots). The black line denotes at which depth the TKE was modelled and measured.

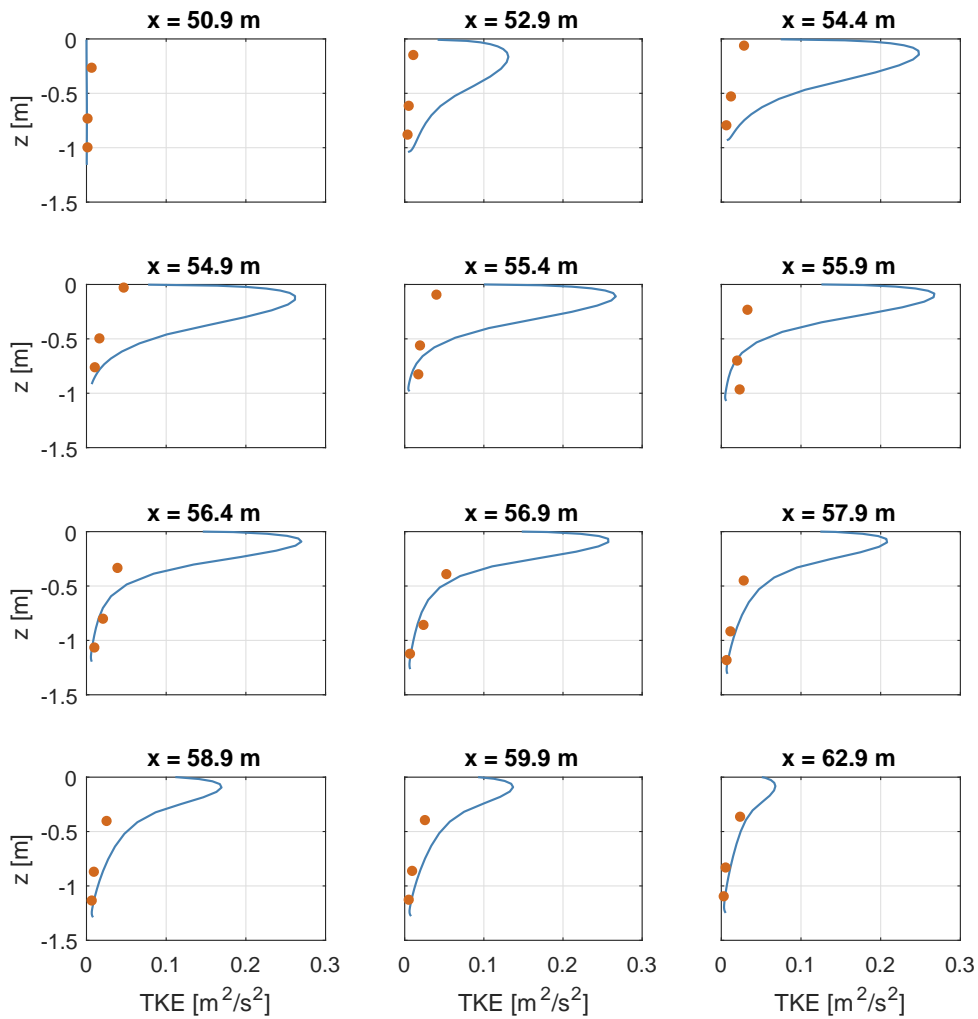


Figure 4.9: Calibrated Turbulent Kinetic Energy (blue line) using measured time-averaged turbulence data by Acoustic Doppler Velocimeters (red dots).

4.2.4 CONCLUSION

The calibrated wave heights approaches the measured wave heights by the Pressure Transducers neatly. Keeping in mind that there might be an error in these measurements as they have been derived indirectly by using the linear wave theory, the model approaches the wave height in the shoaling and breaking region pretty well.

The undertow near the bottom was mainly overestimated in front of the breaker bar, whereas it was underestimated right behind the breaker bar. This was also seen in the vertical undertow profile, where right after the plunge point the model was unable to approach the larger values for the undertow. Calibration of the TKE showed that peak values were obtained right before the top of the breaker bar, whereas the data showed a peak right behind the breaker bar.

Overall, the wave height and undertow were modelled quite accurately by DELFT3D. With a Bias between -1 and 2%, the model does not have the tendency to systematically over- or under-predict the data. With wave heights varying between 0.8 and 0.4m during wave breaking, and values for the RMSE of 0.018 and 0.027m depending on the device which is used, the model is able to accurately model the wave height in the breaker zone. The RMSE of the modelled undertow near the bed is relatively higher than for the wave height, with a value of 0.082 m/s and a modelled undertow varying between -0.15 and -0.45m/s. The modelled gradient of the undertow near the bed was less steep than the data, and behind the breaker bar the undertow was underestimated. This has effect on the suspended sediment transport and vertical concentration profile, which is further elaborated on in the next chapter.

5

ASSESSMENT OF MODELLED TRANSPORT RATES IN DELFT3D

This chapter aims to answer **research question 2** and starts with a description of the settings and validation process. At the start of the validation process, first a number of fractions is chosen. This is done using the sieve curve of the SINBAD experiments (Fig. 2.11), which is divided into a number of fractions (Section 5.1). Hereafter, in Section 5.2, the suspended sediment transport is investigated in terms of the suspended sediment concentrations, grain size distribution in the water column, and cross-shore suspended sediment transport rates. In Section 5.3 the cross-shore bed-load transport is examined, and in Section 5.4 the total transport rates in the cross-shore direction are assessed.

SETTINGS

The bed-load transport model used within DELFT3D is the model by Van Rijn. Data was collected every 15 minutes, therefore the simulated time of the DELFT3D model is 15 minutes. An extra 15 minutes is added as spin-up time, leading to a total simulated time of 30 minutes. Morphological updating has been switched off, and the bed composition is fixed during the run. A sensitivity analysis has been carried out to find the optimised parameter settings, which are shown in Table 5.1. The results of the sensitivity analysis are shown in Appendix H, with in Table H.1 the performance per setting.

Table 5.1: Default and optimised transport parameter settings.

Parameter	Default	Optimised	Description
FwFac	0	2	Tuning parameter for wave streaming
Sus	1	1	Current-related suspended sediment transport factor
Bed	1	1	Current-related bedload transport factor
SusW	1	1	Wave-related suspended sediment transport factor
BedW	1	1	Wave-related bedload transport factor
Dicouv	0.1	0.1	Uniform horizontal eddy diffusivity
AlfaBn	1	1	Transverse bed gradient factor for bedload transport
AlfaBs	1.5	1.5	Longitudinal bed gradient factor for bedload transport

The performance of the model for both the default and optimised setting is shown in Table 5.2. The choice of fraction setting is explained in Section 5.1. The uniform setting uses the parameter values which have been optimised for the graded setting.

Table 5.2: Performance of the model for the default and optimised transport parameter settings. The uniform approach uses the same parameter values as the optimised graded approach.

		Graded		Uniform	
		Default	Optimised	Default	Optimised
RMSE [$\cdot 10^{-5} \text{m}^2/\text{s}$]	q_{sc}	2.31	2.53	2.35	2.66
	q_{sw}	0.22	0.19	0.72	0.57
	q_b	4.80	4.07	4.77	4.09
	q_{tot}	3.55	1.7	2.61	1.35
Bias [%]	q_{sc}	162	-222	67	-209
	q_{sw}	44	3	420	268
	q_b	-69	-63	-68	-62
	q_{tot}	-157	-72	-141	-83

5.1 FRACTION CONFIGURATIONS

The sieve curve has been divided into 6 of segments, each equal to one fraction. Due to an unknown bug in the version of DELFT3D which was modified by Schnitzler (2015), incorporating formulae for regular breaking waves, it is not possible to use more than 6 fractions. By prescribing a maximum (SedMaxDia), minimum (SedMinDia) and median (SedDia) diameter per fraction, the model interpolates a piecewise log-uniform distribution between these values, avoiding any overlap between the different fractions. From this distribution the d_{10} and d_{90} are determined, which can be used for further analysis. In Table 5.3 three settings are displayed which all divide the sieve curve in segments differently.

Table 5.3: Three settings which all divide the sieve curve in segments differently. Per setting the percentage of the fractions available in the mixture is presented in the left column, and the median grain diameter of this fraction in the right column. The RMSE and Bias of the modelled transport rates are presented in the bottom, with the measured transport rates varying between $-6 \cdot 10^{-5} \text{m}^2/\text{s}$ and $6 \cdot 10^{-5} \text{m}^2/\text{s}$.

	Setting 1		Setting 2		Setting 3	
Fraction	p_j [%]	d_j [mm]	p_j [%]	d_j [mm]	p_j [%]	d_j [mm]
1	16.67	0.15	5	0.14	5	0.14
2	16.67	0.21	5	0.15	5	0.15
3	16.67	0.27	20	0.19	20	0.19
4	16.67	0.31	20	0.26	20	0.26
5	16.67	0.33	25	0.32	36.55	0.32
6	16.67	0.38	25	0.36	13.45	0.40
RMSE [$\cdot 10^{-5} \text{m}^2/\text{s}$]	3.63		3.65		3.55	
Bias [%]	-177		-161		-157	

Setting 1 divides the sieve curve equally regarding the cumulative grain size. Setting 2 and 3 place a greater emphasis on the fine tail as this part is assumed to be the most mobile, such that a larger resolution is required. Additionally, setting 3 uses a suitable distribution for the coarser fractions, where the shape of the sieve curve is taken into account (Fig. 5.1). The default transport parameter settings have been used for the comparison and assessment of the different fraction configurations. Since setting 3 gives the lowest value for the RMSE and Bias, this setting is chosen as the default

setting for the rest of the analysis carried out in this chapter. The d_m of the uniform approach is derived from the sieve curve (Fig. 5.1) and is 0.29mm.

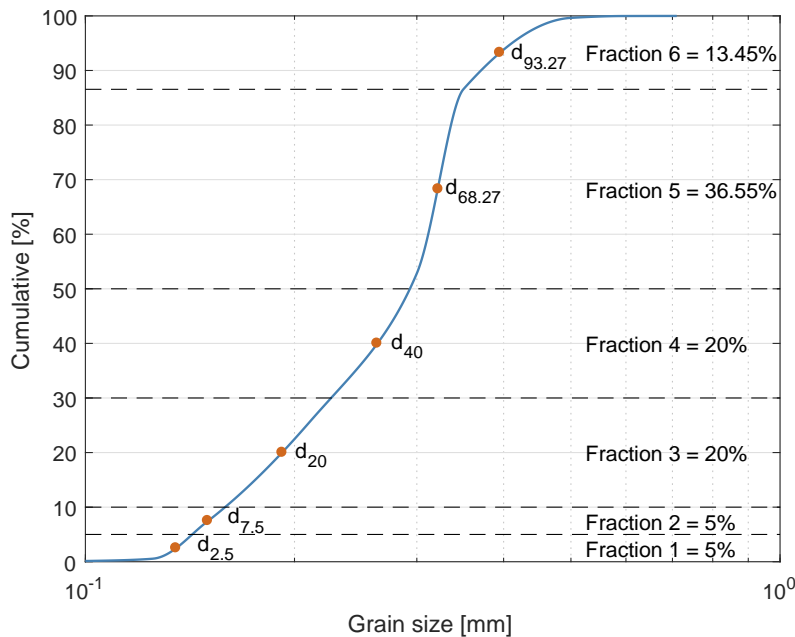


Figure 5.1: Cumulative grain size distribution (blue line) as used in the SINBAD experiments divided in 6 fractions (black dashed line). The median diameter of each fraction is denoted with a red dot.

5.2 SUSPENDED SEDIMENT TRANSPORT

The suspended sediment transport is analysed by investigating the suspended sediment concentrations, the vertical grain size distributions and the net cross-shore suspended sediment transport rates.

5.2.1 SUSPENDED SEDIMENT CONCENTRATIONS

To calculate the vertical suspended sediment concentration profile, first the reference concentration is computed, where after the suspended sediment concentration profile is calculated by assuming a Rouse profile (Van Rijn, 2007c).

REFERENCE CONCENTRATION

The reference concentration at the reference height is shown in Figure 5.2, with in Figure 5.3 the contribution per fraction. One reference height is determined for the entire mixture as the current-related roughness due to ripples, on which the reference height depends, is equal for every fraction in the same mixture. The reference concentration however, is calculated per fraction using d_j instead of d_{rep} , resulting in higher values for the graded approach. Concentrations increase for decreasing grain sizes (Fig. 5.3) (Van Rijn, 2007c). The finer fractions in the mixture lead to higher concentrations for the graded approach. Both approaches overestimate the reference concentration before $x = 55$ and after 56.5 m, and underestimate the concentration between these $x = 55$ and 56.5 m. This corresponds with the model results of the turbulent kinetic energy, which show the same behaviour (Fig. 4.8). Approximately 37% of the entire mixture consists of fraction 5, which is also shown to have the largest contribution to the reference concentration (Fig. 5.3). The lower panel in Figure 5.3 shows that the smaller the grain size, the larger the unweighted contribution to the reference concentration.

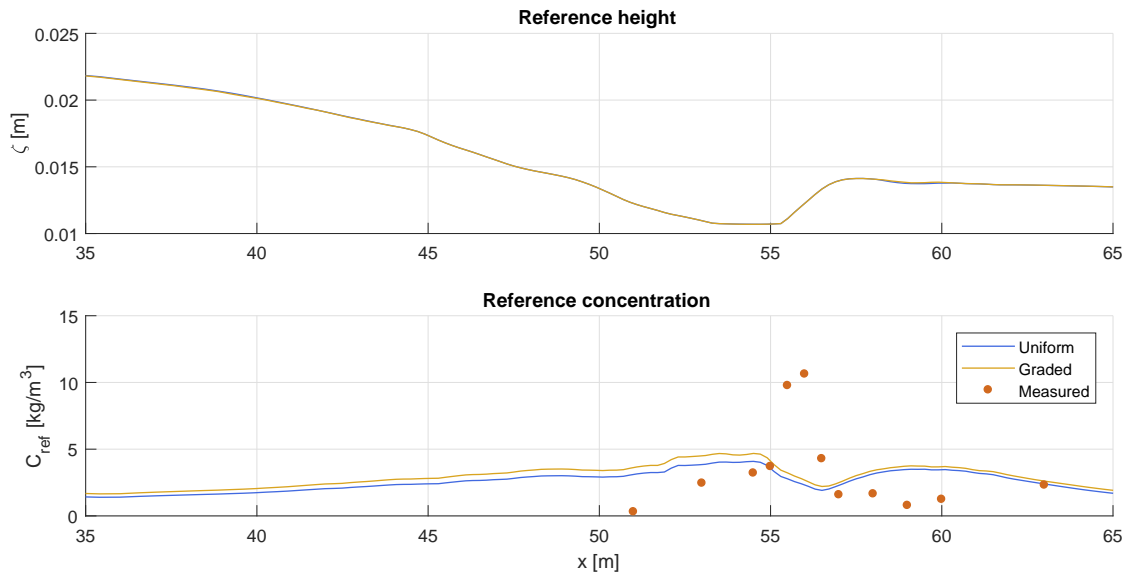


Figure 5.2: Modelled reference concentrations, with in the top figure the reference height at which the reference concentration was measured and modelled, and in the bottom figure the modelled (blue and yellow line) and measured (red dots) reference concentrations.

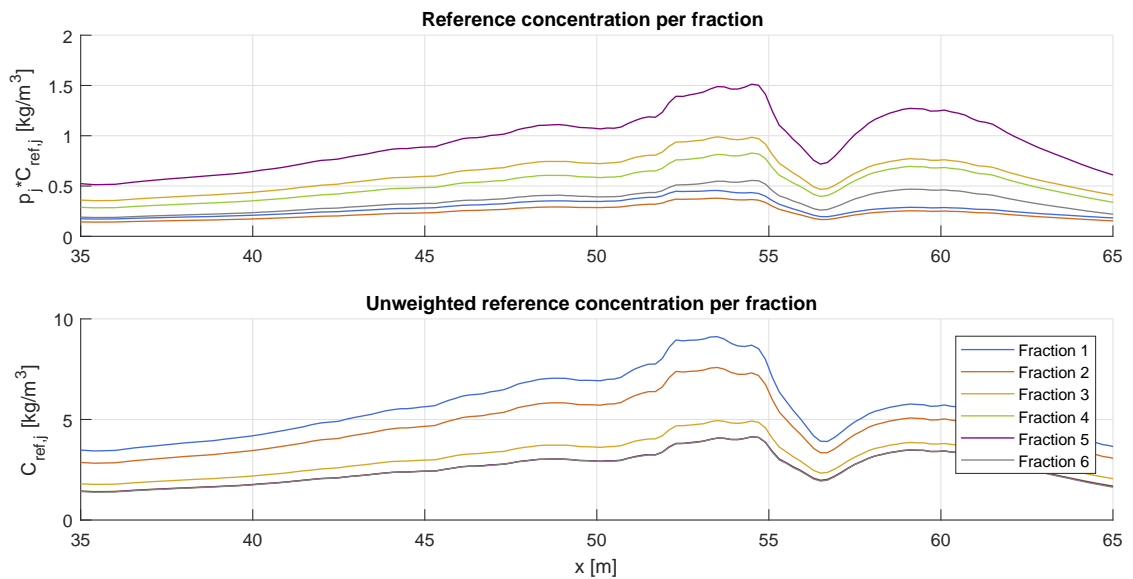


Figure 5.3: Modelled reference concentration per fraction, with in the top figure the weighted reference concentration per fraction where the potential reference concentration is multiplied with the percentage of a fraction in the mixture, and in the bottom figure the unweighted reference concentrations.

VERTICAL SUSPENDED SEDIMENT CONCENTRATION PROFILE

The suspended sediment concentrations above the bed for the twelve stations are presented in Figure 5.4.

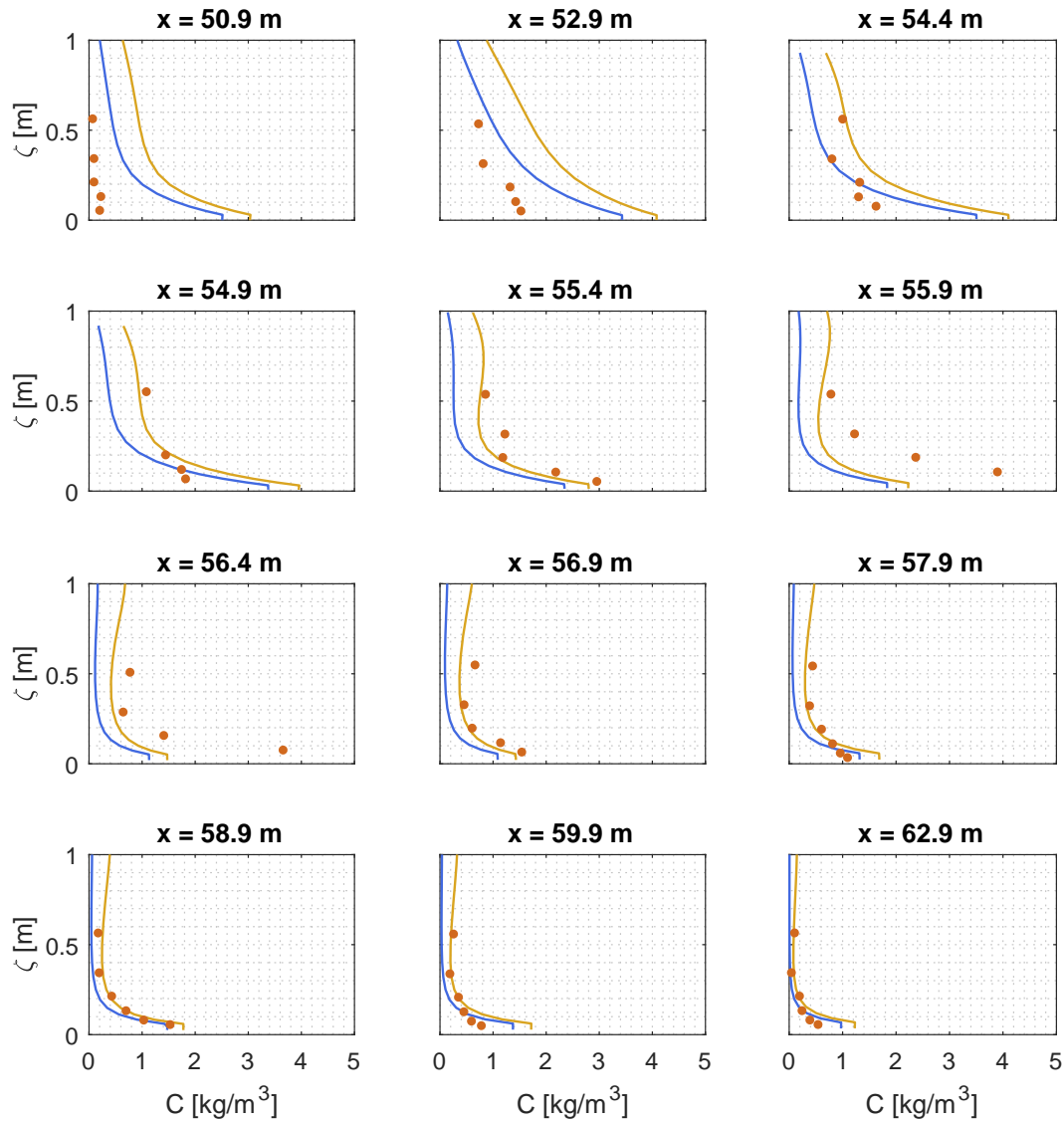


Figure 5.4: Modelled sediment concentrations above the bed, using a uniform (blue line) and graded approach (yellow line), with in red the measured concentrations (red dots) which were obtained using Transverse Suction System nozzles (TSS).

Generally, the suspended sediment concentrations are higher when a graded approach is used. This was also the case for the reference concentration (Fig. 5.2), from which the concentration profile (Rouse profile) is derived. Until $x=54.4\text{m}$ the concentrations are overestimated by the graded approach. Between at $x=55.9$ and 56.4m the concentrations are underestimated by the model, which is also seen in the reference concentration (Fig. 5.2) and is attributed to underestimation of the TKE. For $x>56.4\text{m}$ the measured concentrations are neatly reproduced by the model.

When investigating the weighted contribution per fraction (Fig. 5.5), fraction 5 gives the highest sediment concentrations as it covers nearly 37% of the mixture. The smallest fractions (fraction 1 and 2) hardly show any changes over the water depth. Only in the lower parts of the water column fraction 6 is present, which is logical, since this is the coarsest fraction. When investigating the unweighted suspended sediment concentrations in the water column (Fig. 5.6), the concentrations get higher when the grain size gets smaller. These finer fractions are the most mobile and are easier transported higher into the water column.

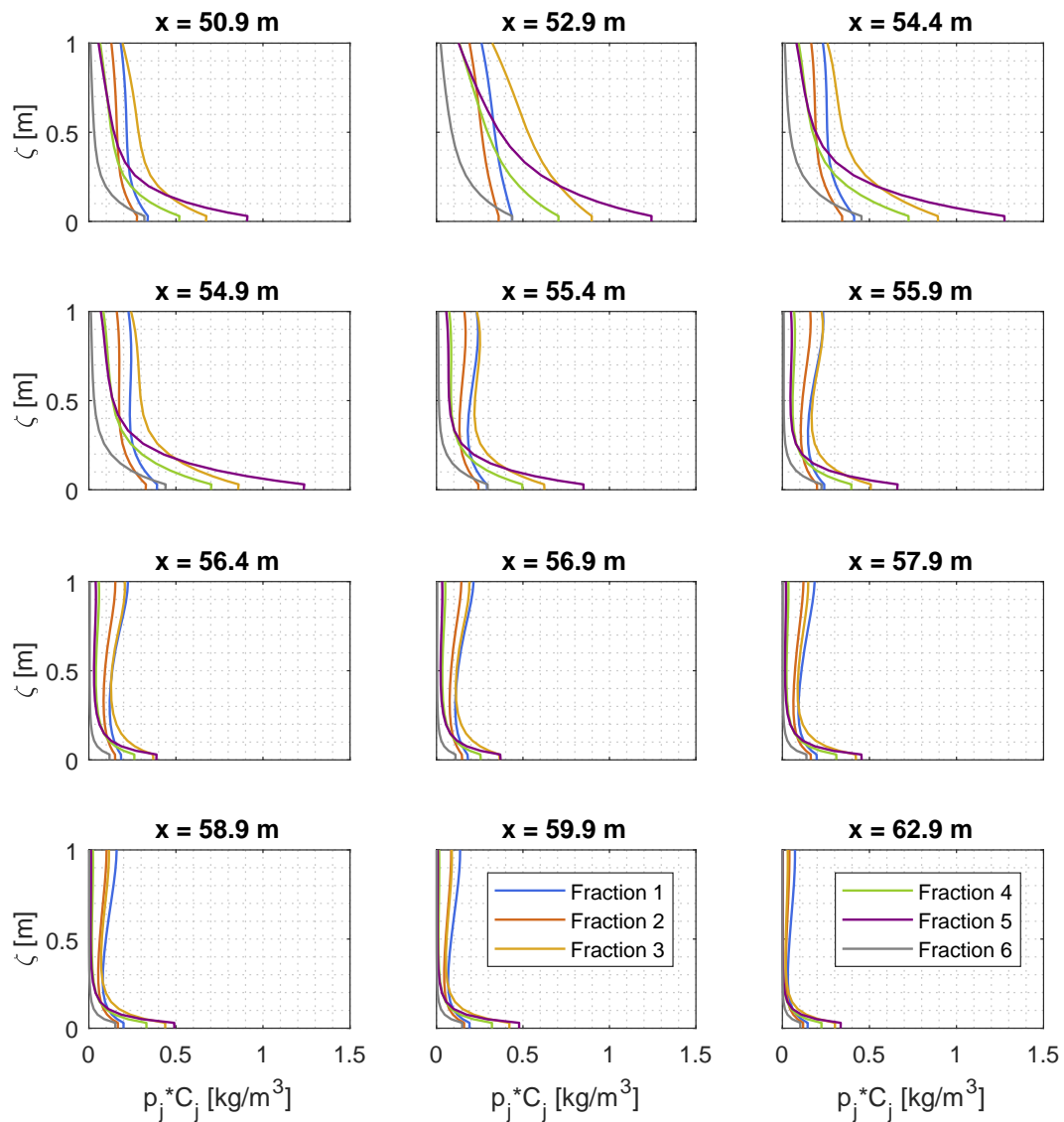


Figure 5.5: Modelled sediment concentrations per fraction.

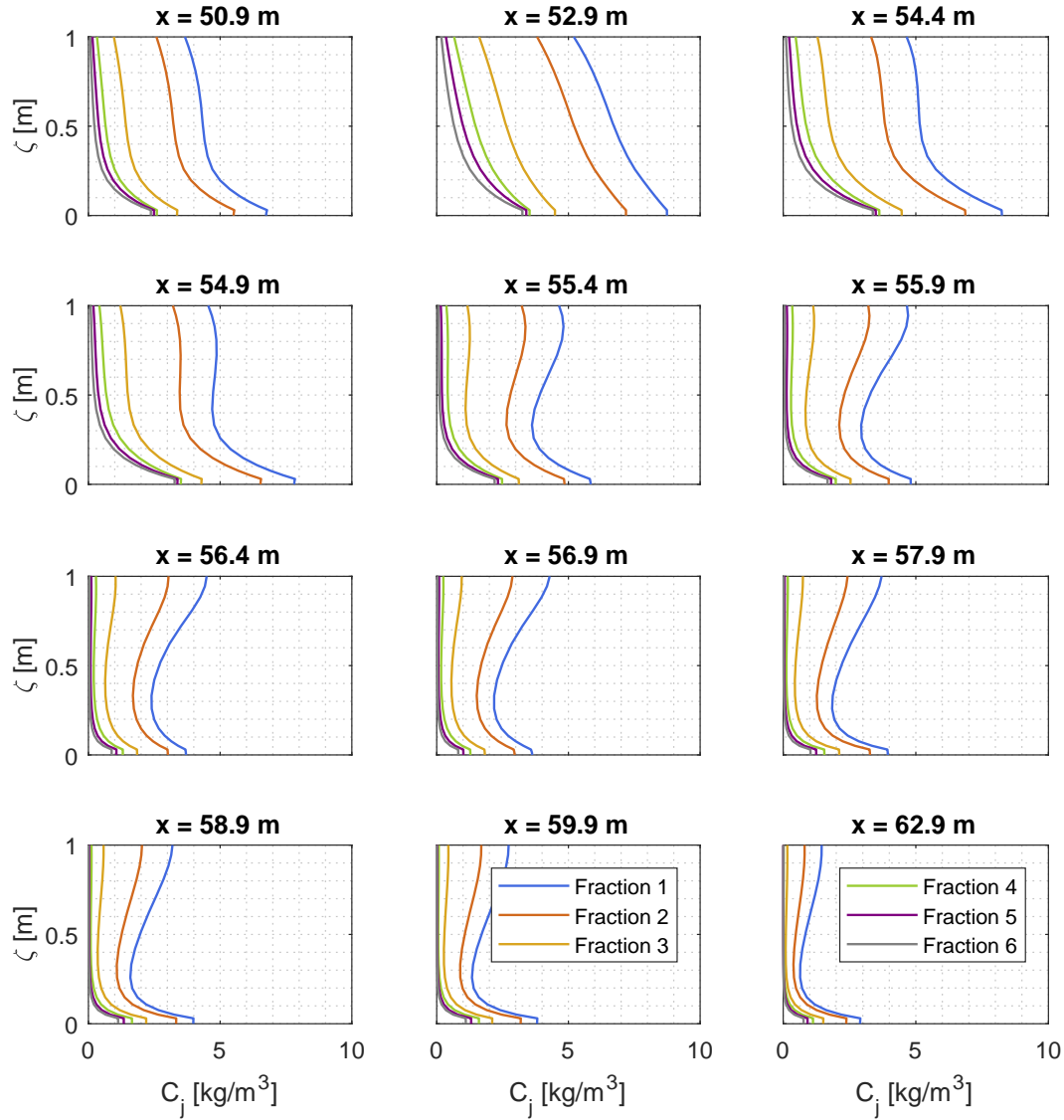


Figure 5.6: Unweighted modelled sediment concentrations per fraction.

5.2.2 GRAIN SIZE DISTRIBUTION IN THE WATER COLUMN

Besides cross-shore sorting, also vertical sorting in the water column takes place, which is presented in Figure 5.7. In this figure, the d_m in the water column is shown, where the black line denotes the original d_m in the bed and the red dots represent the measurements. The d_m of the mixture at different elevations was obtained by:

$$d_{m,\zeta} = \sum_{j=1}^N \frac{C_{j,\zeta}}{C_{tot,\zeta}} * d_{j,\zeta}, \quad (5.1)$$

with N the total number of fractions, $C_{j,\zeta}$ the concentration of sediment fraction j at ζ , $C_{tot,\zeta}$ the total concentration at ζ , and $d_{j,\zeta}$ the grain diameter of sediment fraction j at ζ .

At $x=50.9$ and $x>57.9$ m the data show grain sizes in the water column that are finer than those present in the bed. The waves break at $x\approx 53.5$ m, and the fine grains at $x=50.9$ m may be fine sediment that was entrained in the breaking region and then transported offshore (Van der Zanden et al., 2017). Within the breaker zone ($x\approx 53.5$ till 58.5 m), the gradient of the undertow is at its steepest (Fig. 4.5),

and the turbulent kinetic energy at its highest (Fig. 4.8 and 4.9) leading to vertical mixing, which results in coarse grains higher in the water column. The forces on the bed in the breaking region are thus large, that all the grain sizes are picked up, independent of their grain size (Van der Zanden et al., 2017). The vertical grain size distribution is presented in Figure 5.7.

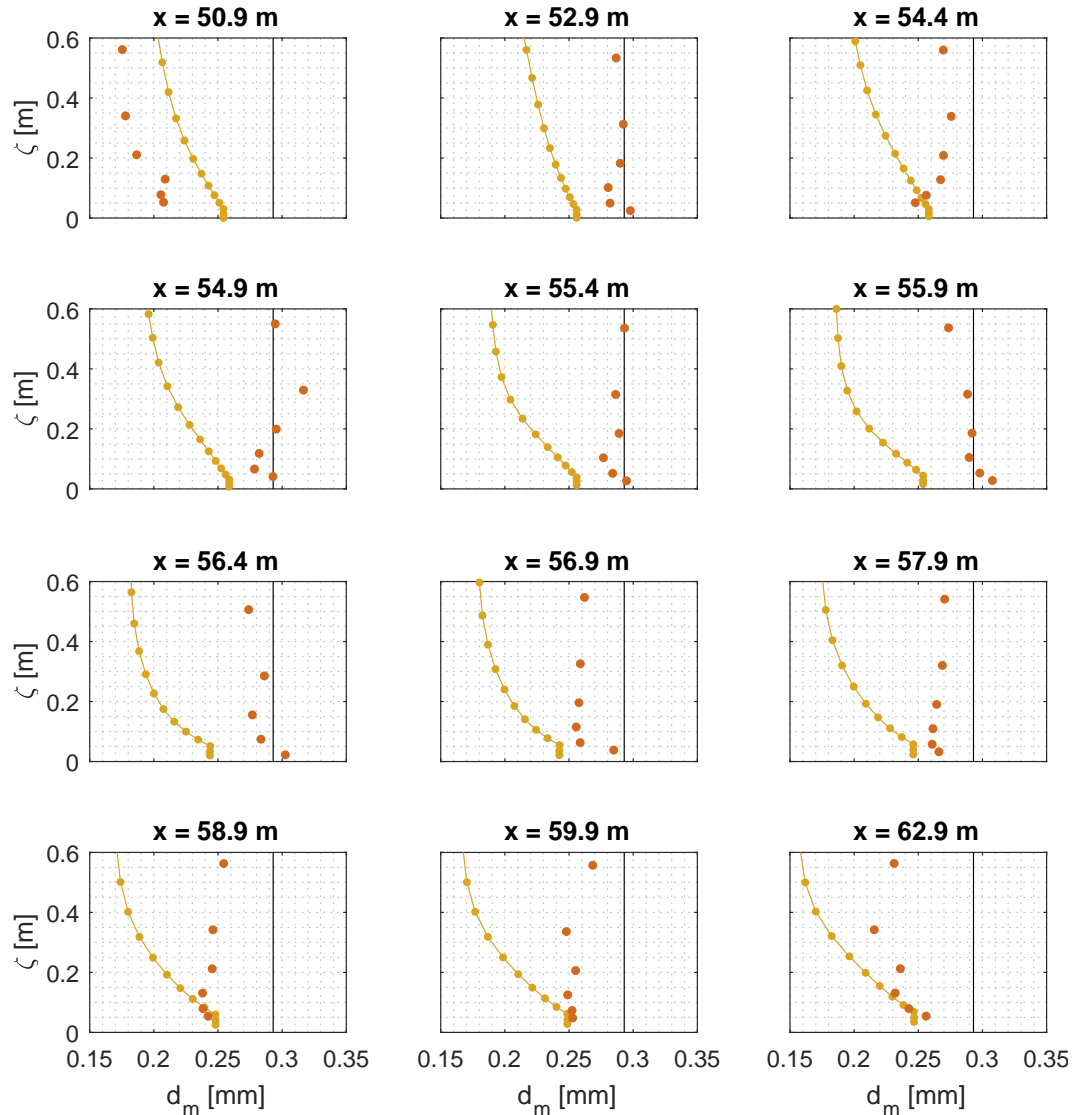


Figure 5.7: Modelled d_m above the bed, using a graded approach (yellow line with dots), with in red the measured d_m (red dots) and in black the original d_m of the bed (black solid line).

The modelled median grain sizes in the water column (yellow line) are always smaller than those present in the bed (black line). Furthermore, the grain sizes always become smaller towards the water surface. The model shows different results than the data, as the grain size always decreases with the elevation. Two methods have been used to calculate the grain size distribution: (1) the method explained previously based on the concentrations and (2) by deriving the d_m from the formulae for the fall velocity by Van Rijn, where d_m was the only unknown. Both approaches lead to the same results, and therefore confirm that the right d_m has been retrieved from the model results. As demonstrated in Chapter 4, the gradient of the undertow is underestimated in the breaking region. In combination with an underestimation of the TKE (Fig. 4.8), the upward mixing of sediment is also underestimated by the model, leading to finer sediment higher in the water column.

5.2.3 CROSS-SHORE SEDIMENT TRANSPORT

The cross-shore sediment transport of suspended sediment consists of two components: (1) the suspended sediment transport due to currents, and (2) the suspended sediment transport due to waves.

SUSPENDED SEDIMENT TRANSPORT DUE TO CURRENTS

The transport due to currents is presented in Figure 5.8, where the total suspended sediment transport due to currents is plotted in the first plot, the transport per fraction in the second plot and the unweighted transport in the third plot. In front of the breaking point ($x \approx 53.5\text{m}$) the transport rates are in the positive direction, but in the breaking region these transport rates are in the negative direction. The modelled and measured transport rates are both in the same direction, though the measured transport rates are underestimated at $x \approx 56.5\text{m}$.

Fraction 5, which covers $\approx 37\%$ of the mixture, gives the highest transport rates in both the positive and negative direction. The unweighted transport rates per fraction, show that the finer fractions are potentially more transported than the coarser fractions. The positive transport rates in front of the breaking point are mainly due to streaming effects. When streaming effects were switched off (Appendix 4.2.3, Fig. H.1), this behaviour was not noticed and the transport in the positive direction was absent.

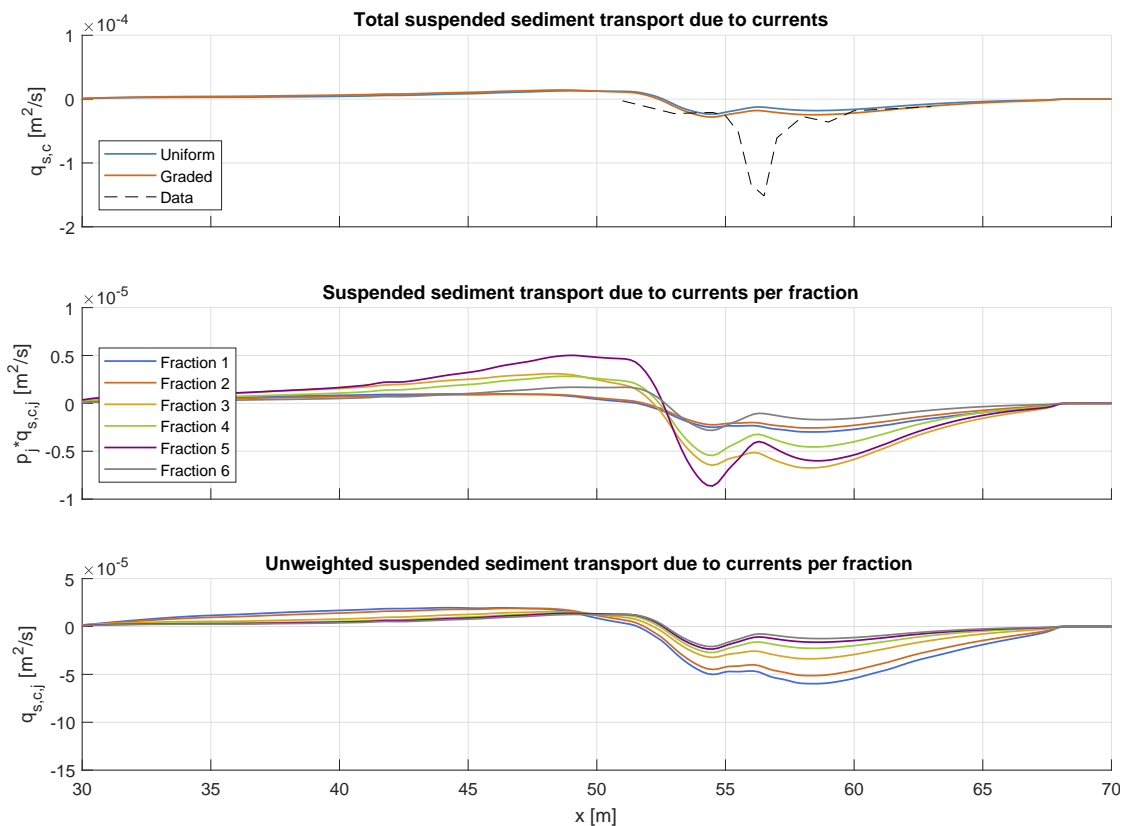


Figure 5.8: Suspended sediment transport due to currents, with in the first plot the total current related suspended sediment transport, in the second plot the transport per fraction and in the third plot the unweighted transport per fraction. Note that the scales of all the y-axes are different.

SUSPENDED SEDIMENT TRANSPORT DUE TO WAVES

Figure 5.9 shows the suspended sediment transport due to waves, where the graded approach is in better agreement with the data than the uniform approach. The peak in the data is given at $x=56\text{m}$, exactly at the location where the highest concentrations were measured (Fig. 5.4), but were underestimated by the model. The largest modelled concentrations, which overestimate the data, were given at $x<55.4\text{m}$. This explains why the observed peak in the wave-related suspended sediment transport rates is modelled earlier than was observed. The modelled sediment transport using a graded approach gives transport rates roughly three times smaller than the uniform approach ($x\approx 52\text{m}$), which is very large and not expected. When assuming no phase lag effects, the modelled sediment transport rates using a multi-fraction approach should give higher values than the single-fraction approach (Section 2.3, Van Rijn (2007c)). When phase lag effects are present however, this can cause differences between the uniform and graded approach as fine fractions are more sensitive to phase lag effects. The uniform approach uses a d_m of 0.29mm , whereas fractions 1 till 4 all have a d_m smaller than 0.29mm (Table 5.3). The third panel in Figure 5.9 shows that fractions 3 and 5 have the highest unweighted transport rates, which is also unexpected, as the unweighted transport rates should decrease with increasing grain size. The wave-related transport depends on the modelled reference concentrations, which show that the unweighted concentrations for the finer fractions are the highest, in contrast with what is shown for the wave-related suspended sediment transport.

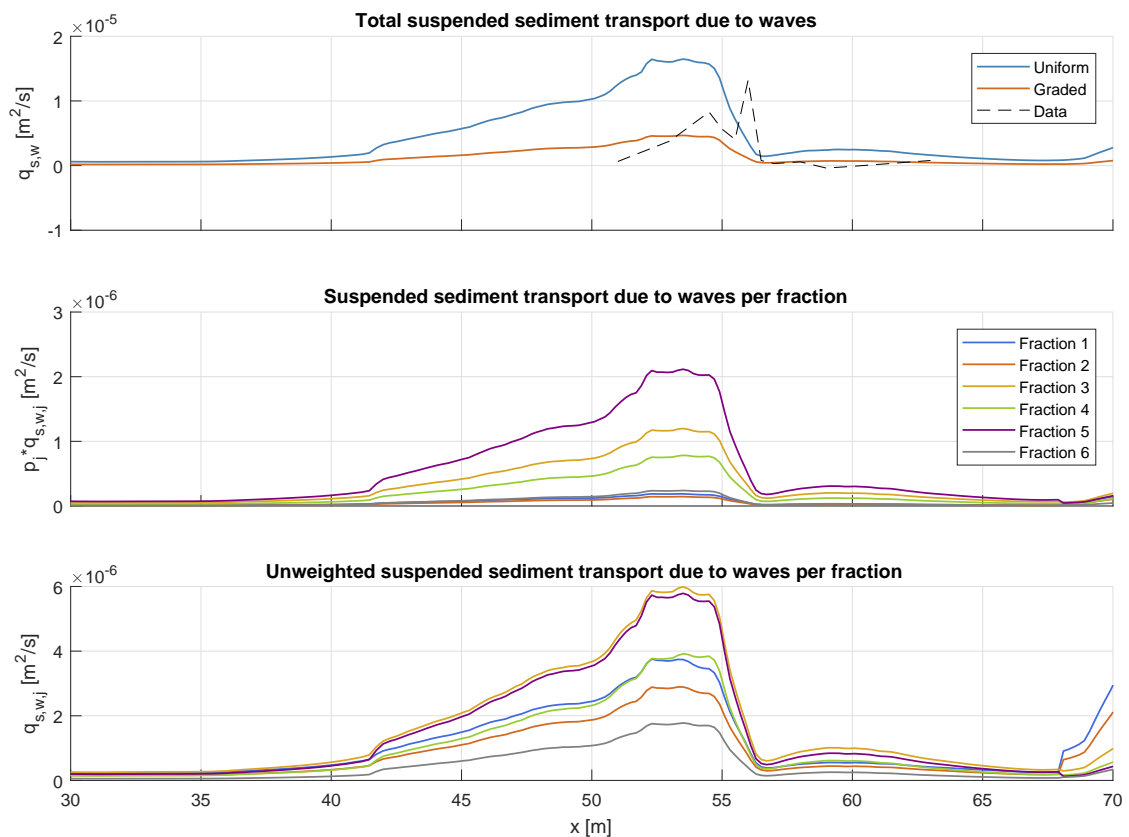


Figure 5.9: Suspended sediment transport due to waves, with in the first plot the total wave related suspended sediment transport, in the second plot the transport per fraction and in the third plot the unweighted transport per fraction. Note that the scales of all the y-axes are different.

5.3 BED-LOAD TRANSPORT

In Figure 5.10 the bed-load transport due to currents and waves is shown. Whereas the majority of the bed-load transport was observed in the positive direction, the model shows transport rates in the negative direction after $x=54\text{m}$ for both the uniform and graded approach. The observed peak in bed-load transport is located at $x\approx 56.5\text{m}$, which is after the top of the breaker bar on the lee side. Due to the steep slope of this breaker bar, the angle of repose may be approached, leading to downward induced sediment transport in the onshore direction (Van der Zanden, 2016). Even though the undertow and orbital velocities were observed in the negative direction, the bed-load transport is primarily directed onshore. This sloping effect may not be modelled by DELFT3D. Additionally, the modelled onshore directed orbital velocities are slightly lower than those directed offshore (Fig. 4.7). However, the undertow is very strong near the bed (Fig. 4.4), causing offshore directed bed-load transport. Again, fraction 5 has the largest contribution regarding the weighted transport per fraction, where fraction 1 and 2 hardly show any transport rates. The unweighted transport even shows that the coarser the fraction, the larger the potential transport rates.

The difference between the uniform and graded approach is very small, which is in agreement with the results found in Chapter 3. In this chapter the stand-alone bed-load transport model of Van Rijn hardly showed any differences between the graded and uniform approach.

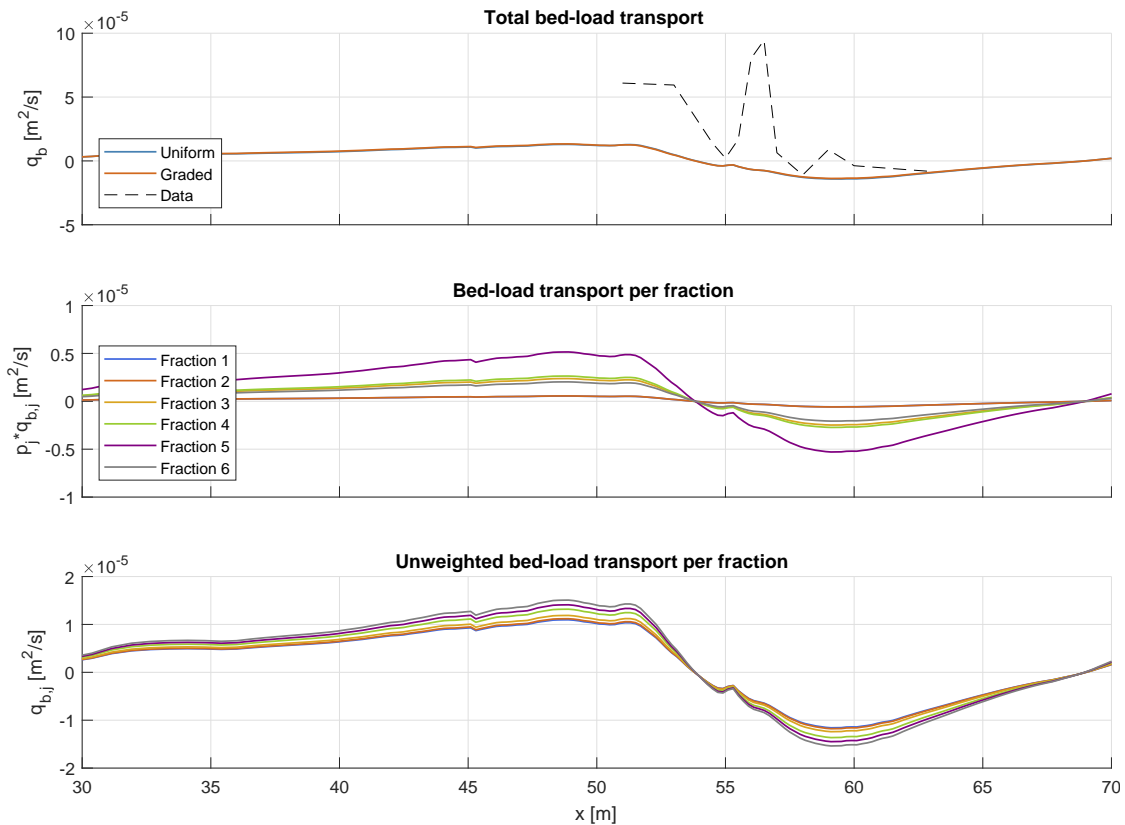


Figure 5.10: Bed-load transport due to currents and waves, with in the first plot the total bed-load transport, in the second plot the transport per fraction and in the third plot the unweighted transport per fraction. Note that the scales of all the y-axes are different.

5.4 TOTAL NET TRANSPORT RATES

The total sediment transport, which is the sum of the wave- and current-related suspended sediment transport and bed-load transport, is presented in Figure 5.11. The contribution of the components is shown in Table 5.4.

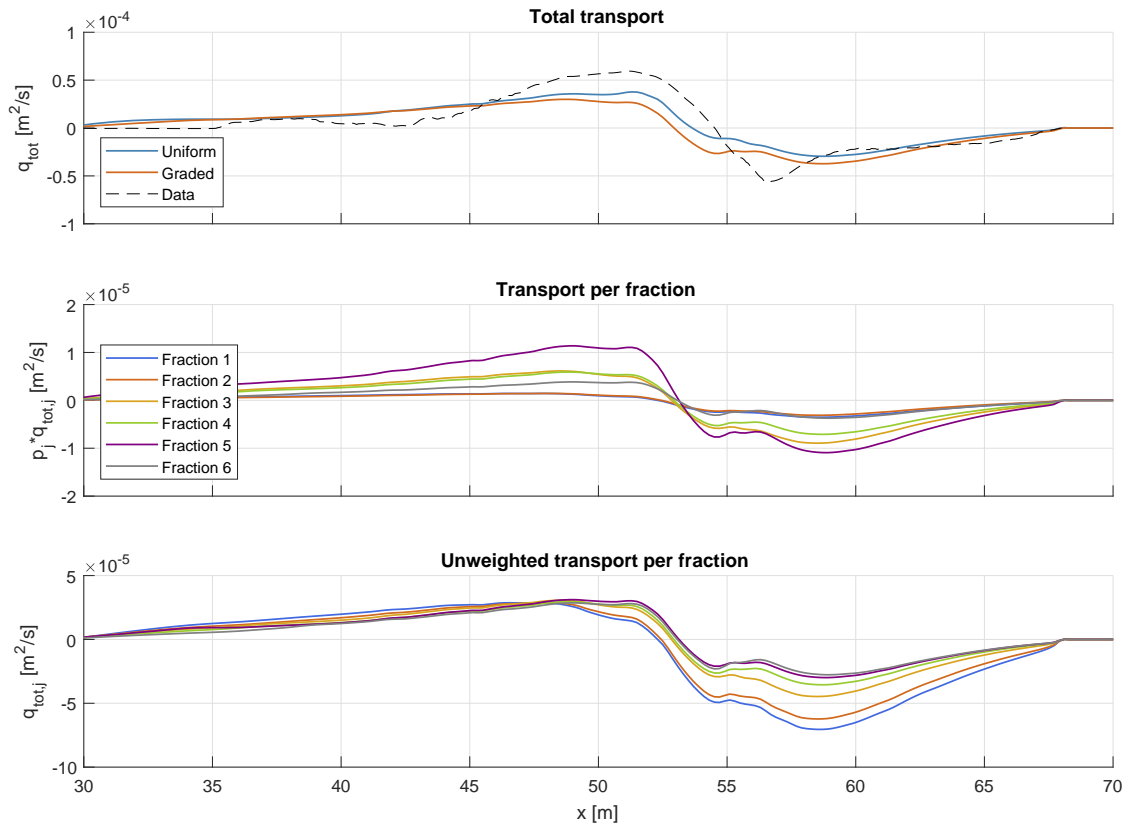


Figure 5.11: Total transport, with in the first plot the total transport, in the second plot the transport per fraction and in the third plot the unweighted transport per fraction. Note that the scales of all the y-axes are different.

Table 5.4: Modelled and measured contributions of the different transport components for both the uniform and graded approach, calculated with $\frac{|q_{xx}|}{|q_{sc}|+|q_{sw}|+|q_b|}$.

		Modelled	Measured
Uniform	q_{sc}	46%	29%
	q_{sw}	23%	2%
	q_b	31%	68%
Graded	q_{sc}	54%	29%
	q_{sw}	7%	2%
	q_b	39%	68%

Compared to the graded approach, the uniform approach gives higher transport rates in the positive direction, but lower transport rates in the negative direction. This can be attributed to the wave-related suspended sediment transport, which is the only component that shows a clear difference between the approaches. Additionally, the current-related shows slightly lower transport rates in

the negative direction for the uniform approach. However, it is doubted whether DELFT3D calculates the wave-related suspended sediment transport correctly. When this is not the case and the values are incorrect, there is no distinct difference between the graded and uniform approach. According to Table 5.4, q_{sw} provides the smallest contribution to the total modelled transport rates.

The weighted transport per fraction shows the highest transport rates for fraction 5, with the largest difference before the breaking point ($x \approx 53.5\text{m}$), mainly caused by the bed-load transport and suspended sediment transport due to currents which are both modelled onshore. At $x = 56.5\text{m}$ the peak in the offshore directed transport is underestimated by both the uniform and graded approach. This is due to underestimation of the current-related suspended sediment transport and the concentrations. The unweighted transport shows that the fine fraction potentially gives higher transport rates, and that the fine fractions are also the quickest to reverse the direction.

5.5 CONCLUSION

This chapter gives answer to research questions 2: *What are the effects of using a graded sediment approach instead of a uniform approach in DELFT3D regarding the (a) suspended sediment concentrations, (b) suspended sediment grain sizes, and (c) cross-shore net total sediment transport?*

The modelled reference concentrations underestimate the observed reference concentrations between $x = 55$ and 56.6m . At these locations the observed turbulent kinetic energy is very strong, and reaches its maximum values. This energy may enhance the concentrations as more sediment is mobilised (Van der Zanden et al., 2017). However, these effects are not incorporated in the formula for the reference concentration. The reference concentration using a graded approach is slightly higher, which is possibly due to the fine fractions which are easily mobilised. The vertical concentration profiles show that the concentrations of the graded approach are always higher than that of the uniform approach. As the reference concentrations are already higher for the graded approach, the rest of the profile also gives higher concentrations than the uniform approach. From $x = 50.9$ till 54.4m both approaches overestimate the measured concentrations, but the overall concentrations of the uniform approach are lower, and are thus in better agreement with the data. At $x = 55.9$ and 56.4m both approaches underestimate the measured concentrations. At both locations the undertow is underestimated by the model, leading to discrepancies between the modelled and measured concentrations. After $x = 56.4\text{m}$ the graded approach seems to perform better for the given dataset.

The modelled grain sizes in the water column are larger than the data at $x = 50.9\text{m}$, but are finer at all other locations, and are always finer than the d_m in the bed. The observed grain sizes measured at $x = 50.9\text{m}$ may be fine sediment that was entrained in the breaker zone, but was then transported offshore. Due to larger values for the turbulent kinetic energy a lot of vertical mixing takes place, resulting in coarser grains higher in the water column. Underestimation of this energy may probably also cause the underestimation in grain sizes in the water column.

Both the uniform and graded approach give comparable results for the current-related suspended sediment transport and bed-load transport, where observed peaks in the data are not replicated by the model. Chapter 3 already showed hardly any differences between the uniform and graded approach for the modelled bed-load transport rates using Van Rijn (2007c). For the current-related suspended sediment transport, this is due to the underestimation of the gradient of the undertow at $x \approx 56.5\text{m}$. The bed-load transport rates for both approaches however, are modelled in the wrong direction ($x \approx 56.5\text{m}$). This may be attributed to the the slope on the lee side of the breaker bar ($x = 55$ till 57m), where downward induced bed-load transport in the onshore direction takes place during the experiment. This effect is not incorporated in DELFT3D, and as the offshore directed undertow

velocities are strong at this location, bed-load transport is modelled in the offshore direction. Only the wave-related suspended sediment transport shows a clear difference between the two approaches, where it is unknown whether this is actually due to grading effects or a bug in DELFT3D. DELFT3D uses a different method to calculate this transport component than was shown in Section 2.4.3, which is based on the reference concentration and Van Rijn's mixing coefficient, so the calculated concentrations presented in Section 5.2.1 are not one-to-one linked with the wave-related suspended sediment transport. Additionally, fraction 5 shows the largest unweighted transport, which does not seem logical, assuming that fine fractions are mobilised more easily. Analysis of the total transport rates has shown that the graded approach gives smaller transport rates in the onshore direction, but larger transport rates in the offshore direction when compared to the uniform approach. This effect can be attributed to the difference in wave-related suspended sediment transport, where the transport in the positive direction is larger for the uniform approach.

6

DISCUSSION

During this research, some uncertainties were encountered. These uncertainties are discussed consequently for (1) the modelling of the bed-load transport rates, (2) the measurements taken during the wave-flume experiments, (3) the modelling of the hydrodynamics and (3) the modelled suspended sediment transport due to waves.

6.1 MODELLING BED-LOAD TRANSPORT RATES

A number of remarks can be made regarding the modelling of bed-load transport with the SANTOSS and Van Rijn model.

VAN RIJN MODEL: CONVERSION FROM FORTRAN TO MATLAB

In the formulations of the Fortran code (TR2004 (Van Rijn et al., 2004)), a number of tweaking parameters was used by Van Rijn to enhance the models performance. Furthermore, streaming effects due to free-surface waves were included, though for the oscillatory flow tunnel experiments this effect was assumed to be absent due to the absence of these waves. Both these aspects are now excluded from the MATLAB code, yielding differences between the computed transport rates by Fortran and MATLAB. Excluding streaming effects reduced the bed-load transport rates by a factor 1.5 to 2 (Appendix F), and compared to the SANTOSS model the transport rates computed by Van Rijn are relatively low.

WAVE-RELATED SUSPENDED SEDIMENT TRANSPORT VAN RIJN

The bed-load transport computed in DELFT3D consists of 3 components, namely the (1) bed-load transport due to waves, (2) bed-load transport due to currents and (3) suspended sediment transport due to waves. Within the formulation of this last component a factor for the wave asymmetry is incorporated, and this is the only component in which phase lag effects are incorporated. In the stand-alone bed-load transport model for Van Rijn, only the bed-load transport due to currents and waves is calculated, ignoring the wave-related suspended sediment transport and any phase lag effects. Section 3.1 showed that all the sediment transport rates were always modelled in the positive direction, even though some transport of the fine fraction was measured in the negative direction. This implies that phase lag effects should be incorporated in the stand-alone bed-load transport formulations, since during the experiments phase lag effects were noticed in the transport of suspended sediment transport.

CALIBRATION AND VALIDATION OF THE SANTOSS MODEL

The SANTOSS model was originally calibrated and validated with the dataset used for this thesis. Though the performance of the model for the different fractions had not yet been calibrated and

validated before, it only seems reasonable that the total net transport rates are in accordance with the used database. Therefore, comparing the performance of the SANTOSS and Van Rijn model to this database is unfavourable for the latter, as the transport rates computed by the Van Rijn were not calibrated using this dataset.

DIFFERENCE BETWEEN UNIFORM AND GRADED APPROACH

The SANTOSS model shows clear differences between the uniform and graded approach, which is not the case for the Van Rijn model. When using a uniform approach in SANTOSS, the bed-load transport rates increase. Within SANTOSS, sediment transport of the fine fraction has been modelled in both the positive and negative direction due to phase lag effects. These phase lag effects only apply when fine sand stays in the water column until the consecutively crest our trough cycle. Generally, the median grain size of a mixture (d_{rep}) is larger than that of the fine fraction when using the graded approach. So when the mixtures are treated as uniform, the grain diameters are possibly too large to stay in the water column until the consecutive cycle. When the transport rates of the different fractions within a mixture were modelled in both the positive and negative direction, the sum of these transport rates resulted in a net positive transport rate. However, when no phase lag effects are endured and the transport is only in one direction, the uniform approach may result in higher magnitudes of the net total transport rates. The Van Rijn formula does not take phase lag effects into account, and the transport rates of the different fractions are all in the same direction. This may explain why the difference between the uniform and graded approach is small using the Van Rijn model.

6.2 MEASURING INSTRUMENTS WAVE FLUME EXPERIMENTS

It is possible that there were errors in the data measured during the experiments. The data used to calibrate the wave height were measured with resistive wave gauges and pressure transducers. It was assumed that the largest transport rates were generated in the wave breaking region, which made it important to model the wave height accurately in this region. As resistive wave gauge measurements were absent at this location, the model was calibrated for the pressure transducers. However, around the breaking point the measured wave height by the different instruments differ about 0.1m, which is a significant difference and introduces an uncertainty within the model. Furthermore, the wave height was obtained indirectly by the pressure transducers, as the linear wave theory was required to calculate the wave height.

6.3 MODELLING HYDRODYNAMICS WAVE FLUME EXPERIMENTS

During the SINBAD experiments, regular waves were used in combination with a breaker bar with a slope 1:10. The bed level increased from $x=30$ till 55m, after which the bed level decreased from $x=55$ till 57m with approximately 0.5m. Firstly, DELFT3D was designed for irregular wave conditions. Even though Schnitzler (2015) modified the formulations for the wave height of regular breaking waves, there are still formulations in DELFT3D which were adapted for irregular waves (Deltares, 2018). Secondly, DELFT3D assumes shallow water, which reduces the vertical momentum equation to the hydrostatic pressure equation (Lesser et al., 2004). This means that the vertical accelerations are neglected, as they are assumed to be small compared to the gravitational acceleration. However, due to the large undertow velocities, vertical acceleration effects may play a role in these experiments.

6.4 MODELLED SUSPENDED SEDIMENT TRANSPORT DUE TO WAVES

When modelling the wave-related suspended sediment transport in DELFT3D, the uniform approach shows transport rates about three times larger than the graded approach. Due to the non-linear relation between the grain size and suspended sediment transport, the graded approach should give larger transport rates than the uniform approach (Section 2.3). However, this is not the case when phase lag effects prove to be important. Furthermore, the unweighted transport rates per fraction show that the finer fractions do not give the highest values, though this is expected as fine sediment is more mobile than coarse sediment. Investigation of the source code of DELFT3D has not yet provided any explanation as to why this happens. Besides the fact that DELFT3D does not use the concentration profile which was calculated in Section 5.2, but uses the reference concentration and Van Rijn's mixing distribution, it can still not be explained why there is such a difference between the uniform and graded approach.

CONCLUSIONS AND RECOMMENDATIONS

7.1 CONCLUSIONS

The objective of this research was: *Assessment of DELFT3D for cross-shore graded sediment transport under waves*. This objective has been achieved by answering two research questions.

RESEARCH QUESTION 1

How well do practical models for bed-load transport predict oscillatory sheet-flow transport of mixed sediments and how can these models be improved?

To answer this research question, the modelled bed-load transport rates by the Van Rijn and SANTOSS model have been validated using oscillatory flow tunnel data. Both models gave the best results when a graded approach was used, together with a representative grain diameter of d_{mean} . This grain diameter is the weighted mean diameter of all fractions. The best setting of the Van Rijn model computes transport rates with an RMSE of $0.17 * 10^{-4} m^2/s$ and 79% within a factor 2 of the data. Using this model, only a small difference in computed transport rates was observed between the uniform and graded approach. The best results obtained by the SANTOSS model gave an RMSE of $0.10 * 10^{-4} m^2/s$ with 95% within a factor 2 of the data. Here the difference between the uniform and graded approach was larger than for the Van Rijn model.

RESEARCH QUESTION 2

What are the effects of using a graded sediment approach instead of a uniform approach in DELFT3D regarding the (a) suspended sediment concentrations, (b) suspended sediment grain sizes, and (c) cross-shore net total sediment transport?

In front of the breaker bar ($x \approx 55m$) the model has difficulties reproducing the reference concentrations, as it systematically overestimates the measured reference concentrations. Around the plunge point ($x \approx 55.5m$), where the highest concentrations were measured, the model underestimates the data. The reference concentration using a graded approach is slightly higher, which is possibly due to the fine fractions which are easily mobilised. The concentration profiles are derived from the reference concentration, and also underestimate the data between $x=55$ and $56.5m$. As the reference concentrations are higher using the graded approach, the same occurs for the vertical concentration profile. Further behind the breaker bar ($x > 65.5m$) the shape of the concentration profile is steeper, which is in better agreement with the data than before the breaker bar. Both the graded and uniform approach give accurate results regarding the measured concentrations further behind the breaker bar.

Due to the high undertow velocities, a lot of mixing occurs and relatively coarse sediment is observed high in the water column. DELFT3D has problems replicating these data as the modelled grain

sizes become smaller towards the water surface, which gives large differences between the modelled and measured grain sizes.

The total net transport rates are split up in 3 components, namely: (1) current-related suspended sediment transport, (2) wave-related suspended sediment transport and (3) current- and wave-related bed-load transport. The current-related suspended sediment transport gives comparable transport rates for the uniform and graded approach, with underestimation of the observed peak transport due to underestimation of the gradient of the undertow. The unweighted transport per fraction shows that the finer fractions give higher transport rates and have the highest potential to be transported as suspended sediment transport due to currents.

The wave-related suspended sediment transport shows transport rates for the graded approach that are three times lower than for the uniform approach. When phase lag effects are ignored, a graded approach should give higher transport rates than the uniform approach due to non-linearity between grain sizes and transport rates. However, when phase lag effects do become important, larger differences between the uniform and graded approach may be observed. Another explanation could be that DELFT3D calculated this transport component differently for the uniform and graded approach, or that there is a bug in the model. The maximum wave-related suspended sediment transport is modelled too early by both models. This is in agreement with the reference concentrations and vertical concentration profiles to which the suspended sediment transport due to waves is related.

The uniform and graded approach give comparable results for the bed-load transport rates, which is in agreement with the results obtained in Chapter 3. The measured and modelled transport are not in the same direction, which may be attributed to the slope of the breaker bar on the lee side which induces downward onshore sediment transport. However, due to the strong undertow near the bed in the offshore direction, DELFT3D models the transport offshore. The unweighted transport shows that the coarser the grains, the higher the transport rates. It is possible that the streaming near the bed is so strong that it does not matter for the model what the size of the grains is, as it is transported anyway.

The total transport rates show that when the transport is directed onshore, the uniform approach gives higher transport rates, whereas for transport in the offshore direction the graded approach gives higher values. This effect can be attributed to the wave-related suspended sediment transport and as it is unknown whether DELFT3D computes the wave-related transport correctly, nothing can be concluded for certain about the differences in total net transport rates. Fraction 5 shows the largest contribution to the weighted transport, as it covers nearly 37 % of the mixture. The unweighted transport shows the highest transport rates for the fine sediment, which is expected since these fractions are more mobile. Finally, the finer fractions also are the first to change direction and are the most sensitive to flow velocities.

From the conclusions drawn previously, the final conclusion can be drawn that graded sediment transport rates can indeed be modelled by DELFT3D, whereas the uniform and graded approach both give comparable results. There is no clear improvement using the graded approach with respect to the uniform approach. When there is more clarity about the computation of the wave-related suspended sediment transport within DELFT3D and what established the differences between the two approaches, more conclusions can be drawn regarding the performance of the model. However, based on the modelled suspended sediment transport rates due to currents and the bed-load transport rates due to currents and waves, the graded approach does not seem necessary to replicate the transport rates which were observed during the SINBAD experiments.

7.2 RECOMMENDATIONS

Based on the results, discussion and conclusion, some recommendations can be done.

IMPROVING HYDRODYNAMICS

Between $x=55$ and 57m the gradient of the undertow is significantly underestimated by the model. This gradient causes mixing effects of suspended sediment, leading to larger concentrations in the water column. At the locations where the gradient is underestimated, the concentrations are underestimated as well and therefore also the suspended sediment transport rates. It is recommended that first the hydrodynamics are properly modelled, before the formulations for sediment transport are modified.

SUSPENDED SEDIMENT TRANSPORT DUE TO WAVES

When modelling the sediment transport rates with DELFT3D, the wave-related suspended sediment transport rates for the graded approach were three times lower than for the uniform approach. This can either mean that the graded approach is strongly affected by phase lag effects, or that DELFT3D calculates this component differently for both the uniform and graded approach. The latter should not be true, as the transport rates are based on the reference concentration and mixing coefficient for both approaches. Therefore it is recommended to carry out further research on how these different values for the transport rates were obtained.

SANTOSS GRADED SEDIMENT APPROACH IMPLEMENTATION IN DELFT3D

Due to the limited time available for this thesis project, it has been decided to not implement the SANTOSS formulations for graded sediment transport in DELFT3D. Validation of the stand-alone bed-load transport models however, showed that the SANTOSS model gives better results than Van Rijn when validated with the SANTOSS database. Therefore, it would be interesting to investigate the effects on the transport rates in DELFT3D when the SANTOSS formulations for graded sediment transport are used instead of Van Rijn.

OTHER EXPERIMENTS WITH GRADED SEDIMENT

It would be interesting to model graded sediment transport using another dataset, which is different than the SINBAD experiments for the following aspects:

1. **Irregular waves**

The SINBAD experiments use regular waves, whereas DELFT3D was designed for irregular waves. Even though Schnitzler (2015) modified a number of hydrodynamic formulations in order to make DELFT3D suitable for regular wave conditions, the model was still designed and parametrised for irregular waves, and it would be useful to carry out an experiment with irregular waves.

2. **Positive bed slope**

The bed profile as used in the experiments first has a positive slope towards the breaker bar, but after $x=55\text{m}$ there is a negative bed slope. This slope may be the cause of the observed onshore directed bed-load transport, even though larger orbital velocities near the bottom are directed in the offshore direction. Excluding this extra complication makes it easier to analyse grading effects. Additionally, a more gentle slope could be applied in the bed.

3. **Non-breaking waves**

Breaking waves also introduce an extra complicated situation, where a lot of mixing due to high velocities for the undertow and turbulent kinetic energy takes place. Excluding this from the experiments, makes it possible to solely focus on grading effects.

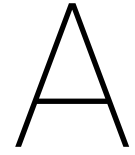
4. **Larger variety of grain sizes in the bed**

The sediment used for this experiment was not very graded. Therefore, experiments that are used for the purpose of analysing graded sediment effects, should have a larger spread in grain sizes. As a reference the SANTOSS database can be used (Table 2.1).

REFERENCES

- Borsje, B. (2013). Marine Dynamics, Chapter 7: Sand transport processes and models. In *Marine dynamics* (pp. 1–23).
- Cáceres, I., Cooke, R., Thorne, P., Hurther, D., & Sánchez-Arcilla, A. (2018). *Ripple Complex Experiments (RIPCOM). Data report UPC*. (Tech. Rep.).
- Chai, T., & Draxler, R. R. (2014). Root mean square error (RMSE) or mean absolute error (MAE)? -Arguments against avoiding RMSE in the literature. *Geoscientific Model Development*, 7(3), 1247–1250. doi: 10.5194/gmd-7-1247-2014
- Day, T. J. (1980). *A study of the transport of graded sediments*. (Tech. Rep.).
- Deltares. (2018). Delft3D-Flow user manual. , 710.
- Egiazaroff, I. V. (1965). Calculation of nonuniform sediment concentrations. *Journal of the Hydraulics Division*, 91(4), 225–247.
- Hamm, L., Katapodi, I., Dohmen-Janssen, M., Ribberink, J., Samothrakis, P., Cloin, B., ... Hein, R. (1998). *Grain size, gradation and density effects on sediment transport processes in oscillatory flow conditions. Data report, Part I.WL|Delft Hydraulics, the Netherlands*. (Tech. Rep.). Delft Hydraulics.
- Hassan, W. N. (2003). *Transport of size-graded and uniform sediments under oscillatory sheet-flow conditions* (Unpublished doctoral dissertation). University of Twente.
- Hassan, W. N., & Ribberink, J. S. (2005). Transport processes of uniform and mixed sands in oscillatory sheet flow. *Coastal Engineering*, 52(9), 745–770. doi: 10.1016/j.coastaleng.2005.06.002
- He, M. (2017). *Improving Suspended Sediment Transport Models for Breaking Wave Conditions* (Tech. Rep.).
- Huisman, B. J., de Schipper, M. A., & Ruessink, B. G. (2016). Sediment sorting at the Sand Motor at storm and annual time scales. *Marine Geology*, 381, 209–226. Retrieved from <http://dx.doi.org/10.1016/j.margeo.2016.09.005> doi: 10.1016/j.margeo.2016.09.005
- Indiawrm. (2015). *Hydrological Information system*.
- Knaapen, M. A. F., Holzhauer, H., Hulscher, S., Baptist, M., DeVries, M., & Van Ledden, M. (2003). On the modelling of biological effects on morphology. In *River, coastal and estuarine morphodynamics, barcelona, spain* (pp. 773–783).
- Lesser, G. R., Roelvink, J. A., van Kester, J. A., & Stelling, G. S. (2004). Development and validation of a three-dimensional morphological model. *Coastal Engineering*, 51(8-9), 883–915. doi: 10.1016/j.coastaleng.2004.07.014
- Miller, M. C., Mc Cave, I. N., & Komar, P. D. (1977). Threshold of sediment motion under unidirectional current. *Sedimentology*, 24(4), 507–527.
- O'Donoghue, T., & Wright, S. (2004). Concentrations in oscillatory sheet flow for well sorted and graded sands. *Coastal Engineering*, 50(3), 117–138. doi: 10.1016/j.coastaleng.2003.09.004
- Ribberink, J. S. (1998). Bed-load transport for steady flows and unsteady oscillatory flows. *Coastal Engineering*, 34(1-2), 59–82. doi: 10.1016/S0378-3839(98)00013-1
- Ribberink, J. S. (2011). *River Dynamics II : Transport Processes and Morphology* (No. March).
- Schnitzler, B. (2015). *Modelling sand transport under breaking waves* (Tech. Rep.).
- Smith, E. R., & Kraus, N. C. (1991). Laboratory study of wave breaking over bars and artificial reefs. *Waterways, Port, Coastal, and Ocean Engineering*, 117, 307–325.
- The Open University. (1999). *Waves, Tides and Shallow Water Processes* (2nd ed.). Oxford: Butterworth-Heinemann.
- Van der A, D. A., Ribberink, J. S., Van der Werf, J. J., O'Donoghue, T., Buijsrogge, R. H., & Kranenburg, W. M. (2013). Practical sand transport formula for non-breaking waves and currents. *Coastal*

- Engineering*, 76, 26–42. Retrieved from <http://dx.doi.org/10.1016/j.coastaleng.2013.01.007> doi: 10.1016/j.coastaleng.2013.01.007
- Van der Werf, J. J., Schretlen, J. J., Ribberink, J. S., & O'Donoghue, T. (2009). Database of full-scale laboratory experiments on wave-driven sand transport processes. *Coastal Engineering*, 56(7), 726–732. Retrieved from <http://dx.doi.org/10.1016/j.coastaleng.2009.01.008> doi: 10.1016/j.coastaleng.2009.01.008
- Van der Zanden, J. (2016). *Sand Transport Processes in the Surf and Swash Zones* (Unpublished doctoral dissertation).
- Van der Zanden, J., Van der A, D. A., Hurther, D., Cáceres, I., O'Donoghue, T., Hulscher, S. J., & Ribberink, J. S. (2017). Bedload and suspended load contributions to breaker bar morphodynamics. *Coastal Engineering*, 129(September), 74–92. doi: 10.1016/j.coastaleng.2017.09.005
- Van Rijn, L. C. (1993). *Principles of Sediment Transport in Rivers, Estuaries and Coastal Seas*. doi: 10.1002/9781444308785
- Van Rijn, L. C. (2007a). Unified View of Sediment Transport by Currents and Waves. I: Initiation of Motion, Bed Roughness, and Bed-Load Transport. *Journal of Hydraulic Engineering*, 133(6), 649–667. Retrieved from [http://ascelibrary.org/doi/10.1061/\(ASCE\)0733-9429\(2007\)133:7\(776\)](http://ascelibrary.org/doi/10.1061/(ASCE)0733-9429(2007)133:7(776)) doi: 10.1061/(ASCE)0733-9429(2007)133:7(776)
- Van Rijn, L. C. (2007b). Unified View of Sediment Transport by Currents and Waves. II: Suspended Transport. *Journal of Hydraulic Engineering*, 133(7), 668–689. Retrieved from [http://ascelibrary.org/doi/10.1061/\(ASCE\)0733-9429\(2007\)133:7\(776\)](http://ascelibrary.org/doi/10.1061/(ASCE)0733-9429(2007)133:7(776)) doi: 10.1061/(ASCE)0733-9429(2007)133:7(776)
- Van Rijn, L. C. (2007c). Unified View of Sediment Transport by Currents and Waves. III: Graded Beds. *Journal of Hydraulic Engineering*, 133(7), 761–775. Retrieved from [http://ascelibrary.org/doi/10.1061/\(ASCE\)0733-9429\(2007\)133:7\(776\)](http://ascelibrary.org/doi/10.1061/(ASCE)0733-9429(2007)133:7(776)) doi: 10.1061/(ASCE)0733-9429(2007)133:7(776)
- Van Rijn, L. C., Walstra, D., & van Ormondt, M. (2004). Description of TRANSPOR2004 and Implementation in Delft3D-ONLINE. (November), 77.
- Van Rijn, L. C., Walstra, D. J., Grasmeijer, B., Sutherland, J., Pan, S., & Sierra, J. P. (2003). The predictability of cross-shore bed evolution of sandy beaches at the time scale of storms and seasons using process-based profile models. *Coastal Engineering*, 47(3), 295–327. doi: 10.1016/S0378-3839(02)00120-5
- Van Rijn, L. C., & Wijnberg, K. M. (1996). One-dimensional modelling of individual waves and wave-induced longshore currents in the surf zone. *Coastal Engineering*, 28(1-4), 121–145. doi: 10.1016/0378-3839(96)00014-2
- Walstra, D., van Ormondt, M., & Roelvink, J. (2004). *Shoreface Nourishment Scenarios* (Tech. Rep.).
- Wentworth, C. K. (1922). A Scale of Grade and Class Terms for Clastic Sediments. *The journal of geology*.



VAN RIJN EQUATIONS

A.1 SEDIMENT BED CLASSIFICATION

$$\begin{aligned}d_{gravel} &= 2000\mu m && \text{(diameter of gravel)} \\d_{sand} &= 62\mu m && \text{(diameter of sand)} \\d_{silt} &= 32\mu m && \text{(diameter of silt)} \\d_{cs} &= 8\mu m && \text{(diameter of clay and silt)}\end{aligned}\tag{A.1}$$

A.2 CURRENT RELATED BED ROUGHNESS

A.2.1 RIPPLES

The current-related roughness due to ripples is given by:

$$\begin{aligned}k_{s,c,r} &= 150f_{cs}d_{rep} && \text{for } \psi \leq 50 \\k_{s,c,r} &= 20f_{cs}d_{rep} && \text{for } \psi > 250 \\k_{s,c,r} &= (182.5 - 0.652\psi)f_{cs}d_{rep} && \text{for } 50 < \psi \leq 250 \\k_{s,c,r} &= 20d_{silt} && \text{for } d_{rep} < d_{silt}\end{aligned}\tag{A.2}$$

with ψ the current-wave mobility parameter: $\psi = U_{wc}^2/[(s-1)gd_{rep}]$ where $U_{wc}^2 = U_w^2 + u_c^2$. U_w denotes the peak orbital velocity near the bed and u_c the depth-averaged current velocity. Furthermore $f_{cs} = (0.25d_{gravel}/d_{rep})^{1.5}$.

A.2.2 MEGA-RIPPLES

The current-related roughness due to mega-ripples is given by:

$$\begin{aligned}k_{s,c,mr} &= 0.0002f_{fs}\psi h && \text{for } \psi \leq 50 \\k_{s,c,mr} &= (0.011 - 0.0002\psi)f_{fs}h && \text{for } 50 < \psi \leq 550 \\k_{s,c,mr} &= 0.02 && \text{for } \psi > 550 \text{ and } d_{rep} \geq 1.5d_{sand} \\k_{s,c,mr} &= 200d_{rep} && \text{for } \psi > 550 \text{ and } d_{rep} < 1.5d_{sand} \\k_{s,c,mr} &= 0 && \text{for } d_{rep} < d_{silt}\end{aligned}\tag{A.3}$$

with $f_{fs} = (d_{rep}/1.5d_{sand})$ and $f_{fs} = 1$ for $d_{rep} \geq 1.5d_{sand}$ and $k_{s,c,mr,max} = 0.2$.

The coefficient related to the vertical structure of the velocity profile β is given by:

$$\beta = 0.25 \frac{[-1 + \ln(30h/k_{s,c})]^2}{[\ln(30a/k_{s,c})]^2}\tag{A.4}$$

A.3 BED-SHEAR STRESS

The bed-shear stress for current and waves is given by:

$$\tau'_b = \alpha_{cw} \mu_c \tau_{b,c} + \mu_w \tau_{b,w} \quad (\text{A.5})$$

with:

$$\alpha_{cw} = \left[\frac{\ln(30\delta_m/k_a)}{\ln(30\delta_m/k_{s,c})} \right]^2 \left[\frac{-1 + \ln(30h/k_{s,c})}{-1 + \ln(30h/k_a)} \right]^2 \quad (\text{A.6})$$

$$\alpha_{cw,max} = 1$$

$$\mu_c = f'_c / f_c \quad (\text{A.7})$$

$$\mu_w = 0.7 / D_{*,i} \quad (\text{A.8})$$

$$\mu_{w,min} = 0.14 \text{ for } D_{*,i} \geq 5$$

$$\mu_{w,max} = 0.35 \text{ for } D_{*,i} \leq 2$$

$$\tau_{b,c} = 0.125 \rho_w f_c (U_{net})^2 \quad (\text{A.9})$$

$$\tau_{b,w} = 0.25 \rho_w f_w (U_w)^2 \quad (\text{A.10})$$

$$(\text{A.11})$$

where δ_m is the thickness of the effective fluid mixing layer, h the water depth, U_{net} the net current, U_w the maximum orbital velocity near the bottom and ka the apparent roughness.

B

SANTOSS EQUATIONS

B.1 BED-SHEAR STRESS

The current-related and wave-related bed roughness are given by Ribberink (1998):

$$k_{s,\delta} = \max\{3d_{90}, d_{rep}[\mu + 6(\langle|\theta|\rangle - 1)]\} + 0.4\eta^2/\lambda \quad (\text{B.1})$$

$$k_{s,w} = \max\{d_{rep}, d_{rep}[\mu + 6(\langle|\theta|\rangle - 1)]\} + 0.4\eta^2/\lambda \quad (\text{B.2})$$

with

$$\mu = \begin{cases} 6 & \text{if } d_{rep} \leq 0.15\text{mm} \\ 6 - \frac{5(d_{rep}-0.15)}{(0.20-0.15)} & \text{if } 0.15\text{mm} < d_{rep} < 0.20\text{mm} \\ 1 & \text{if } d_{rep} \geq 0.20\text{mm} \end{cases} \quad (\text{B.3})$$

and

$$\langle|\theta|\rangle = \frac{\frac{1}{2}f_{\delta}|U_{net}|^2}{(s-1)gd_{rep}} + \frac{\frac{1}{2}f_w U_w^2}{(s-1)gd_{rep}} \quad (\text{B.4})$$

C.1 GRIDS

The staggered grid as used in DELFT3D to solve the equations is shown in Figure C.1 and the vertical grid with the different sigma layers is shown in Figure C.2.

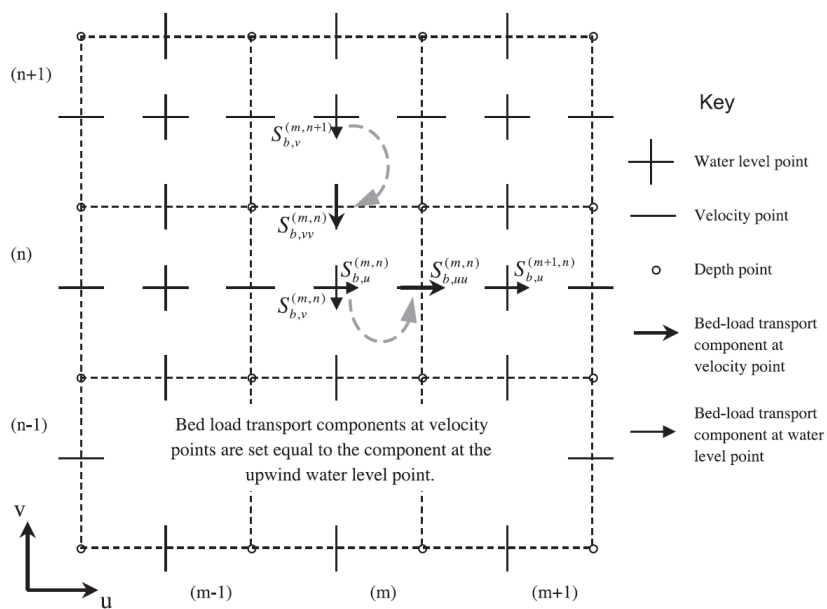


Figure C.1: Staggered grid to solve equations as used in DELFT3D-FLOW. (Deltares, 2018)

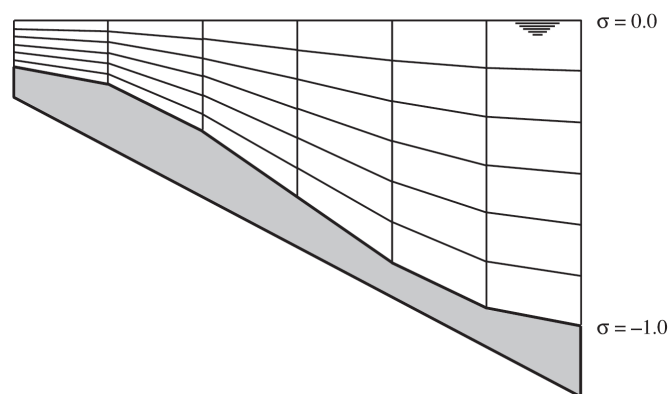


Figure C.2: Vertical grid with 6 σ layers of equal thickness. (Lesser et al., 2004)

C.2 SYSTEM OF EQUATIONS

The set of equations used to solve the shallow-water equations are named below. It comprises the hydrostatic pressure assumption, continuity and horizontal momentum equations, and turbulence closure model.

C.2.1 HYDROSTATIC PRESSURE ASSUMPTION

As shallow water is assumed, the vertical momentum equation reduces to the hydrostatic pressure equation. This excludes vertical acceleration due to buoyancy effects or variations in the bottom topography. The hydrostatic pressure equation is given by:

$$\frac{\partial P}{\partial \sigma} = -\rho gh \quad (\text{C.1})$$

where the left term indicates the change of pressure over depth, and the right term the hydrostatic pressure at a given water depth.

C.2.2 CONTINUITY EQUATION

The depth-averaged continuity equation for incompressible fluids is given by:

$$\frac{\partial \zeta}{\partial t} + \frac{\partial [h\bar{U}]}{\partial x} + \frac{\partial [h\bar{V}]}{\partial y} = S \quad (\text{C.2})$$

where the first term describes the change of the free surface elevation relative to the undisturbed water level over time, the second and third term the flow in the x and y direction and the term on the right implies whether there is any withdrawal or discharge of water.

C.2.3 HORIZONTAL MOMENTUM EQUATION

The horizontal momentum equations for incompressible fluids are given by:

$$\begin{aligned} \frac{\partial U}{\partial t} + U \frac{\partial U}{\partial x} + v \frac{\partial U}{\partial y} + \frac{\omega}{h} \frac{\partial U}{\partial \sigma} - fV &= -\frac{1}{\rho_0} P_x + F_x + M_x + \frac{1}{h^2} \frac{\partial}{\partial \sigma} \left(v_V \frac{\partial u}{\partial \sigma} \right) \\ \frac{\partial V}{\partial t} + U \frac{\partial V}{\partial x} + V \frac{\partial V}{\partial y} + \frac{\omega}{h} \frac{\partial V}{\partial \sigma} - fU &= -\frac{1}{\rho_0} P_y + F_y + M_y + \frac{1}{h^2} \frac{\partial}{\partial \sigma} \left(v_V \frac{\partial v}{\partial \sigma} \right) \end{aligned} \quad (\text{C.3})$$

Where the first four terms on the left describe the accelerations over space and time, and the fifth term the Coriolis force. The first term on the right is the horizontal pressure term given by the Boussinesq approximations, the second term the Reynold's stresses, the third term represents the contributions due to external source and sinks of momentum and the last term the turbulence closure model.

C.2.4 TURBULENCE CLOSURE MODELS

Within DELFT3D there are four turbulence closure models that can determine v_V (used in Eq. C.3) and D_V (used in Eq. 2.37), namely:

1. Constant coefficient.
2. Algebraic Eddy viscosity closure Model (AEM).
3. $k - L$ turbulence closure model.
4. $k - \epsilon$ turbulence closure model.

The models are different in their approach of the turbulent kinetic energy k , dissipation rate of turbulent kinetic energy ϵ and/or the mixing length L (Deltares, 2018).

C.2.5 CONCENTRATION PROFILE (ROUSE PROFILE)

The concentration per fraction is given by:

$$c^{(l)} = c_a^{(l)} \left[\frac{a(h-z)}{z(h-a)} \right]^{A^{(l)}}, \quad (\text{C.4})$$

with $c^{(l)}$ the concentration of sediment fraction (l), $c_a^{(l)}$ the reference concentration of sediment fraction (l), a the reference height, h the water depth and z the elevation above the bed. $A^{(l)}$ is the Rouse number given by:

$$A^{(l)} = \frac{\ln \left(\frac{c_{kmx}}{c_a} \right)}{\ln \left(\frac{a(h-z_{kmx})}{z_{kmx}(h-a)} \right)}, \quad (\text{C.5})$$

with c_{kmx} the concentration at the kmx layer and z_{kmx} the elevation of the kmx layer.

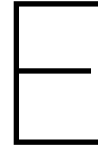
D

SINBAD EXPERIMENTS

The sieving data as measured by the CIEM lab is shown in Table D.1.

Table D.1: Sieve data of sediment used in SINBAD experiments.

Grain size [mm]	[%]	Cumulative [%]
0.710	0.010	0.010
0.595	0.014	0.024
0.500	0.336	0.360
0.350	13.093	13.453
0.300	33.723	47.175
0.210	27.308	74.484
0.149	18.384	92.867
0.125	6.580	99.447
0.105	0.372	99.819
0.088	0.121	99.940
0.063	0.025	99.965
Rest	0.035	100.000



PERFORMANCE CRITERIA

The performance of the models are assessed by the Bias, Root Mean Square Error (RMSE), coefficient of determination (r^2) and Factor 2 interval.

BIAS

The Bias shows whether the model has a tendency to over- or underestimates the sediment transport and is given by:

$$Bias = \frac{q_{mod} - q_{meas}}{q_{meas}} * 100 \quad (E.1)$$

The Bias is expressed in % where a negative value implies underestimation and a positive value overestimation.

ROOT MEAN SQUARE ERROR

The Root Mean Square Error is an often used test to determine the accuracy of a model, and gives a relatively high weight to outliers and is qualified to reveal model performance differences (Chai & Draxler, 2014). The RMSE is expressed in the unit of the assessed data and is given by:

$$RMSE = \sqrt{\frac{\sum_{j=1}^N (q_{mod} - q_{meas})^2}{N}} \quad (E.2)$$

COEFFICIENT OF DETERMINATION (r^2)

r^2 is a dimensionless criterion and expresses the variance between the observed and the modelled data. When $r^2 = 1$ the dependent variable can be predicted without error from the independent variable. It assesses how well a model can predict future outcomes. The equation is given by:

$$r^2 = \left(\frac{n(\sum q_{mod}q_{meas}) - (\sum q_{mod})(\sum q_{meas})}{\sqrt{[n \sum q_{mod}^2 - (\sum q_{mod})^2][n \sum q_{meas}^2 - (\sum q_{meas})^2]}} \right)^2 \quad (E.3)$$

FACTOR 2 INTERVAL

This criterion assesses how many of the modelled net transport rates are located within a Factor 2 of the measured net transport rates and is expressed in %.

VALIDATION VAN RIJN MODEL FOR BED-LOAD TRANSPORT

F.1 FORTRAN CODE

In the paper of Van Rijn, different methods are introduced to model graded sediment transport. The measured bed-load transport rates for the P9F case carried out by Hassan (2003) (Table 2.1) are used to validate the different calculation methods, which results are presented in Figure F.1. The subscript A or B presented on the x-axis denotes the choice of the dimensionless bed-shear stress parameter T_j , where the grain related roughness (k_s) is either based on d_j or d_{90} .

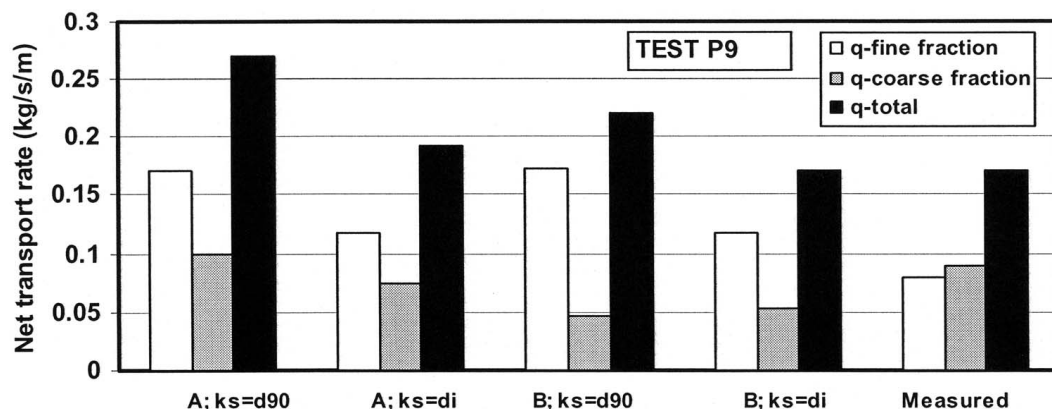


Figure F.1: Comparison of the modelled and measured net transport rates as computed by Van Rijn (2007c) for experiment P9F as carried out by Hassan (2003) in a flow tunnel. A or B depicts the method used to calculate the dimensionless bed-shear stress parameter and 90 or i normative grain roughness based on respectively d_{90} or d_i

All the modelled net transport rates show higher values for the fine fraction than for the coarse fraction. This can be attributed to the absence of formulae for phase lag effects in the model for bed-load transport. These effects are accounted for by the formulations regarding suspended sediment transport by Van Rijn (2007b), which are present within the DELFT3D model. The absence of these formulations for suspended sediment transport within the current bed-load model seems to lead to systematic overestimation of the transport rates of the fine fraction.

F.2 COMPARISON FORTRAN AND MATLAB

The existing Fortran code is converted into a MATLAB code, sticking as much to the code as possible. However, Van Rijn uses some tweaking parameters in the Fortran code to enhance its performance, for example when an extra parameter is added to the dimensionless bed-shear stress parameter, leading to adapted critical bed-shear stresses. For the transition between Fortran and MATLAB the decision has been made to exclude this parameter and to stick to the existing documentation on the code.

F.2.1 STREAMING

Additionally, Van Rijn has included streaming within his model which is present in case of transverse waves. As the experiments have taken place in an oscillatory flow tunnel, these types of waves are absent and this factor must thus be excluded from the formulations.

F.2.2 COMPARISON

Including this streaming effect in the MATLAB model should yield results comparable to that of the Fortran code. Both models are compared using the same input as presented in Table F.1, which values are based on the P9F experiment carried out by Hassan (2003). All input parameters have fixed values, except the wave height which is varied between a value of 0 till 3 meter with steps of 0.2 meter. The corresponding orbital velocities and bed-load transport rates are included in Table F.2. The transport rates obtained by the Fortran code and MATLAB code are plotted in Figure F.2a, where the solid line denotes the line of perfect fit.

Table F.1: Input parameters comparison Fortran code and MATLAB script

Parameter	Value	Unit
Water depth	2.5	m
Wave period	6.5	s
Wavelength	30.9	m
Wave height	[0:0.2:3]	m
Number of fractions	1	-
D_{10}	0.16	mm
D_{50}	0.24	mm
D_{90}	0.99	mm
Temperature	15	°C
Salinity	0	‰

Table F.2: Input values for the significant wave height (H_s) for validation of the MATLAB script with the Fortran code. U_{bw} , U_{bwf} , U_{wbw} and U_{bwr} respectively denote the peak, forward, backward and representative orbital velocity.

H_s (m)	U_{bw} (m/s)	U_{bwf} (m/s)	U_{wbw} (m/s)	U_{bwr} (m/s)	q_b ($\times 10^{-6} m^2/s$)	
					Fortran	MATLAB
0.0	0.00	0.00	0.00	0.00	0.00	0.00
0.2	0.18	0.20	0.16	0.18	0.10	0.10
0.4	0.36	0.40	0.28	0.35	1.18	1.19
0.6	0.55	0.61	0.38	0.52	4.02	4.21
0.8	0.73	0.79	0.48	0.67	9.65	10.78
1.0	0.91	0.96	0.57	0.81	19.63	24.69
1.2	1.09	1.12	0.65	0.94	37.09	38.92
1.4	1.28	1.26	0.72	1.06	52.57	55.83
1.6	1.46	1.38	0.79	1.16	69.47	74.96
1.8	1.64	1.49	0.84	1.25	86.87	94.99
2.0	0.18	1.59	0.89	1.33	103.74	115.28
2.2	2.00	1.66	0.93	1.39	119.06	134.41
2.4	2.19	1.73	0.97	1.45	131.92	151.22
2.6	2.37	1.77	0.99	1.49	141.51	165.19
2.8	2.55	1.81	1.01	1.51	147.32	175.09
3.0	2.73	1.82	1.02	1.53	148.94	180.48

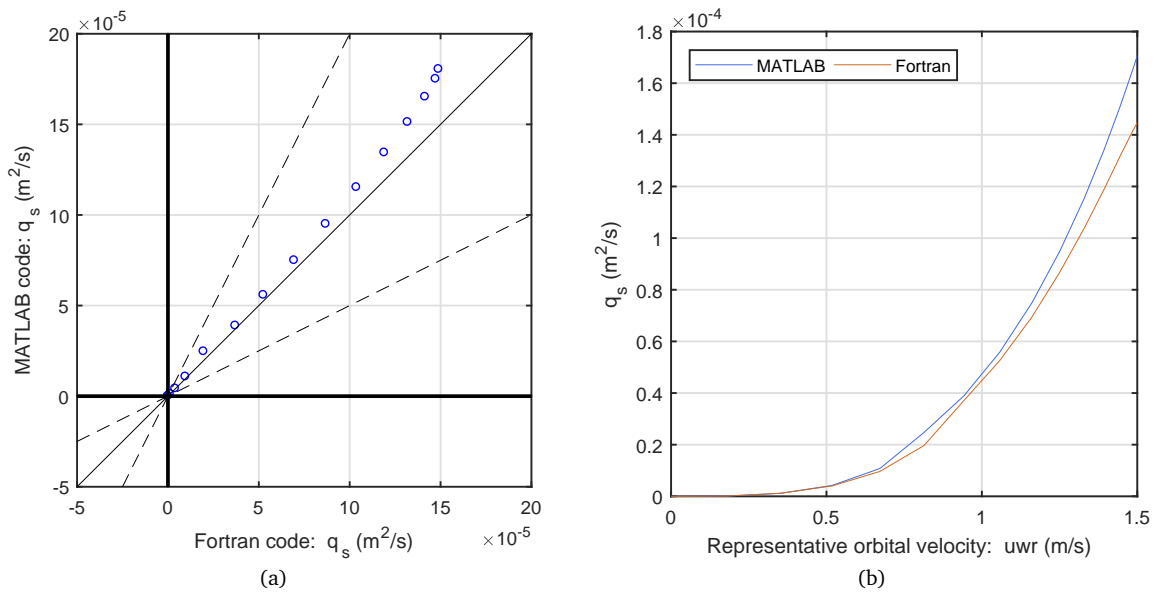


Figure F.2: Validation of the MATLAB code, using the original TR2004 Fortran code. Comparison by (a) using a line of perfect fit and (b) plotting the bed-load transport rates as function of the representative orbital velocity.

The results show that the transport rates from the MATLAB code overestimate the transport rates given by the Fortran code. This may be attributed to tweaking parameters used by Van Rijn in the Fortran code to enhance the models performance, which are absent in the MATLAB code. Especially

when the significant wave height and thus the orbital velocities are larger, the MATLAB code yields relatively higher transport rates than the Fortran code. Nevertheless, as shown in the previous chapter with the validation of the SANTOSS model, the transport rates hardly ever exceed $10 \cdot 10^{-5} m/s$, and is not expected to do so either for the formulations by Van Rijn. In Figure F.2b the net bed-load transport is plotted as function of the representative orbital velocity. The actual representative orbital velocity for this particular case (P9F, Table 2.1) is $1.32 m/s$, with a transport rate of $10 - 11 \cdot 10^{-5} m^2/s$.

F.3 MATLAB RESULTS

As streaming is not present within oscillatory flow tunnels, this term is now excluded from the model and set to 0 m/s, resulting in the transport rates presented in Figure F.3.

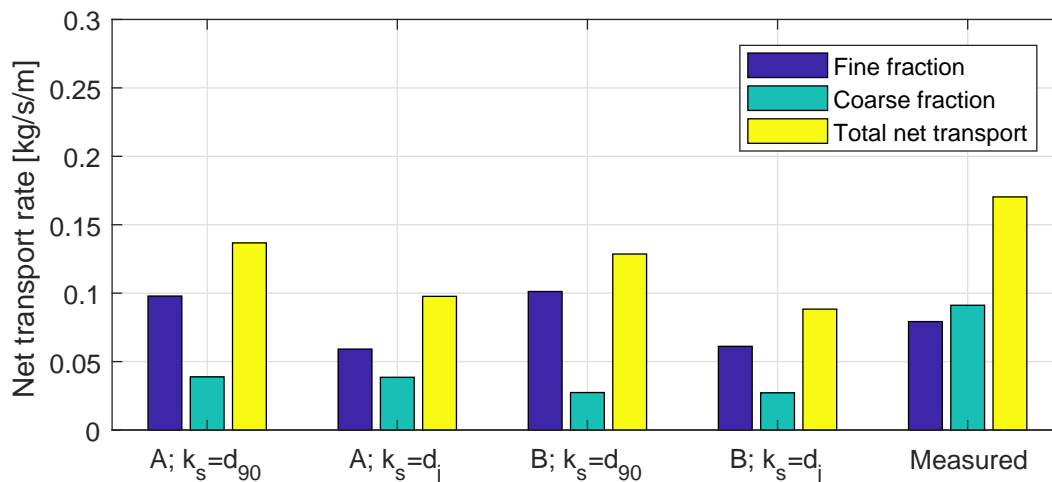


Figure F.3: Comparison of the modelled and measured net transport rates as computed using the formulation by Van Rijn (2007c) for experiment P9F as carried out by Hassan (2003) in a flow tunnel. A or B depicts the method used to calculate the dimensionless bed-shear stress parameter and 90 or i normative grain roughness based on respectively d_{90} or d_i

Due to the absence of streaming effects, the MATLAB model gives lower transport rates than the Fortran code. Nevertheless, Figure F.3 seems to catch the patterns as presented in Figure F.1, where the proportions between the transport rates of the different fractions show clear resemblances. The transport rates however, are systematically overestimated in the Fortran code and underestimated in the MATLAB model.

F.4 RESULTS FRACTIONS

The performance per fraction for the different model settings is presented in Table F.3.

Table F.3: Performance of the Van Rijn model when modelling the transport per fraction using different settings. The average value of the observed transport is $0.32 * 10^{-4} m^2/s$. F, M and C respectively denote the Fine, Medium and Coarse fraction, and $N = 19$.

Name	Setting No. #	Bias [%]			r^2 [-]			RMSE [$*10^{-4} m^2/s$]			Factor 2 [%]		
		F	M	C	F	M	C	F	M	C	F	M	C
Graded approach	1.1	-125	-37	-44	0.21	0.88	0.92	0.11	0.13	0.09	53	26	16
	1.2	-120	-29	-37	0.18	0.87	0.88	0.11	0.13	0.08	53	37	37
Grain roughness	3.1	-118	-26	-43	0.18	0.83	0.91	0.14	0.12	0.09	37	37	21
	3.2	-108	-15	-36	0.14	0.78	0.87	0.17	0.12	0.08	37	37	42
Hiding and exposure	4.1	-128	-41	-52	0.22	0.85	0.92	0.11	0.14	0.11	53	15	0
	4.2	-121	-28	-38	0.19	0.92	0.92	0.11	0.11	0.08	47	37	32
	4.3	-121	-28	-38	0.19	0.91	0.92	0.10	0.12	0.08	47	37	32
	4.4	-119	-30	-44	0.17	0.82	0.9	0.13	0.13	0.09	47	37	16
	4.5	-121	-28	-38	0.19	0.91	0.92	0.11	0.12	0.08	47	37	32
	4.6	-121	-28	-38	0.19	0.91	0.92	0.11	0.12	0.08	47	37	32

F.5 EFFECT OF ROUGHNESS SETTINGS USING $d_{rep} = d_{50}$

In the left sub-figure of figure F.4 and F.5, the default setting is shown, with in the right sub-figure the transport rates of a different grain roughness approach using $k_s = d_{90}$ instead of d_j .

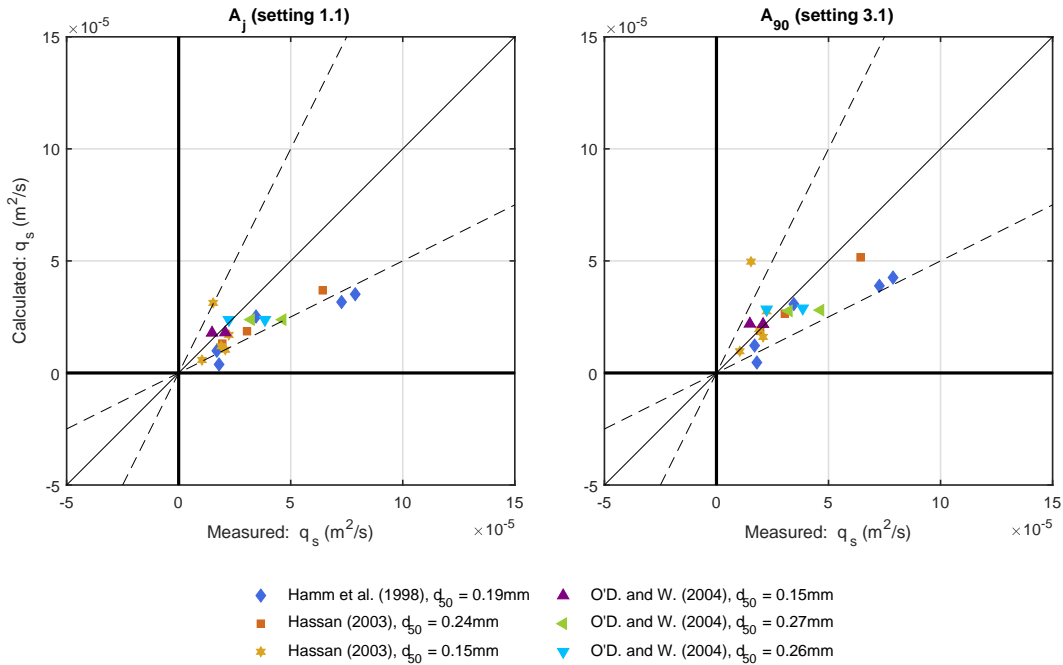


Figure F.4: Net total transport rates for different settings for the grain roughness, using $d_{rep} = d_{50}$. Setting 1.1 and 3.1 use method A for the dimensionless bed-shear stress parameter and d_j or d_{90} for the grain related roughness, hence A_j and A_{90} .

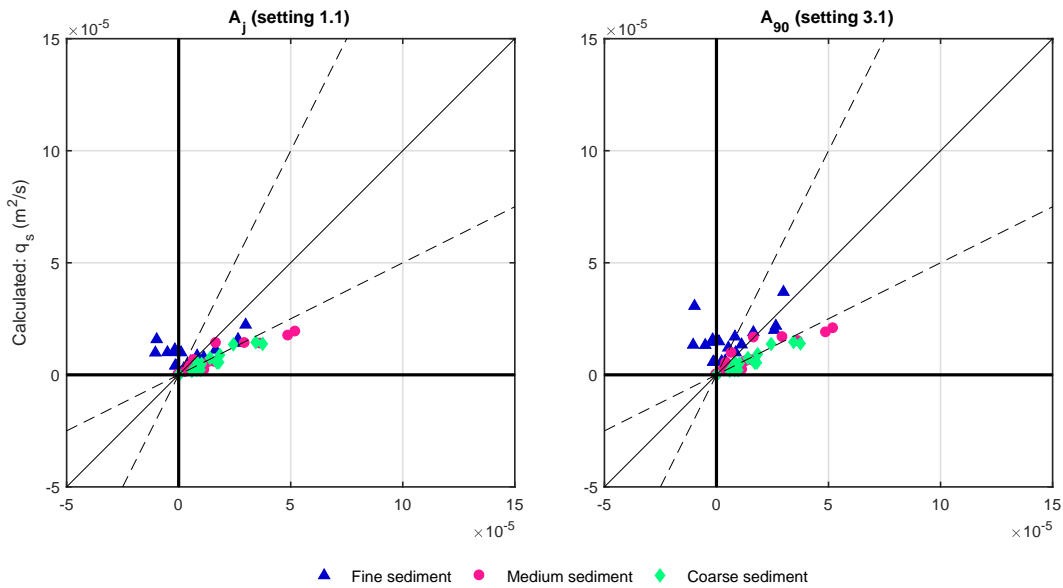


Figure F.5: Net transport rates per fraction for different settings for the grain roughness, using $d_{rep} = d_{50}$. Setting 1.1 and 3.1 use method A for the dimensionless bed-shear stress parameter and d_j or d_{90} for the grain related roughness, hence A_j and A_{90} .

F.6 SELECTIVE TRANSPORT USING $d_{rep} = d_{50}$

CORRECTION FACTOR FOR THE EFFECTIVE GRAIN-SHEAR STRESS AND HIDING AND EXPOSURE

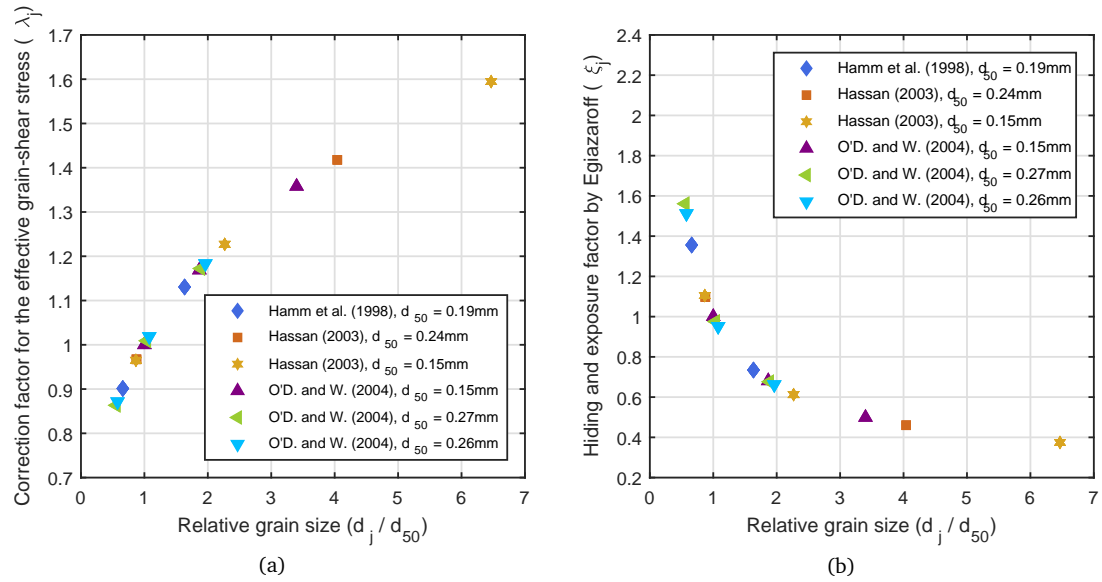


Figure F.6: (a) The correction factor for the effective grain-shear stress and (b) the hiding and exposure factor by Egiazaroff as function of the relative grain size. Please note that both y-axes use different limits.

BED-SHEAR STRESS

Figure F.7 shows the critical bed-shear stress, now distinguishing between the different datasets to gain a better understanding of the behaviour of the critical bed-shear stress.

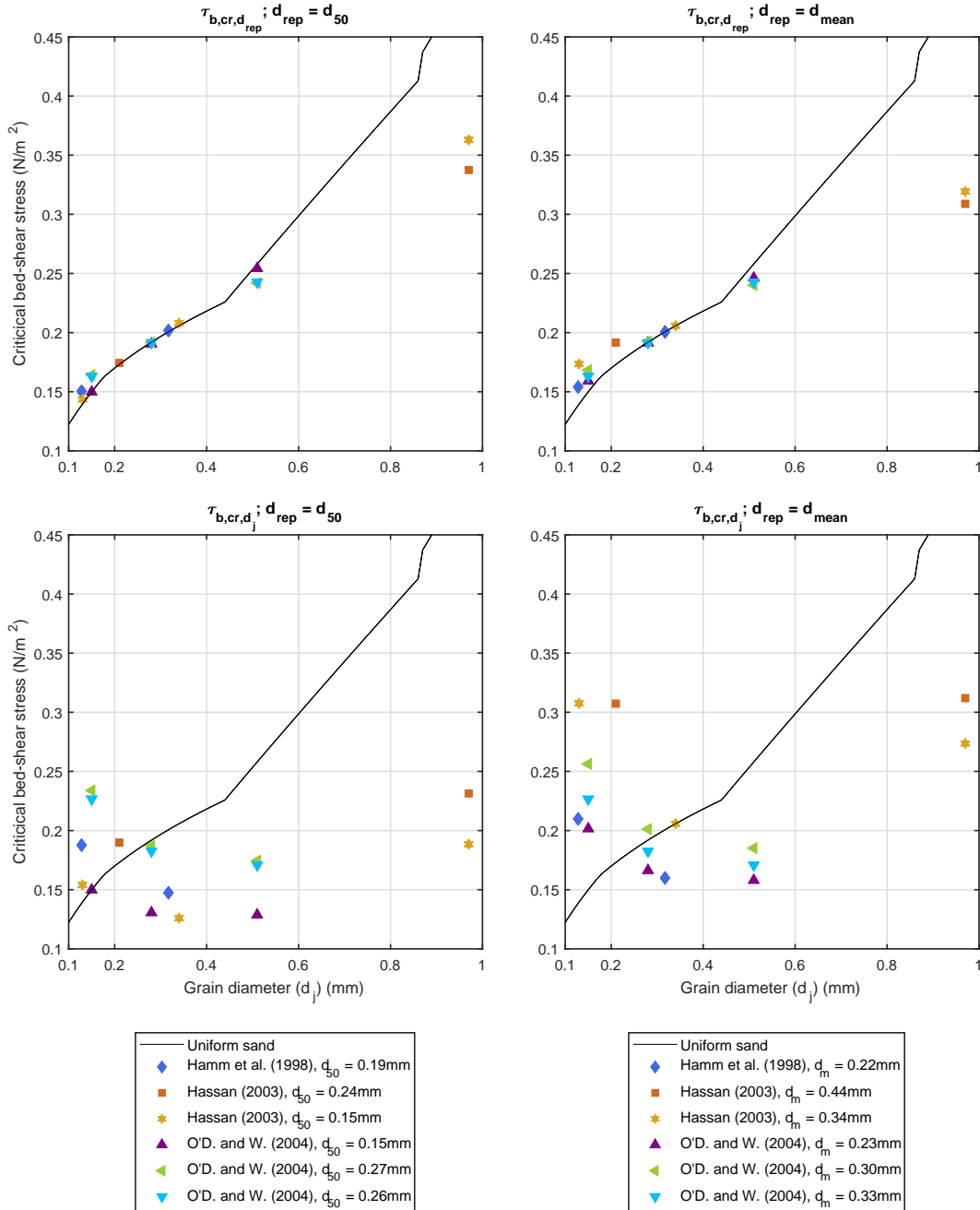


Figure F.7: Critical bed-shear stress times the hiding and exposure factor of Egiazaroff (Eq. 2.16), $\tau_{b,cr} * \xi_j$, as function of the grain diameter d_j . The top two figures comprise the d_{rep} approach respectively using $d_{rep} = d_{50}$ and $d_{rep} = d_{mean}$ as used in Method A and B (Eq. 2.18 and 2.19). The lower two figures depict the d_j approach respectively using $d_{rep} = d_{50}$ and $d_{rep} = d_{mean}$ as used in Method C (Eq. 2.20). The black line denotes the critical bed-shear stress for uniform sand.

The two upper sub-plots show that using a representative grain diameter of d_{mean} yields higher critical shear stresses for the fine sand and lower stresses for the coarse sand when compared to uni-

form sand. On the other side, comparing these two upper figures to the two in the bottom shows that the latter yield larger differences in critical stresses for the different representative grain diameters. Especially for the datasets by Hassan (2003), the overall critical bed-shear stresses are a lot higher using d_{mean} instead of d_{50} , though the other datasets also show a general increase.

EFFECT OF SELECTIVE TRANSPORT FOR $d_{rep} = d_{50}$

Figure F.8 and F.9 show the transport rates for all four different methods using a grain roughness of d_j .

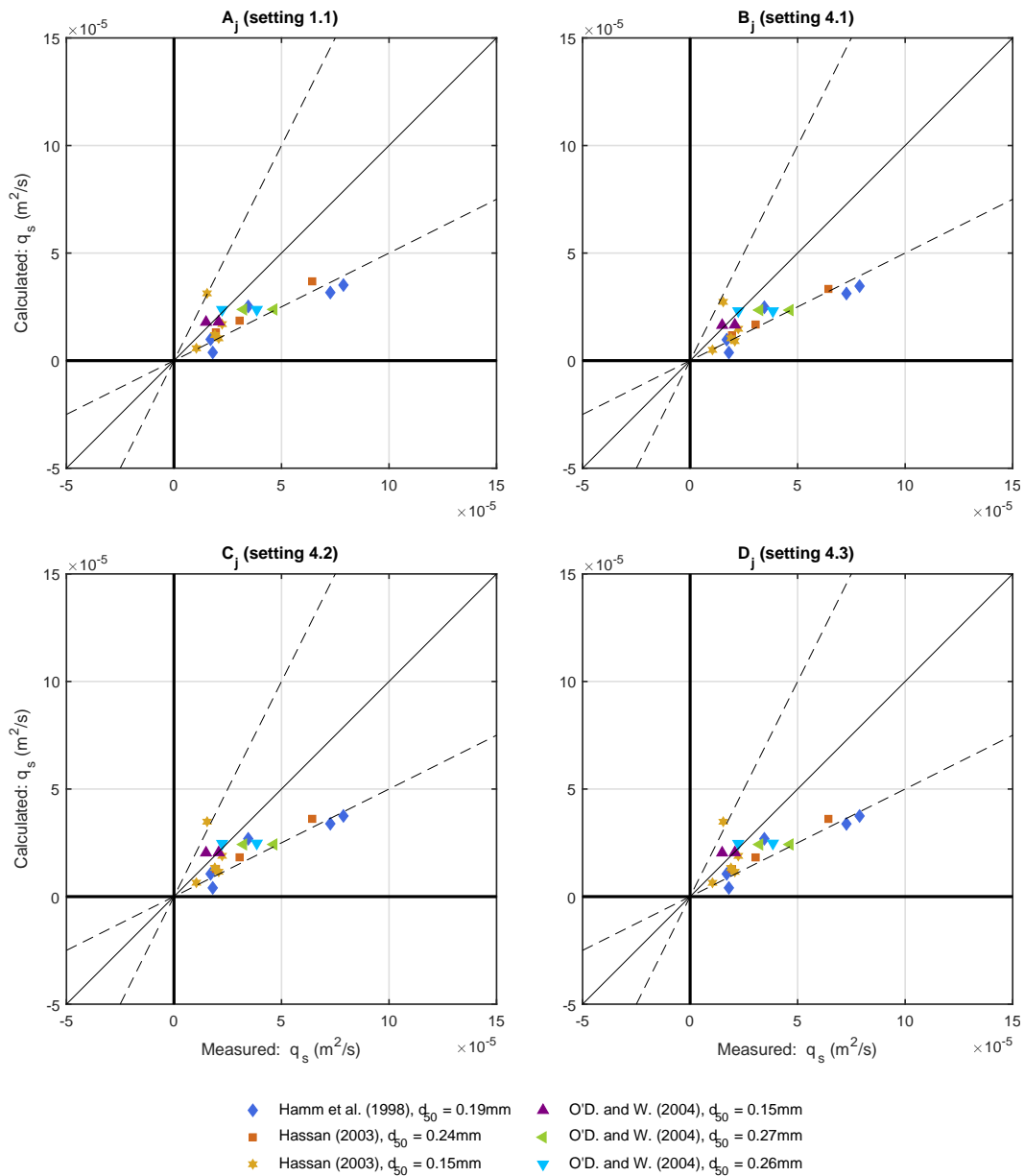


Figure F.8: Net total transport rates for different settings for grain roughness and critical bed-shear stress, using $d_{rep} = d_{50}$. Setting 1.1, 4.1, 4.2 and 4.3 respectively use method A, B, C or D for the dimensionless bed-shear stress parameter and d_j for the grain related roughness, hence A_j , B_j , C_j and D_j .

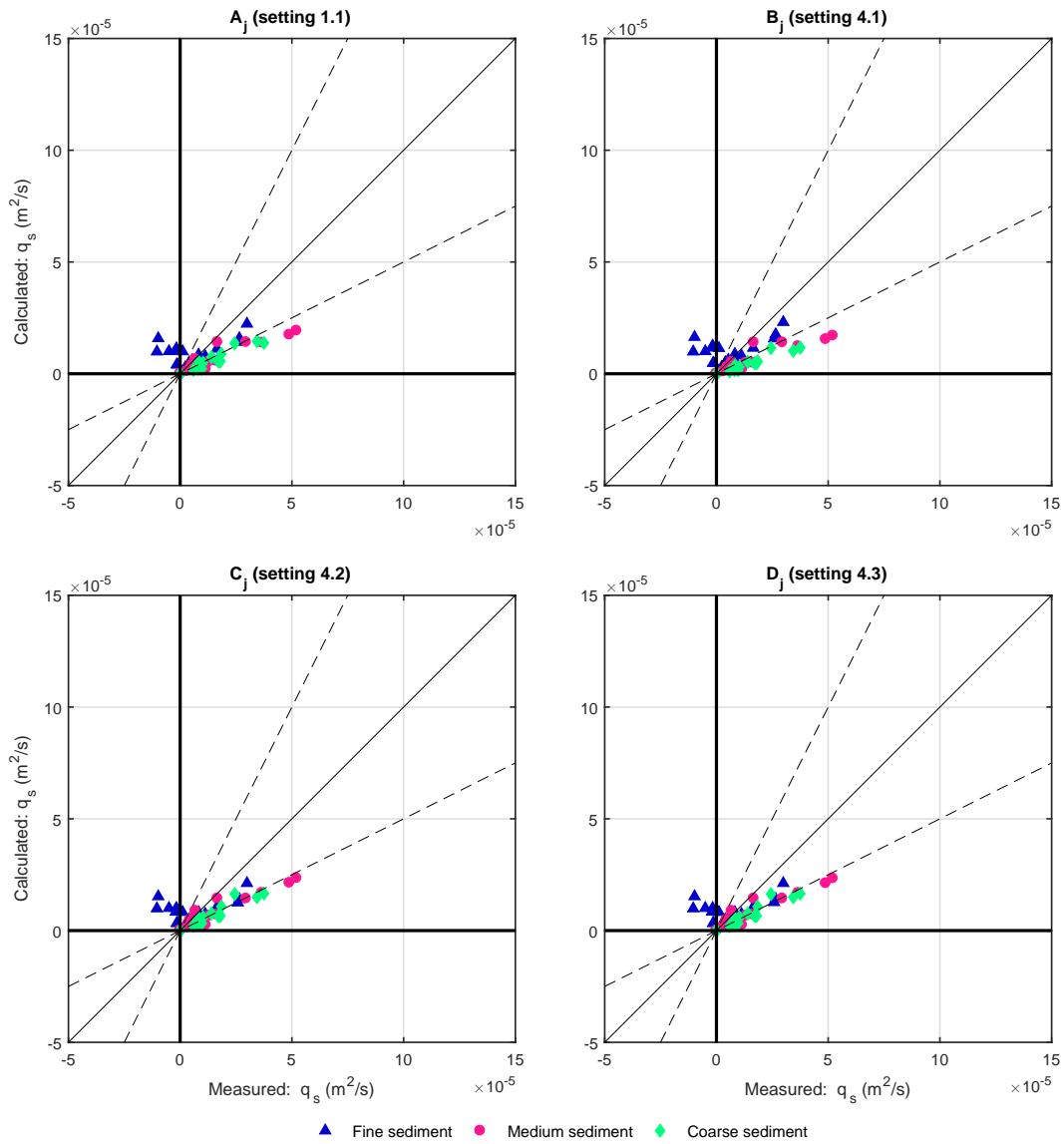


Figure F.9: Net transport rates per fraction for different settings for grain roughness and critical bed-shear stress, using $d_{rep} = d_{50}$. Setting 1.1, 4.1, 4.2 and 4.3 respectively use method A, B, C or D for the dimensionless bed-shear stress parameter and d_j for the grain related roughness, hence A_j , B_j , C_j and D_j .

G

VALIDATION SANTOSS MODEL FOR BED-LOAD TRANSPORT

G.1 RESULTS FRACTIONS

The performance per fraction for the different model settings is presented in Table G.1.

Table G.1: Performance of the SANTOSS model when modelling the transport per fraction using different settings. The average value of the observed transport is $0.32 * 10^{-4} m^2/s$. F, M and C respectively denote the Fine, Medium and Coarse fraction, and $N = 19$.

Name	Setting No. #	Bias [%]			r^2 [-]			RMSE [$*10^{-4} m^2/s$]			Factor 2 [%]		
		F	M	C	F	M	C	F	M	C	F	M	C
Graded approach	1.1	-48	-4	-20	0.70	0.89	0.89	0.10	0.08	0.06	42	68	68
	1.2	-71	7	-23	0.72	0.93	0.91	0.07	0.06	0.06	58	68	63
Wave-related roughness	3.1	-46	11	19	0.71	0.89	0.75	0.10	0.10	0.08	42	63	68
	3.2	-28	27	79	0.43	0.80	0.75	0.30	0.30	0.21	16	21	32
	3.3	-77	11	-2	0.71	0.93	0.86	0.06	0.08	0.05	68	68	74
Hiding and exposure	3.4	5	109	50	0.48	0.91	0.81	0.19	0.26	0.14	32	32	53
	4.1	-42	-18	-44	0.70	0.89	0.91	0.12	0.07	0.10	42	58	5
	4.2	-53	-3	-38	0.75	0.92	0.92	0.10	0.05	0.09	47	68	37

G.2 WAVE-RELATED ROUGHNESS

EFFECT OF THE WAVE-RELATED ROUGHNESS FOR $d_{rep} = d_{50}$

The total net transport rates and the transport rates per fraction for $d_{rep} = d_{50}$ are presented in Figure G.1 and G.2.

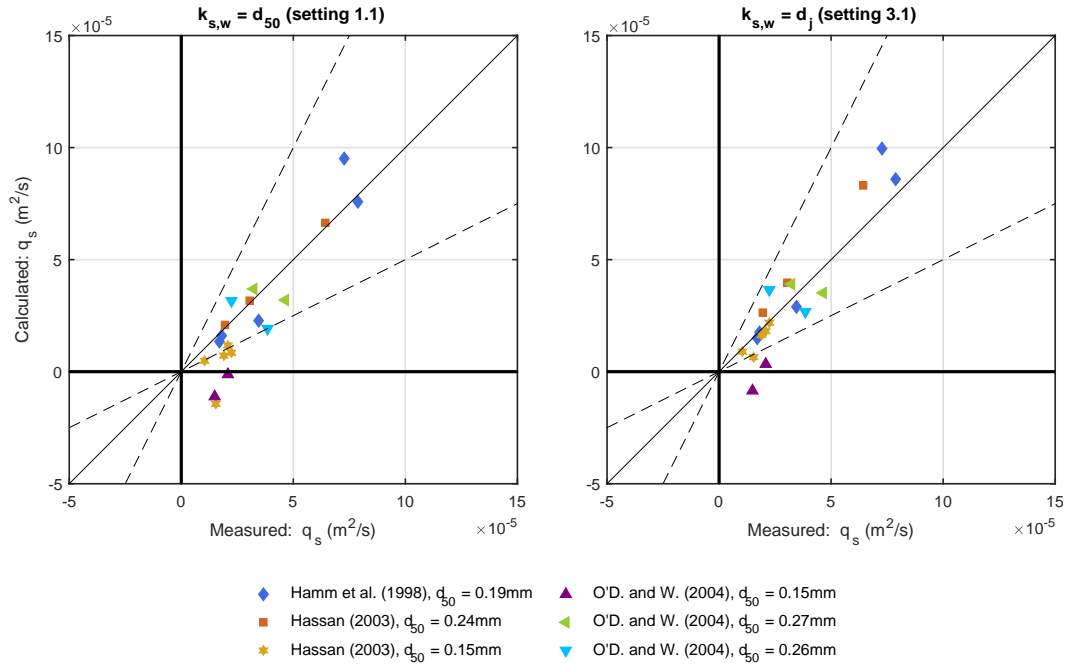


Figure G.1: Net total transport rates for different settings for the wave-related roughness, using $d_{rep} = d_{50}$

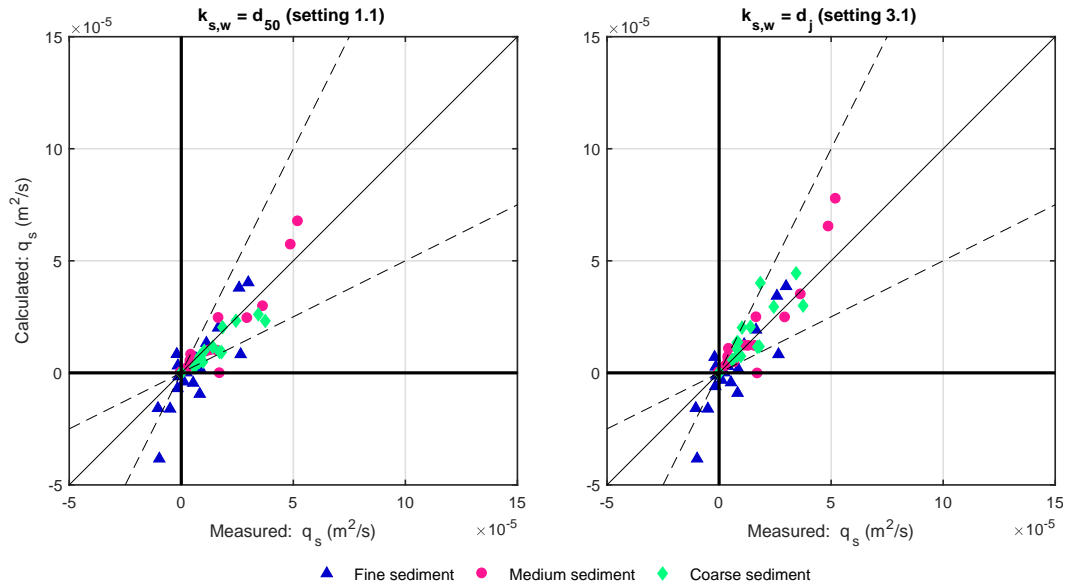


Figure G.2: Net transport rates per fraction for different settings for the wave-related roughness, using $d_{rep} = d_{50}$

The graded approach as used within the SANTOSS model (*setting 1.1*), is the left sub-figure in Figure G.1, denoted with $k_{s,w} = d_{50}$. Comparison with the setting where the wave-related friction

factor is based on d_j shows that the latter gives better results, as more data points are now located within the Factor 2 interval and for only one dataset the transport has been calculated in the wrong direction.

Investigation of the calculated transport per fraction shows that using a wave-related roughness of $k_{s,w} = \{d_j, \dots\}$ instead of $k_{s,w} = \{d_{50}, \dots\}$ gives higher transport rates for the medium and coarse fraction. This can be attributed to the use of d_j which is generally higher than d_{50} for the medium and coarse fraction, inducing higher values for the bed roughness. Regarding the fine fraction hardly any differences are visible as d_{50} often approaches d_j due to a skewed grain size distribution.

WAVE-RELATED ROUGHNESS OF $k_{s,w} = \{3d_{90}, \dots\}$

In Figure G.3 and G.4 the transport rates for a wave-related roughness of $3d_{90}$ are presented. Please note that the y axes all use the same limits for the sake of comparison, leading to one data point that is excluded from the right sub-figure in Figure G.3 from the dataset by Hamm et al. (1998), which gave a calculated net total transport rate of $15.04 \times 10^{-5} \text{ m}^2/\text{s}$ with an observed transport of $7.27 \times 10^{-5} \text{ m}^2/\text{s}$. The net total transport rates become very high for a wave-related roughness of $3d_{90}$ and there is large scatter in the transport rates per fraction, resulting in transport rates in the erroneous direction.

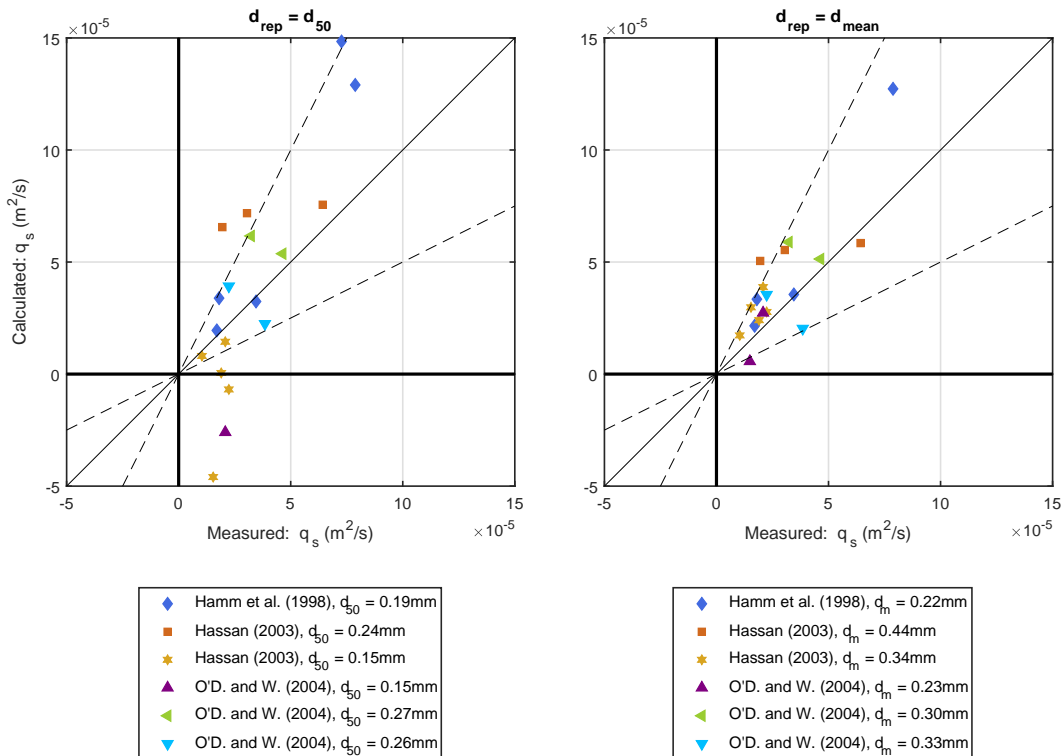


Figure G.3: Net total transport rates for a wave-related roughness of $3d_{90}$

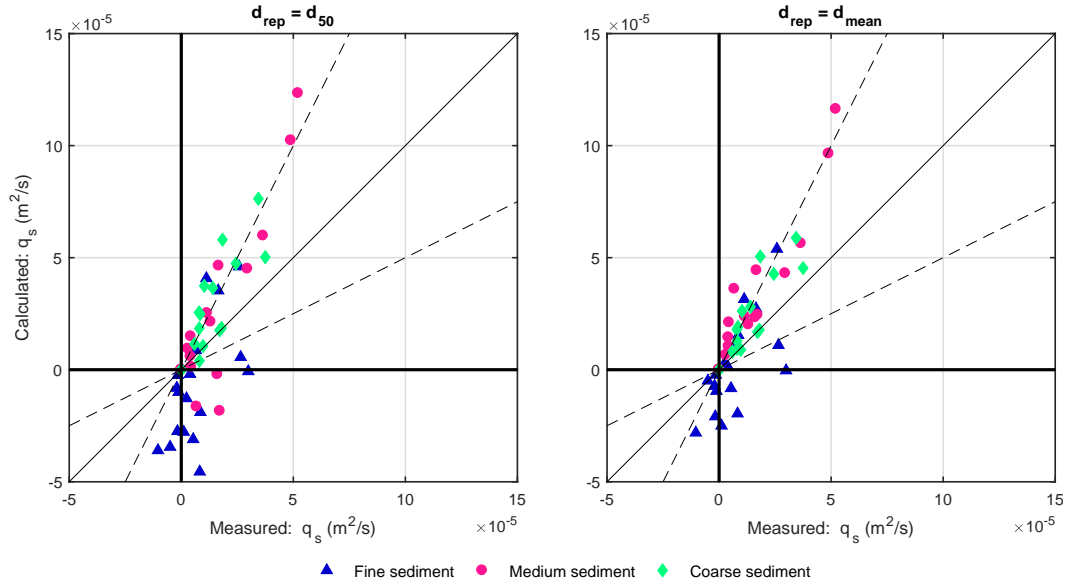


Figure G.4: Net transport rates per fraction for a wave-related roughness of $3d_{90}$

G.3 EFFECT OF SELECTIVE TRANSPORT FOR $d_{rep} = d_{50}$

In Figure G.5 the total net transport is presented with and without incorporation of λ_j . The overall calculated transport rates are a little higher when λ_j is included, especially for the dataset of Hassan (2003) with $d_{50} = 0.15mm$. Figure F.6a shows that λ_j almost reaches a value of 1.6 for a relative grain size of around 6.5. The experiments carried out by Hassan (2003) with code S#F, using $d_{50} = 0.15mm$ and $d_{coarse} = 0.97$, obtain these large values for λ_j , which affects the transport rates.

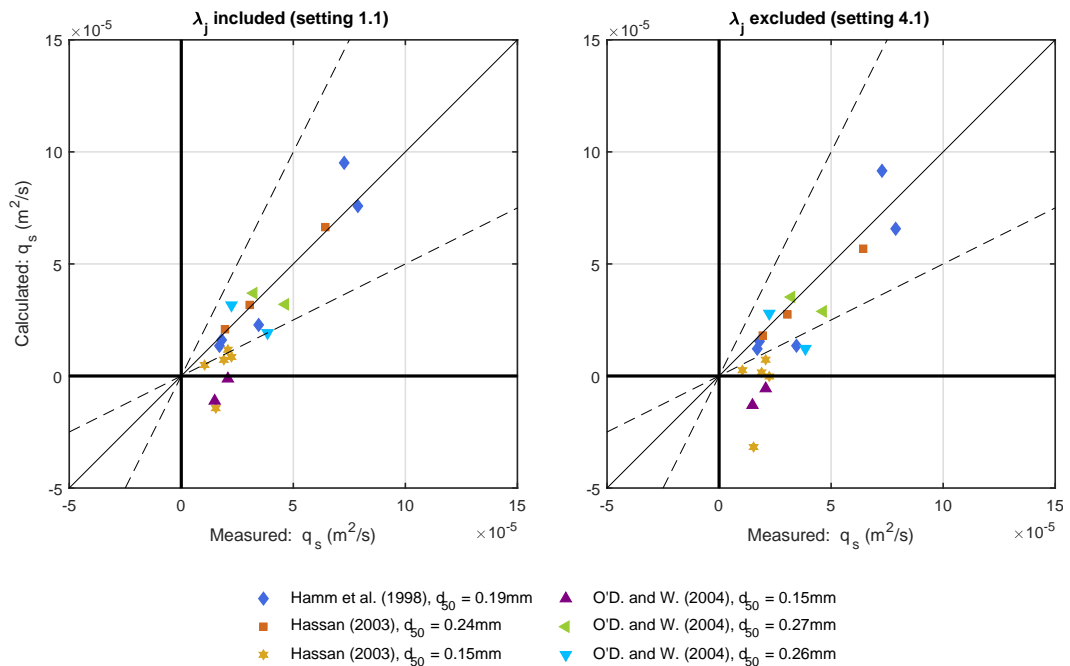


Figure G.5: Net total transport rates for both exclusion and inclusion of the correction factor for the effective grain-shear stress using $d_{rel} = d_{50}$.

Analysis of the transport rates per fraction (Fig. G.6) points out that mainly the medium and coarse sediment are affected by the different settings. However, only small differences are noticeable due to the relatively low values for d_{50} . This leads to values for λ_j which approach 1 for the fine sediment, which is almost equal to excluding the correction factor. Nevertheless, Figure ?? shows that correction factors for the coarser fractions reach values above 1.3, leading to higher transport rates for the medium and coarse fractions when hiding and exposure is included in the model.

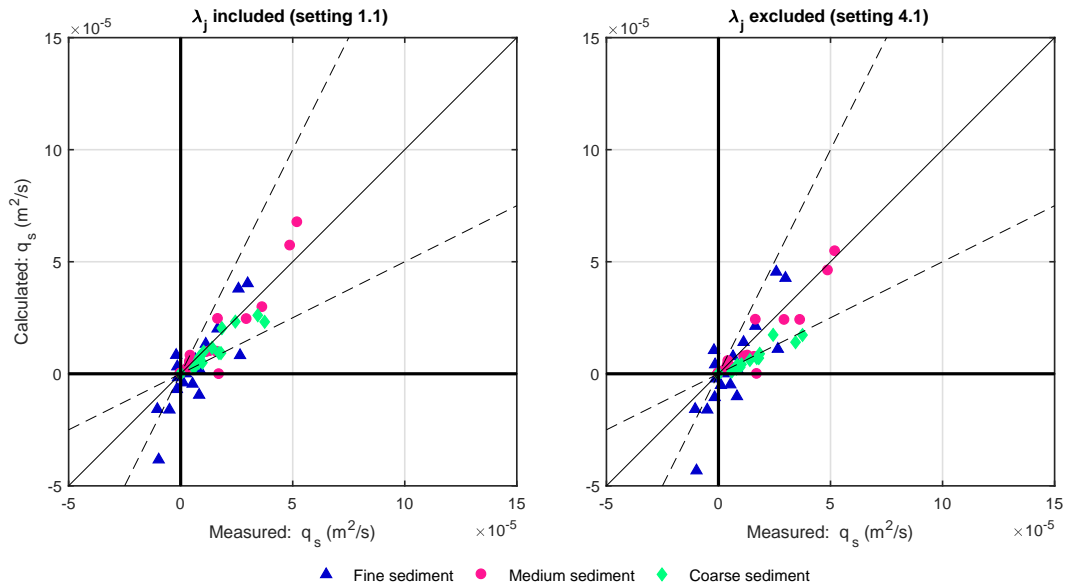
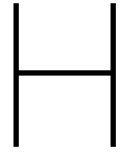


Figure G.6: Net transport rates per fraction for both exclusion and inclusion of the correction factor for the effective grain-shear stress using $d_{rel} = d_{50}$.



SENSITIVITY ANALYSIS DELFT3D

The sensitivity analysis has been carried out for the parameters given in Table H.1, according to the ranges proposed by Walstra, van Ormondt, and Roelvink (2004).

Table H.1: Overview of the performance of DELFT3D using different model settings, using the RMSE and Bias. With q_{sc} , q_{sw} , q_b and q_{tot} the current- and wave-related suspended sediment transport, bed-load transport and net total sediment transport. The bold parameter value is the default.

Parameter	Values	RMSE [$\cdot 10^{-5} \text{ m}^2/\text{s}$]				Bias [%]			
		q_{sc}	q_{sw}	q_b	q_{tot}	q_{sc}	q_{sw}	q_b	q_{tot}
FwFac	0	2.31	0.22	4.80	3.55	162	44	-69	-157
	0.5	2.29	0.19	4.30	2.23	-125	5	-63	-86
	1	2.42	0.19	4.17	1.85	-188	1	-62	-75
	1.5	2.50	0.19	4.12	1.76	-208	2	-63	-74
	2	2.53	0.19	4.07	1.70	-222	3	-63	-72
Sus	0	3.06	0.21	4.58	2.44	-100	34	-66	-78
	0.2	2.80	0.21	4.65	2.48	-73	3	-68	-89
	0.4	2.59	0.21	4.69	2.64	-29	38	-68	-102
	0.6	2.42	0.21	4.73	2.86	23	40	-68	-118
	0.8	2.32	0.21	4.77	3.22	93	42	-69	-139
	1	2.31	0.22	4.80	3.55	162	44	-69	-157
	1.2	2.41	0.22	4.83	3.98	243	44	-70	-183
Bed	0	2.31	0.22	4.57	3.31	162	44	-81	-153
	0.2	2.31	0.22	4.61	3.35	162	44	-79	-154
	0.4	2.31	0.22	4.66	3.40	162	44	-76	-154
	0.6	2.31	0.22	4.70	3.45	162	44	-74	-155
	0.8	2.31	0.22	4.75	3.50	162	44	-72	-156
	1	2.31	0.22	4.80	3.55	162	44	-69	-157
	1.2	2.31	0.22	4.85	3.60	162	44	-67	-158
SusW	0	2.31	0.25	4.80	3.77	162	-100	-69	-164
	0.2	2.31	0.22	4.80	3.73	162	-71	-69	-163
	0.4	2.31	0.21	4.80	3.68	162	-43	-69	-161
	0.6	2.31	0.20	4.80	3.64	162	-14	-69	-160
	0.8	2.31	0.20	4.80	3.68	162	15	-69	-159
	1	2.31	0.22	4.80	3.59	162	44	-69	-157
	1.2	2.31	0.24	4.80	3.5	162	72	-69	-156
BedW	0	2.31	0.22	4.63	3.41	162	44	-97	-152
	0.2	2.31	0.22	4.82	3.60	162	44	-84	-157
	0.4	2.31	0.22	4.82	3.59	162	44	-80	-157
	0.6	2.31	0.22	4.81	3.57	162	44	-77	-157
	0.8	2.31	0.22	4.81	3.56	162	44	-73	-157
	1	2.31	0.22	4.80	3.55	162	44	-69	-157
	1.2	2.31	0.22	4.80	3.54	162	44	-65	-157
Dicouv	1E-06	2.30	0.22	4.81	3.59	162	44	-70	-159
	1E-04	2.30	0.22	4.80	3.57	160	44	-70	-160
	0.01	2.49	0.22	4.79	3.81	156	43	-69	-164
	0.1	2.31	0.22	4.80	3.55	162	44	-69	-157
	1	4.25	0.21	4.77	5.31	661	42	-68	-231
	10	1.22	0.21	4.74	12.88	2190	38	-69	-1153
	100	3.05	0.21	4.74	31.56	6471	37	-68	-5630

In Table H.1 the default parameter value is in bold. This default value is fixed for every parameter, except for the parameter which is analysed. Only one parameter is being varied at a time. In the following paragraphs the definition of the parameters is given, together with the transport rates. Based on these figures and Table H.1, the optimum settings as shown in Table 5.1 are chosen. Only $FwFac=2$ clearly gives better results than the default setting. Therefore, only this parameter has been changed when comparing the default setting to the optimum setting.

FWFAC

$FwFac$ is the tuning parameter for the wave streaming and affects the vertical mixing distribution according to Van Rijn (Fig. H.1). A higher value for $FwFac$ gives positive total transport rates before $x \approx 52.5\text{m}$, but decreases the magnitude of the transport in the negative direction after this point.

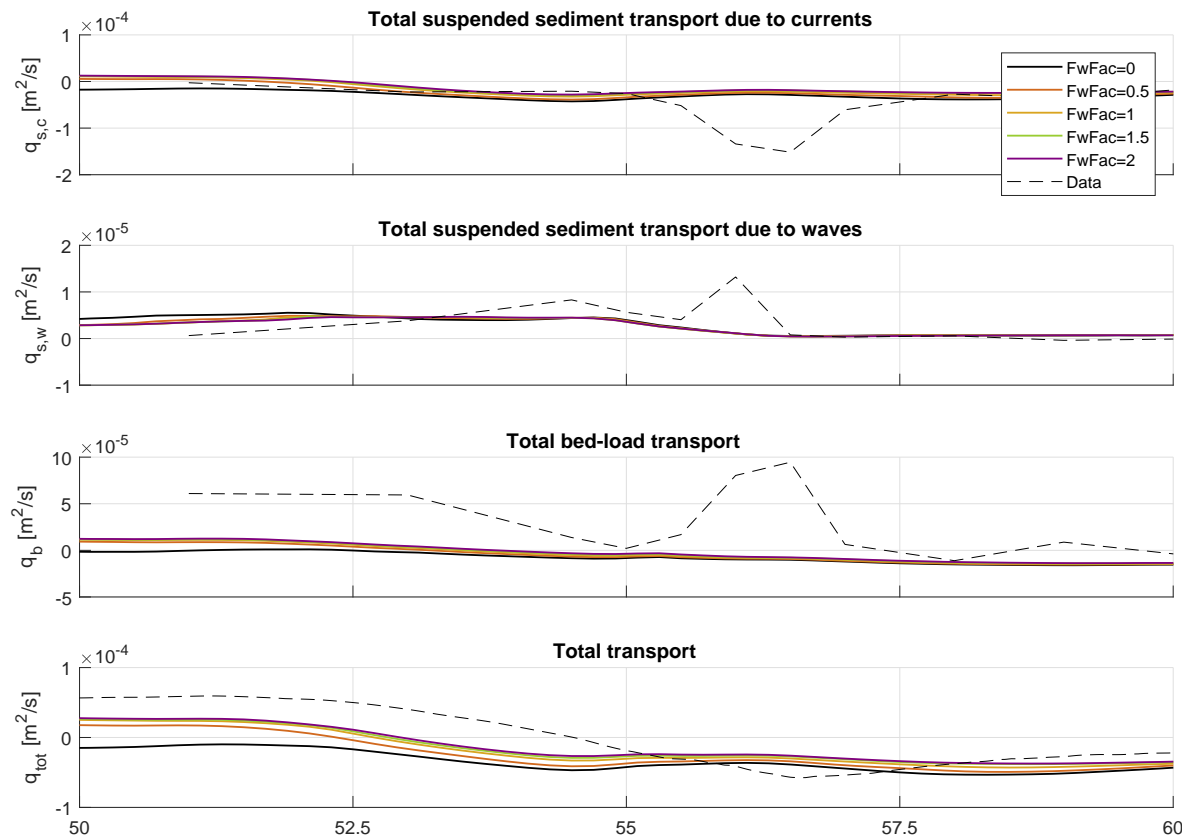


Figure H.1: Sediment transport rates using varying values for $FwFac$ as presented in Table H.1.

Sus

Sus is the current-related suspended sediment transport factor and is a multiplication factor for suspended sediment reference concentration (Fig. H.2). Higher values for *Sus* give higher suspended sediment transport rates, but the peak at $x \approx 56.5\text{m}$ is still not modelled accurately.

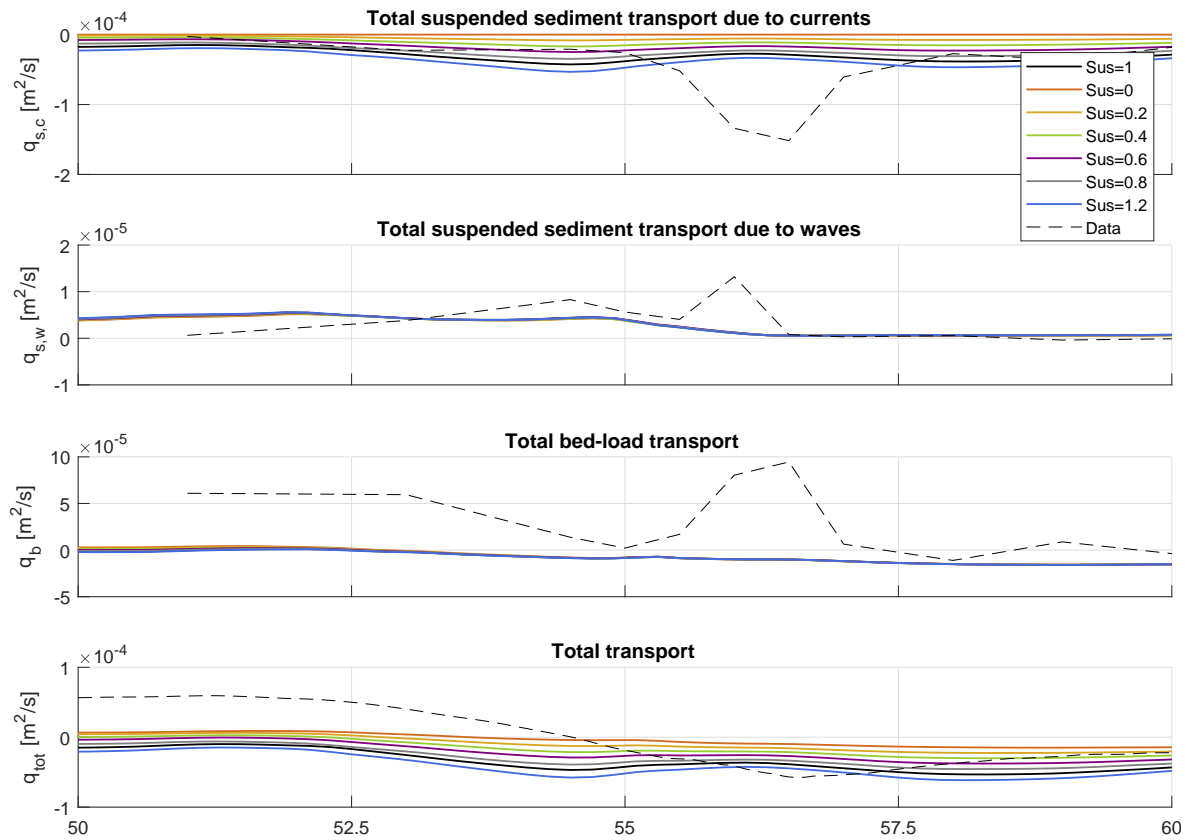


Figure H.2: Sediment transport rates using varying values for *Sus* as presented in Table H.1.

BED

Bed is the current-related bedload transport factor and is a multiplication factor for bed-load transport vector magnitude (Fig. H.3). Changing this parameter hardly affects the transport rates.

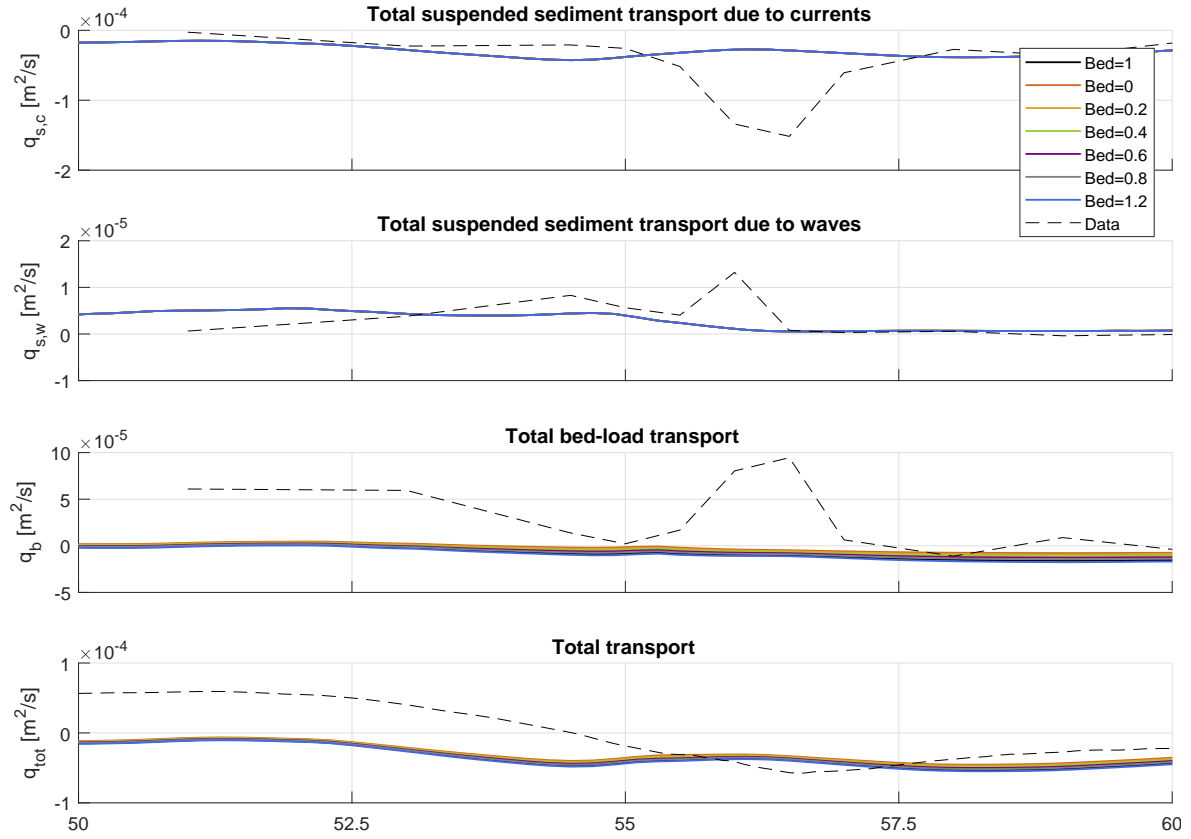


Figure H.3: Sediment transport rates using varying values for *Bed* as presented in Table H.1.

SusW

SusW is the wave-related suspended sediment transport factor (Fig. H.4). Higher values for *SusW* show higher transport rates before $x \approx 56\text{m}$, but the data is still not replicated accurately by the model.

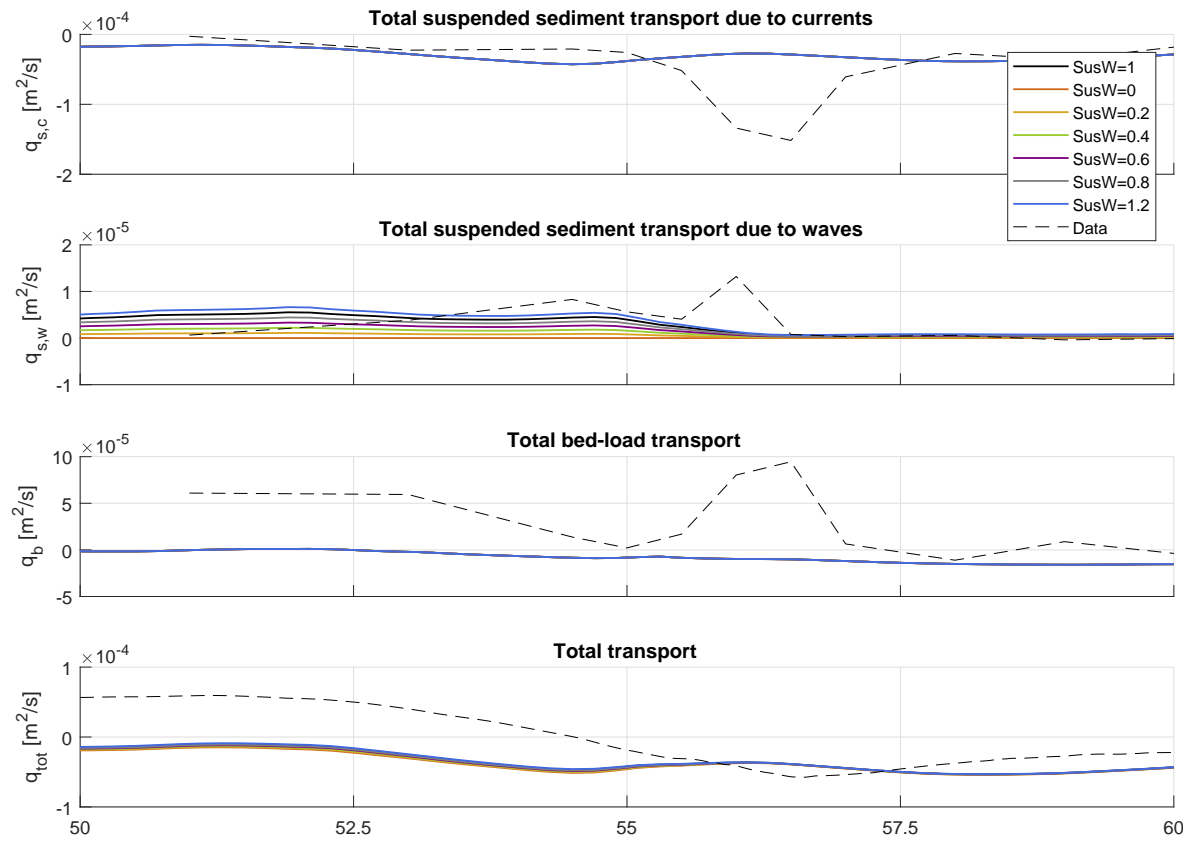


Figure H.4: Sediment transport rates using varying values for *SusW* as presented in Table H.1.

BEDW

BedW is the wave-related bedload sediment transport factor (Fig. H.5). As for *Bed*, *BedW* also hardly affects the transport rates.

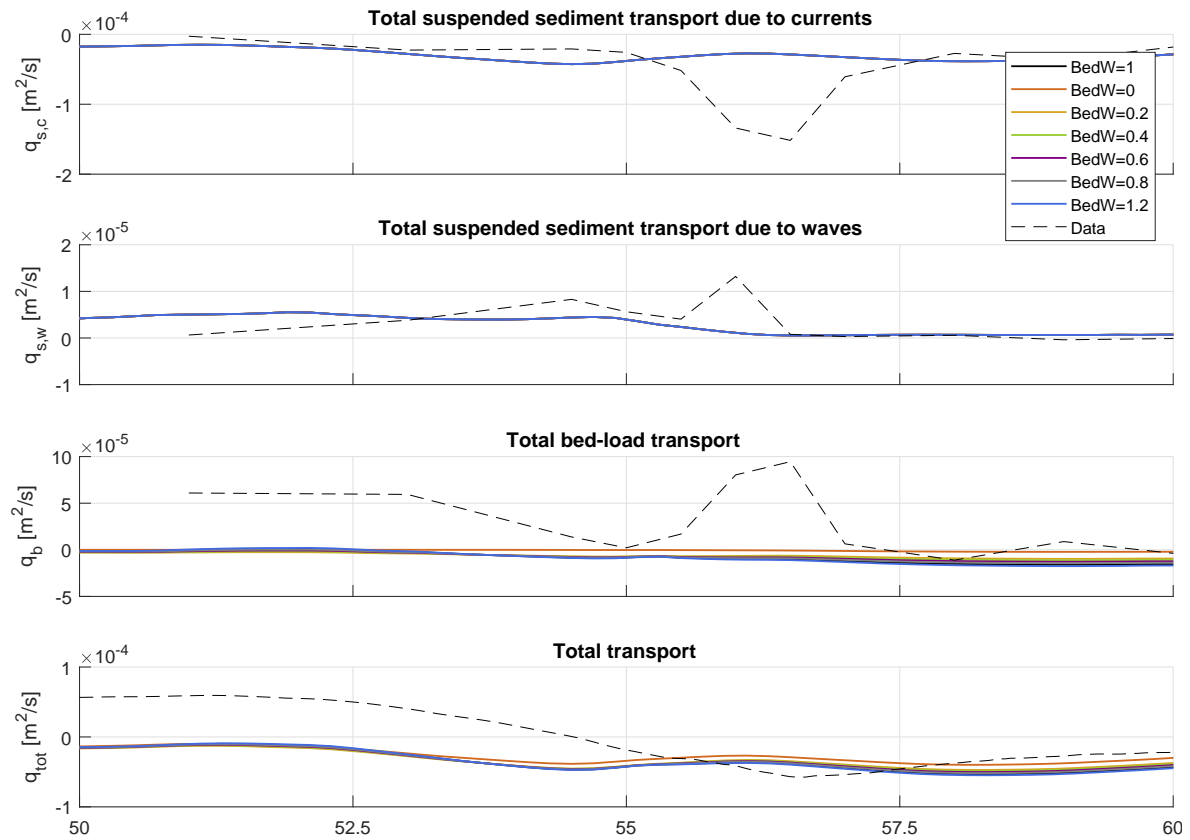


Figure H.5: Sediment transport rates using varying values for *BedW* as presented in Table H.1.

DICOUV

Dicouv is the horizontal eddy diffusivity and affects the mixing due to eddy motion (Fig. H.6). Increasing values for *Dicouv* give steeper slopes and higher transport rates. However, none of the values is able to accurately reproduce the data.

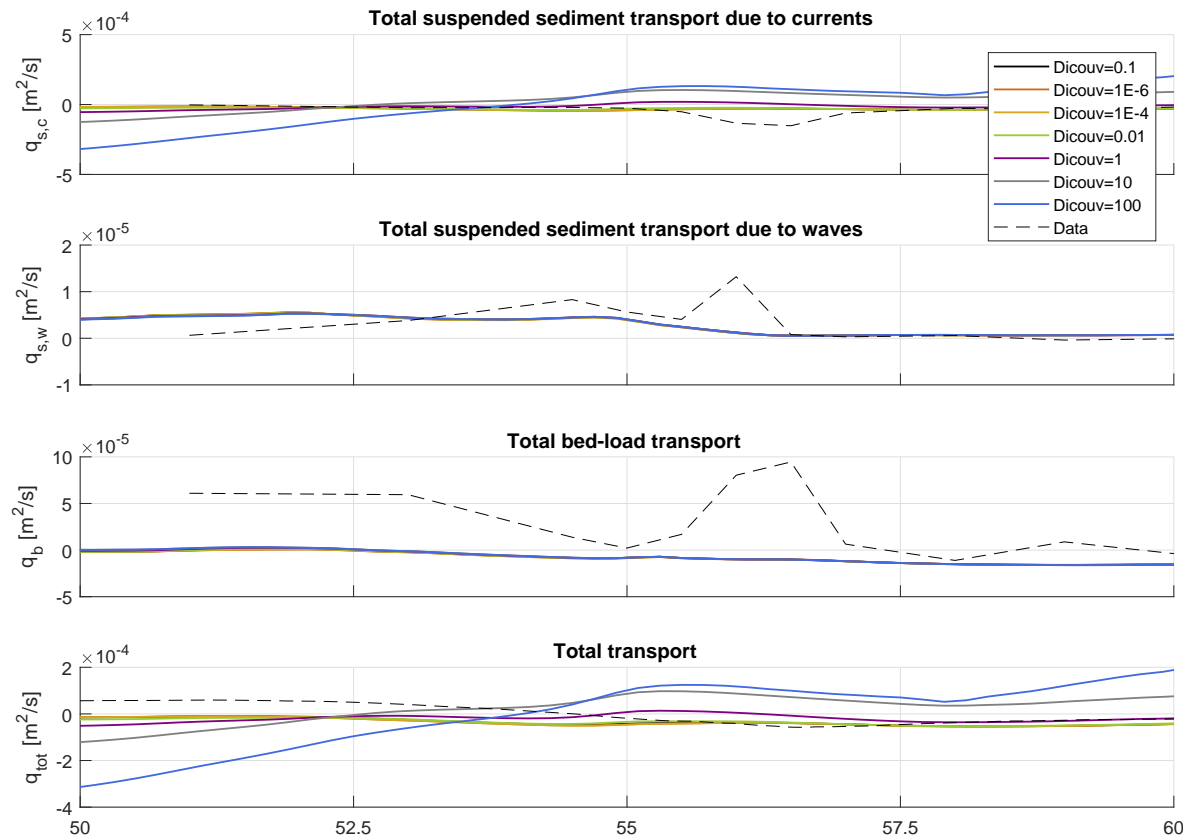


Figure H.6: Sediment transport rates using varying values for *Dicouv* as presented in Table H.1.